THE UNIVERSITY OF CHICAGO

ENGINEERING MATERIAL INTERFACES FOR SELECTIVE TRANSPORT IN AQUEOUS SYSTEMS

A DISSERTATION SUBMITTED TO

THE FACULTY OF THE PRITZKER SCHOOL OF MOLECULAR ENGINEERING

IN CANDIDACY FOR THE DEGREE OF

DOCTOR OF PHILOSOPHY

BY

ZIJING XIA

CHICAGO, ILLINOIS

DECEMBER 2022

TABLE OF CONTENTS

LIST OF FIGURES

LIST OF TABLES

ACKNOWLEDGEMENTS

It is impossible to adequately acknowledge all the people and forces in my life that have enabled me to reach this point.

First and foremost, I would like to thank my Ph.D. advisor Seth Darling for his trust and support throughout the whole time of my doctorate study. I feel very grateful for joining Darling group and having chance working between two institutions, University of Chicago, and Argonne National Laboratory to work with many talented scientists. I have learnt so much from his profound knowledge and enthusiasm for science. Thank you for being an excellent mentor to help me to approach the endeavor of scientific research professionally and productively. I would like to thank the current and former Darling group members, namely Dr. Haocheng Yang, Ruben Waldman, Dr. Feng Gao, Omar Kazi, Yuqin Wang, Wen Chen, and visiting students Huiru Zhang, Xiaobin Yang for being incredible colleagues providing generous help on experiments and productive feedback on all kinds of meetings.

I would also like to thank all of the Shrayesh Patel's research group for accepting me as de-facto group member. Thank you to Garrett Grocke, Dr. Ban Dong, Arvin Sookezian, Tengzhou Ma, Peter Bennington, Veronica Burnett, Priya Mirmira, Hongyi Zhang, Dr. Zhongbo Zhang, Nicholas Boynton, Mark DiTusa, Dr. Zhongyang Wang, and Sam Kopfinge for your help in the troubleshooting ionic transport problems. Thanks to Professor Shrayesh Patel for your guidance, encouragement, and entertaining group meetings.

Next, I would like to thank Professor Paul Nealey, Professor Juan de Pablo, Professor Chong Liu and Professor Junhong Chen for being on my Defense Committee or Candidacy Committee and supporting me as a candidate. It is a great honor for me to present my work to these excellent scientists.

Mainly working at Argonne, I would like to particularly thank Jeff Elam, Alex Martinson, and their group members, especially, Anil Mane, Vepa Rozyyev, and Rahul Shevate, for giving me help, access and trust with their ALD instruments. I would also like to thank Dr. Wei Chen, the lab manager, for helping me to build a nicer and more organized research environment. Thanks also to Dr. Sang Soo Lee for entertaining discussions and productive collaboration. I would like to thank Robin Harris, Susan Podoba, and Judy Brenzing for helping to handle daily issues working for a governmental institution.

Living in Chicago for the past five years has been a great journey and joy. Thanks to all of my friends for making my life in Hyde Park greater and warmer. Thanks to my former and current roommate for supporting and helping each other every day. It is remarkable to live at Chicago, along with Lake Michigan as a researcher focused on water treatment.

Finally, I would like to thank my family. To my parents, Qingbo Xia and Min Ma, you gave me life and unconditional love, care and support through my life, I would never become who I am without you. Thank you to my grandparents, Mingqin Su and Zhongyao Xia, for always providing love and attention to support me. To my ancestors, I hope this work brings honor. Thank my best friend, Xueyan Xie, for always supporting me through ups and downs. This work is dedicated to my family whole-heartedly.

ABSTRACT

Water stress is a vital security challenge that our world faces, and it is intricately connected to the global energy problem. Scientists and engineers have designed different methods for efficiently purifying water. Among these technologies, membranes in particular have proven to be effective for water purification with decades of productive use. Membrane processes have distinct advantages, including high water quality with easy maintenance, stationary parts with compact modular construction, and excellent separation efficiency. With recent innovations in both analytical and fabrication tools, more advanced membrane technologies are surfacing for a multitude of water purification applications.

In this dissertation, we aim to build advanced functional materials for three different membrane systems to manipulate their interfaces to induce selective transport and to apply them for practical use. We have made fundamental insights into the water-membrane interface properties for selective ion transport, yielding first reports of advanced functional materials for several applications.

This work begins with fabricating porphyrin covalent organic frameworks (POFs) using a simple one-pot method to modify membranes for solar steam generation. The focus in the literature of covalent organic frameworks for water treatment has been on desalination, dye removal, and ion capture. We have developed a new direction for these materials, namely, to design and fabricate this material for distillation. We demonstrated a universal, simple, and scalable interface engineering strategy for the fabrication of a solar steam generator based on this POF material. Wood@POF, using wood as the template, exhibited about 80% overall process efficiency for solar steam generation under 1.6 Suns illumination.

In the next chapter, we demonstrate a route to tune the ion-transport properties of vermiculite membranes by introduction of alkanediamine molecules to crosslink the layers. We show that the interlayer spacing can be tuned by introducing diamines of different molecular lengths, and the crosslinked vermiculite membranes exhibit distinct ion-separation performance. The methodology outlined here could be extended to other layered materials with different inherent layer spacings and electrostatic properties, opening a pathway for designing a diverse range of 2D membrane materials with tunable ion transport.

Next, a systematic study of surface charge properties of atomic layer deposition (ALD) grown films in aqueous environments is established. 17 different ALD-grown metal oxide films are synthesized, and a comprehensive study of their water stability, wetting properties, and surface charge properties are provided. This analysis represents a resource guide for researchers, and ultimately for materials and process engineers, seeking to tailor interfacial charge properties of membranes and other porous water treatment components.

Lastly, ongoing experimental work in the development of a Janus membrane via ALD is detailed. Detailed characterization of the structure, properties, and function of these membranes will ultimately provide a thorough understanding of ionic transport properties, with ramifications extending beyond the applications explored herein.

Chapter 1: INTRODUCTION

Water security is a crucial element of the energy, climate, food, economic, and human security challenges that our world faces in the coming decades.[1] As the economy expands rapidly, water demand will increase along with pollution and wastewater generation. Unlike energy sources, water has no alternative sources. Thus, water stress represents a massive and growing social risk. To mitigate this challenge, various technologies have been explored to increase supplies of fit-for-purpose water, including membrane separation, catalytic degradation, adsorption, and solar steam generation, to name a few. These techniques can be divided into three main categories: chemical, physical, and biological methods. To date, no single process is capable of effective treatment on its own due to the complex composition of typical wastewater; generally, one must apply a combination of various techniques in sequence.

Improving upon desalination, water recycling, and pollution remediation technologies will only be possible with a thorough understanding of the interactions of complex aqueous fluids with materials relevant for sorption, membranes, and other components of water treatment systems. Scientific understanding of interactions and transport involving ions is particularly poor. Furthering this understanding will have benefits beyond potential innovations in water treatment technologies. Water at interfaces plays essential roles in many water treatment applications.

To better understand the ion transport process and water interfaces in aqueous systems, we propose the design and synthesis of new model porous materials, in some cases recently enabled by the discovery in our group of a method for gradient interface engineering, for nanofiltration and osmotic energy harvesting. We propose three different systems, which offer

complementary capabilities and an opportunity to broaden our understanding of more than one mechanism: covalent organic frameworks (COFs), phyllosilicate 2D material membranes, and Janus membranes.

1.1 Membrane for Water Treatment

Based on the pore size, membrane separation processes are classified into one of the following categories: reverse osmosis (RO), nanofiltration (NF), ultrafiltration (UF), and microfiltration (MF). (Figure 1.1) Among these types of membrane, MF membranes have the largest pore size, around 0.1-5 μm, and RO membranes bare the smallest pore size, within 1 nm, because they are mainly designed for the separation of metal ions or salt ions. [2]

This dissertation mainly focuses on membranes of pore size between 1 to 100 nm, which fall under the NF and UF categories.

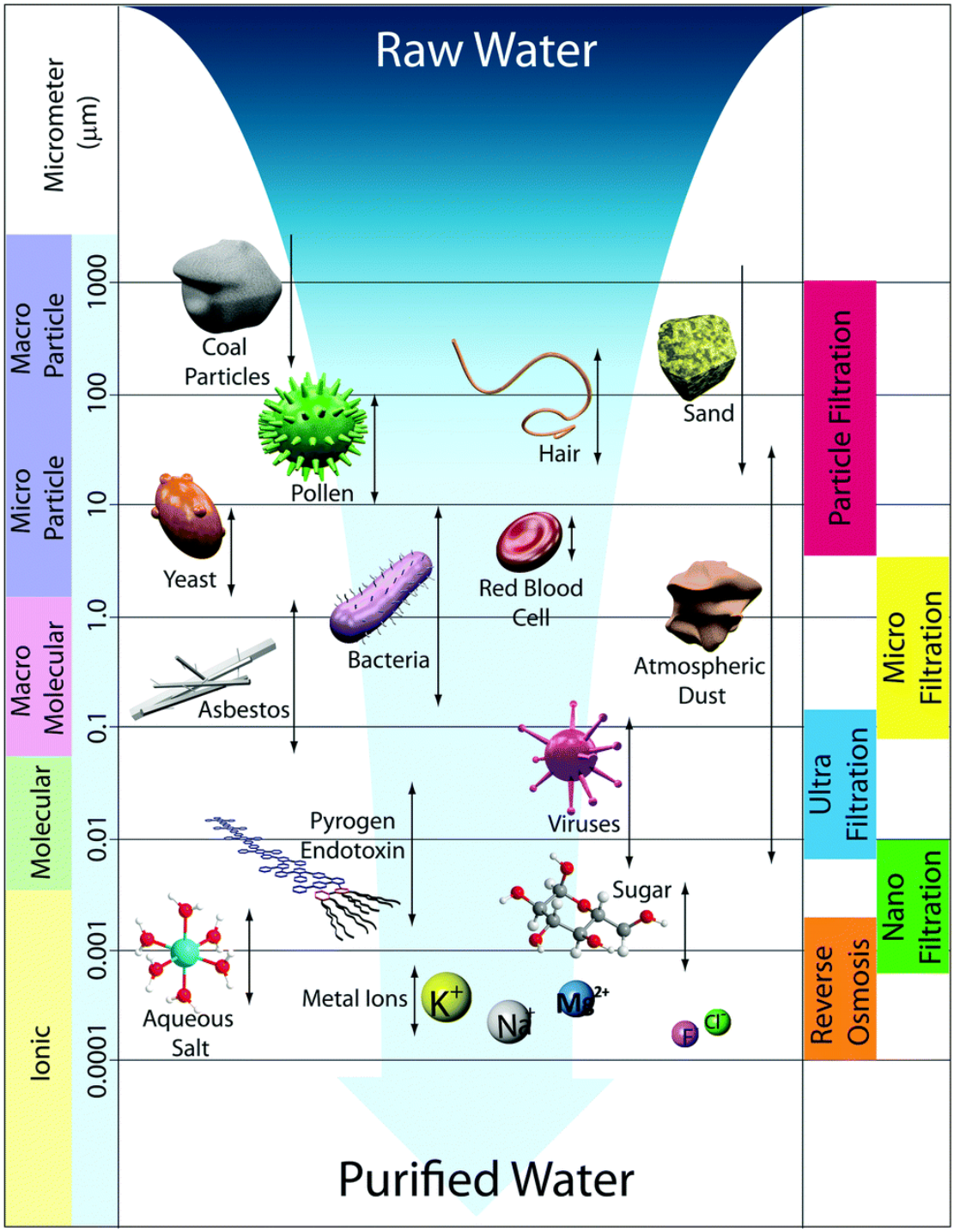

Figure 1.1: Schematic of the membrane filtration spectrum. RO, NF, UF, and MF membranes have different pore sizes and applications. (Reproduced from [2])

1.2 Covalent Organic Framework-Based Membranes

Porous materials, such as porous carbons, zeolites, conjugated microporous polymers (CMPs), porous aromatic frameworks (PAFs), and metal organic frameworks (MOFs) have attracted substantial attention for their high surface area and abundant active sites. However, there remains a need for porous structures with highly ordered aperture size and tunable structures with designer properties. Covalent organic frameworks (COFs) are crystalline framework materials, constructed by covalent bonds from reactions of light elements including carbon, nitrogen, hydrogen, oxygen, and boron. COFs were first reported by Yaghi and co-workers in 2005.[3] Because of their high porosity, highly organized pore structures, adjustable chemostability, tunable surface properties, and controllable aperture size, COFs have been applied for gas separation[4], gas storage[5, 6], catalysis[7, 8, 9], chemical sensing[10], and energy storage[11, 12]. Recently, COFs' potential versatility in water treatment applications has generated excitement in the field. Their designable aperture size and hydrophilicity make COF films or mixed matrix membranes (MMMs) with COF particles as nanofillers promising candidates for desalination or selective organic contaminant removal from aqueous solutions. Moreover, COF powders with tunable surface properties, created by introducing different functional sites on the organic linkages, are promising for selective metal ion detection and adsorption.[13]

COF films can be synthesized through a bottom-up strategy involving solvothermal synthesis[3], interfacial synthesis[14], room temperature vapor-assisted conversion[15], or synthesis under continuous flow conditions[16]. Alternatively, a top-down strategy can be implemented to obtain COF thin films from bulk materials, including solvent-assisted exfoliation[17], mechanical delamination[18], chemical exfoliation[19], or self-exfoliation[20]. COF powders have generally been synthesized through the solvothermal method. The reader is directed to existing reviews for

details on COF fabrication processes.[21, 22, 23] The state-of-the-art applications of COFs for water treatment are in desalination, dye removal, ion capture, and beyond (Figure 1.2).

To utilize COF materials for water treatment, stability in water is an obvious prerequisite. Many COFs show good thermostability, but stability in aqueous solution remains a challenge for certain COFs. The physical aperture size defines the application space among membrane separation processes such as RO, NF, UF, and MF; the design and fabrication COFs with tailored pore size(s) is crucial for practical use. Properties like surface charge and hydrophilicity are also important with regard to performance, which can be controlled through post-synthesis or bottom-up methods. Introducing COFs into other materials to obtain hybrids is also a widely used method to enrich functionality.

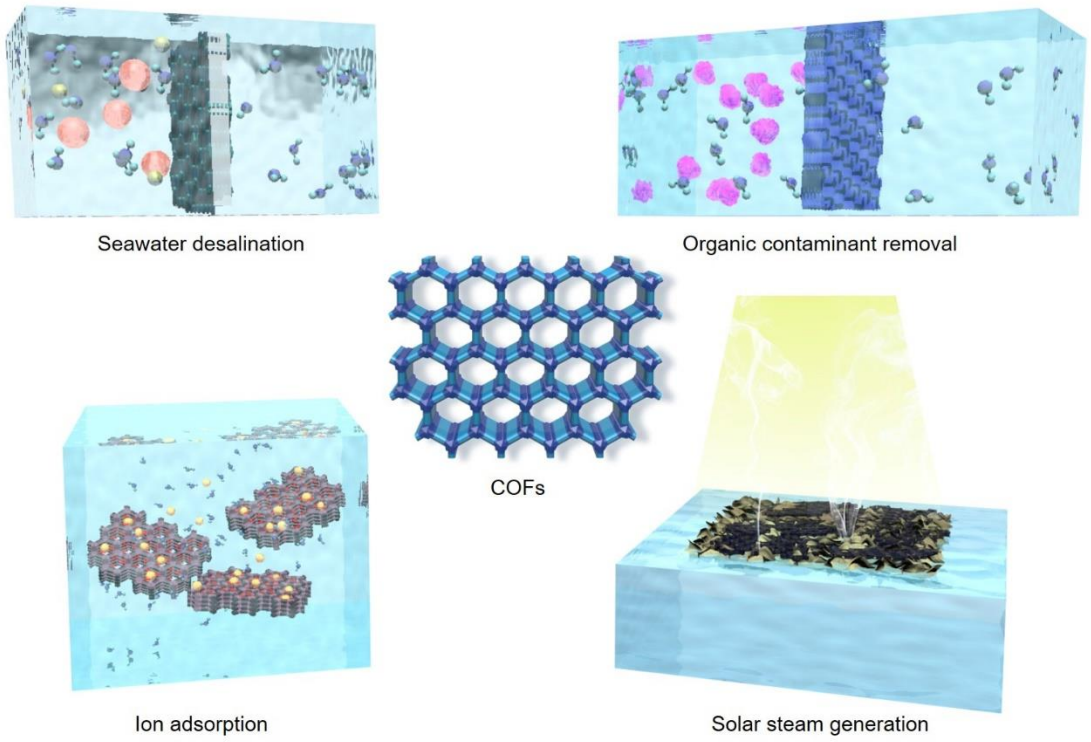

Figure 1.2: Key applications for COFs in water treatment. (Reproduced from [13])

Functionalization endows COFs with new or modified properties. Bottom-up synthesis and post-synthesis modification (Figure 1.3) are the two general strategies to accomplish such functionalization (e.g. surface charge or hydrophilicity), in analogy to the approaches discussed previously for pore-size regulation.[23]

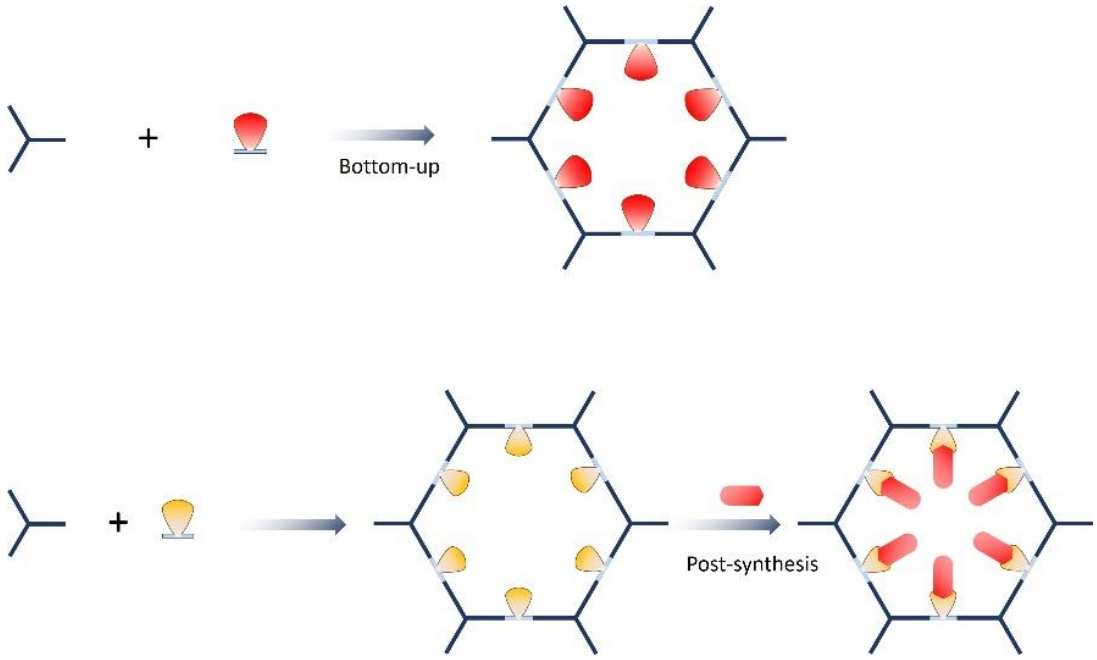

Figure 1.3: Typical photothermal materials and their light-to-heat conversion mechanisms.

Bottom-up synthesis is at once both a straightforward and a difficult approach for COF design and construction. The functional moieties will be directly included in the designed building units before completing the synthesis.[21] For example, the surface charge of COFs can be manipulated by the predesign of building-block monomers. Bottom-up strategies have succeeded in constructing COFs for gas storage[24] and photoelectric applications[25], and have also shown potential for water treatment in some early studies. However, the design and fabrication of a new COF with good chemostability, crystallization, and porosity is a significant challenge.

Water treatment in complex aqueous systems imposes a difficult set of requirements on materials; one must consider the water stability, hydrophilicity, and charge distribution. Often, COFs excel in exhibiting a subset of these properties while struggling to achieve others. Combining COFs with other materials to create a COF-based hybrid is a potentially simple and useful method to combine the merits of both materials. Many kinds of materials have been reported to combine with COFs for water treatment, such as MOFs, GO, and polymers. The intended application will dictate material selection in such hybrids. For seawater desalination or dye removal, COF particles embedded in the crosslinked polymer polyamide (PA) can function as a selective layer. COF thin films on UF support layers are another practical option. For ion adsorption, graphene has been integrated into COFs to increase water stability and separation ability.[26]

Solar steam generation (Figure 1.4) is a promising technology for treatment of saline or wastewater, drawing on plentiful sunlight as a clean and renewable energy source for distillation.[27, 28, 29] In this application, one needs an efficient photothermal material that can harvest a broad range of wavelengths, convert the energy into heat, and transfer that heat to water at an air/water interface for enhanced evaporation.

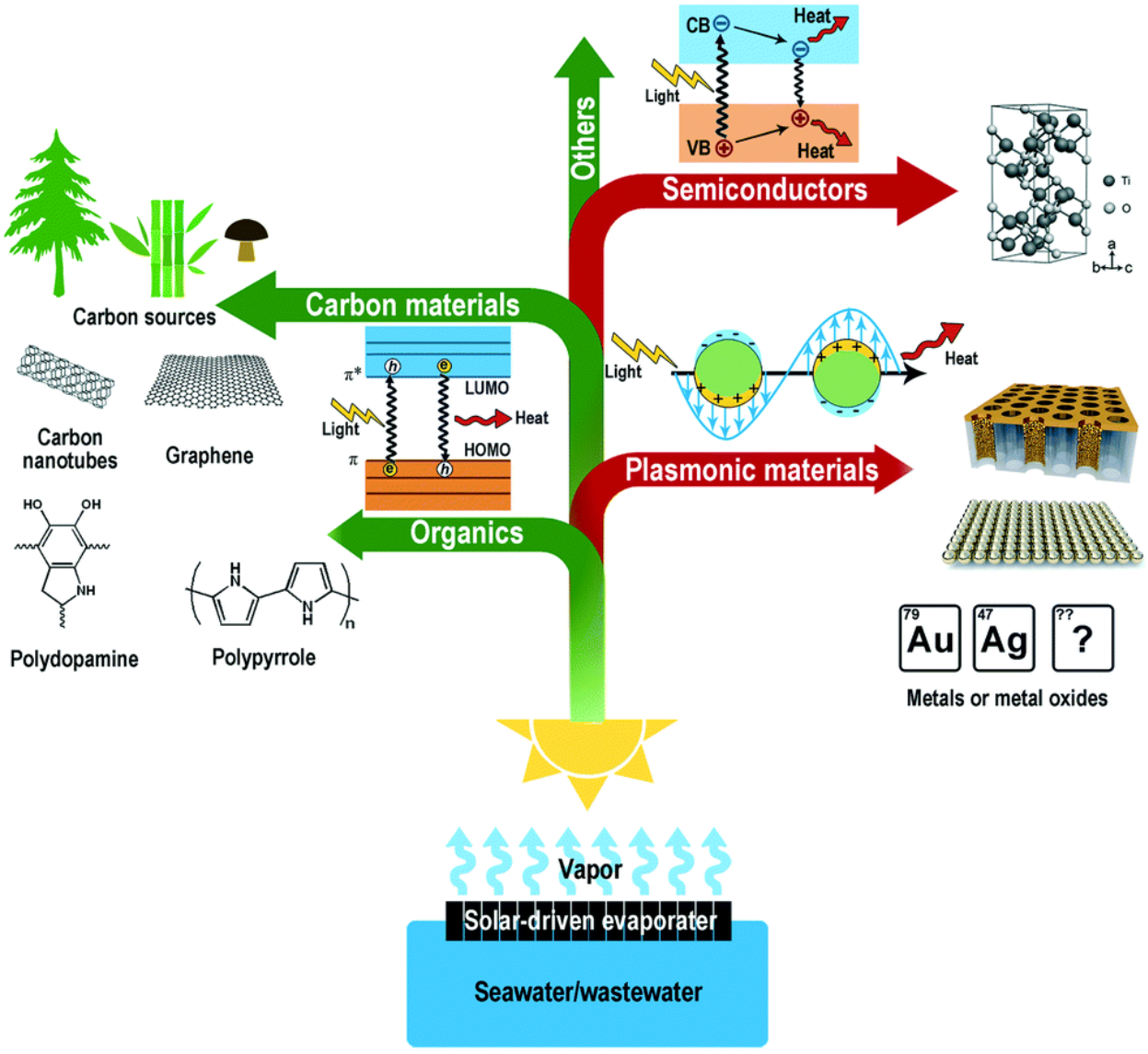

Figure 1.4: Typical photothermal materials and their light-to-heat conversion mechanisms. (Reproduced from [30])

COFs with highly uniform and ordered aperture size provide passages can, in principle, deliver ultrahigh-selectivity molecular sieving. Defect-free COF thin membranes can be assembled onto UF substrates as a selective layer, and COF powders can be used as nanofillers in active layers of mixed matrix membranes. COF particles are also often implemented as adsorbents because of the high surface area and abundant surface active sites (chelating sites) for heavy metal ions, radioactive ions, or organic pollutants. The design and the introduction of

surface functionality govern the adsorption performance of COFs. COFs with broad sunlight wavelength absorption property and photothermal conversion efficiency have shown potential for solar steam generation, and the use of COFs as photocatalysts or capacitive deionization electrodes materials has only just begun.

The history of COF materials for water treatment is only about five years old; the opportunities going forward are vast, presuming detailed foundational studies continue. Much remains to be learned about the relationship between COF structure and performance/properties. The mechanism of ion adsorption in COFs, development of tailored active sites for selective ion capture, and the role that COFs particles play as nanofillers during separation processes still need further investigation. With more in-depth understanding of the relationship between performance and structure, more COF-based materials could be designed and explored effectively for water treatment. A closely related application space is in sensor technology, where selectivity of adsorption is also paramount. This is a topic ripe for additional exploration. With more comprehensive understanding of the structure-performance relationships present in this diverse class of materials, COFs may indeed play an important role for water treatment in the future. As new COF platforms are developed, including engineering of their interfacial charge and chemistry[31], it is certain that there will be exciting new discoveries with untold impact in addressing our society's water challenges.

1.3 Phyllosilicate Two-Dimensional Material Membranes

Two-dimensional (2D) materials (Figure 1.5) of atomic-scale thickness have emerged as promising candidates to develop membranes with unique nanopores or nanochannels. 2D material membranes feature unique permeation properties, providing a new pathway for fast and

highly selective membranes for water separation. 2D materials can be fabricated into two categories of membranes: nanosheet and lamellar membranes.[32] In general, the molecular transport direction is perpendicular to the membrane for nanosheet membranes, which consist of 2D materials with uniform pore sizes for separation. In 2D lamellar membranes, the pathway of molecules is parallel to membranes, which is fabricated by the restacking of 2D material nanosheets. By choosing different 2D materials and tailoring the surface structures, those 2D material membranes could exhibit both high flux and selective properties. The selectivity and the transmembrane flux are also determined by the membrane thickness.

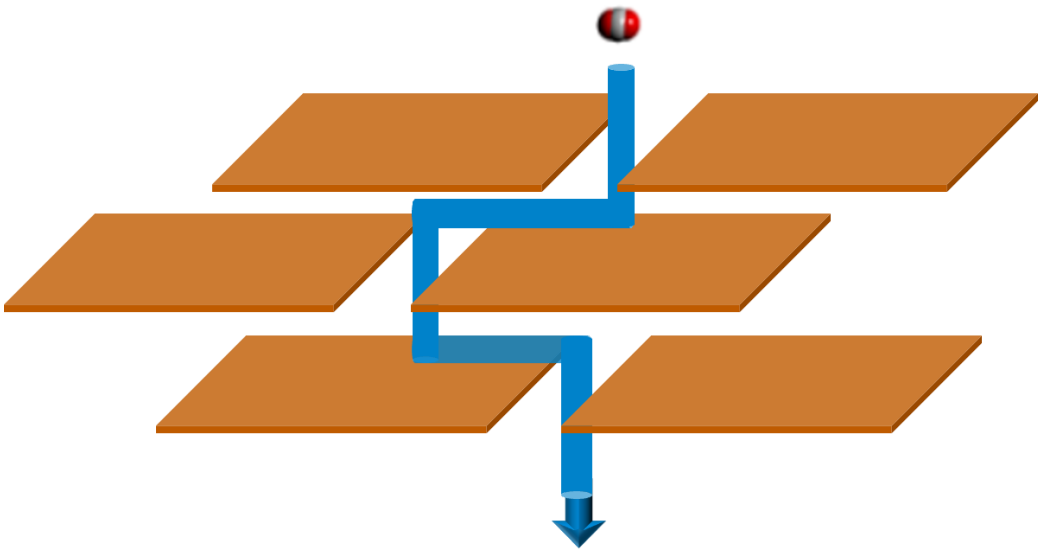

Figure 1.5: Interlayer spacing of 2D material membranes provides pathways for molecules and ions transport through membranes.

2D material nanosheet membranes consisting of materials such as metal organic frameworks (MOFs),[33, 34] zeolites[35, 36] or graphene-like materials[37, 38, 39] have pore size range from 0.25 to 5 nm.[40, 13] Compared to 2D material nanosheet membranes, 2D material lamellar membranes always behave lower separation efficiency because of their higher thickness. However, they can also be easily fabricated on a larger scale, which are more suitable for

practical applications. To date, various 2D materials have been successfully fabricated as lamellar membranes for water separations or other applications. Among these 2D materials, graphene oxide (GO)[37, 41] is the most popular candidate. Besides graphene, 2D atomic crystals such as transition metal dichalcogenides,[42, 43] layer double hydroxides (LDHs)[44, 45] and MXenes[46] have received increased attention because of the nature of their 2D structures and unique chemistries.

Phyllosilicates refer to the group of minerals which form parallel sheets of silicate tetrahedra. Phyllosilicates can be broadly classified into two categories one where the composition is 1:1, wherein there is one tetrahedral sheet for every octahedral sheet present and another class of minerals have a 2:1 composition with one octahedral layer between two tetrahedral layer. These sheet silicates include number of minerals like clay, mica, chlorite, serpentine, talc, etc. The layer of water molecules occupies a spacing of about two water molecules. The extent of hydration the way the layers are stacked within the structure of the clay mineral is heavily dependent on the radius and the charge of the exchangeable cations present in this space. For example, the interlayer spacing of vermiculite varies according to the relative humidity and also the cations from 10.5 to 15.7 Å. [47]

1.4 Janus Membranes

1.4.1 Concept of Janus Membranes

Janus objects have been of great interest for over thirty years since Cho and Lee reported the first Janus particle, consisting of polystyrene and poly(methyl methacrylate), in 1985.[48] Widespread attention was then garnered after P. G. de Gennes's Nobel Prize lecture.[49] The Janus

object, named after the Roman god Janus, has two faces with different properties on each side. Among different Janus objects, Janus membranes have attracted much attention for the past several years.[50] In contrast to conventional counterparts, Janus membranes exhibit opposite properties on each side, like positive/negative surface charge, hydrophilic/hydrophobic surface, etc. These kinds of asymmetric structures make Janus membranes obtain an intrinsic "inner" driving force to control the transport properties of ions and molecules along the channels.[51] This inner driving force provides an additional potential, increasing the expected mass or energy flow when it aligns with the external driving force, while decreasing those flows when counter aligned.[52]

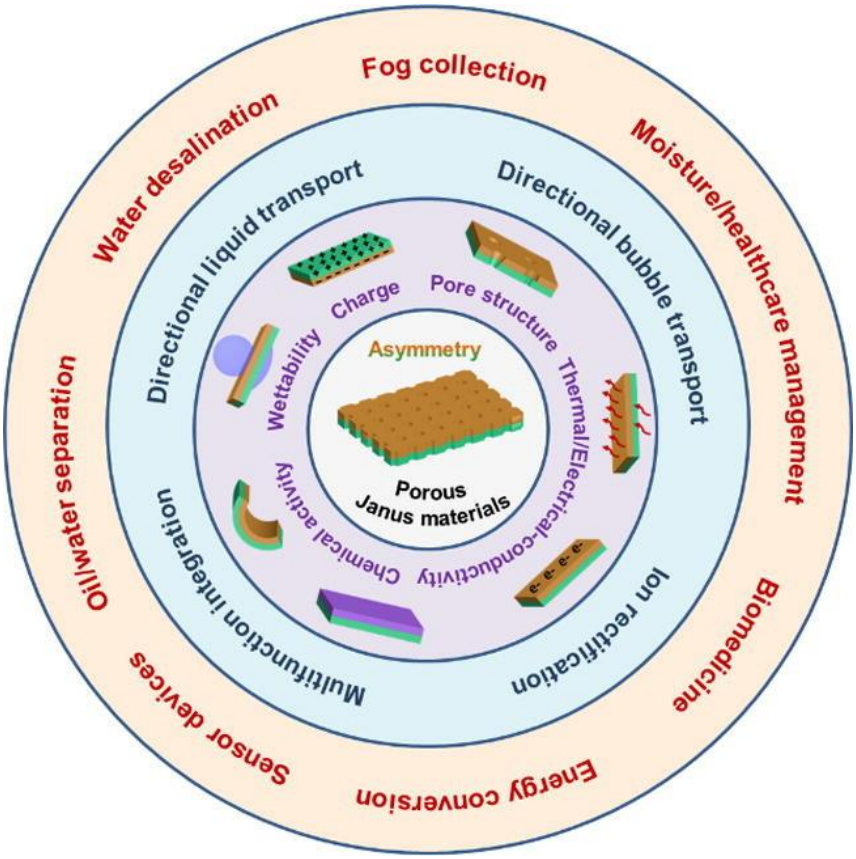

Figure 1.6: Summary of the properties, functions, and potential applications of porous Janus materials based on various asymmetries (wettability, charge, pore size or structure, thermal or electrical conductivity, or chemical activity). (Reproduced from [53])

Due to the unique structure of Janus membranes, they have shown much promise for different applications, including nanofiltration, demulsification, and osmotic energy conversion. (Figure 1.6)

Normally, Janus membranes could be fabricated by two approaches (Figure 1.7): asymmetric fabrication and asymmetric decoration (through interfacial strategies or non-interfacial strategies). Asymmetric fabrication introduces the Janus structure during the membrane formation process, while asymmetric decoration introduces the Janus structure by post-modification after membrane formation.[50, 52]

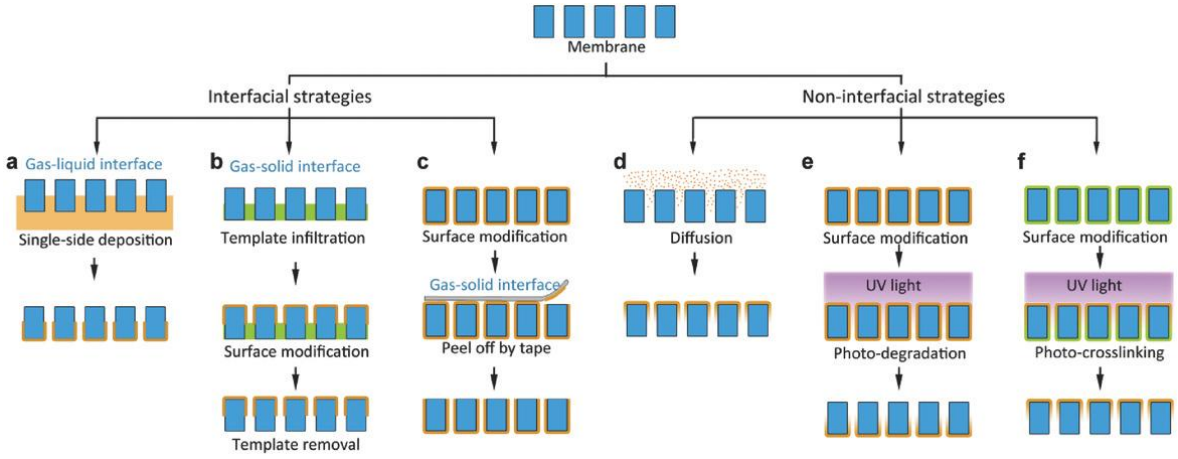

Figure 1.7: Scheme of fabrication processes of Janus membranes. (Reproduced from [52])

The conventional method to make a Janus membrane is to fabricate each side of the membrane separately and then combine them together. For example, sequential electrospinning[54] and sequential vacuum filtration[55] are the two most common methods used to fabricate Janus membranes.

Another popular method to generate Janus structures is one-side modification. By controlling directional diffusion or other asymmetric treatments, this goal could be achieved easily. For example, shingle-faced photo degradation[55,56], single-faced photo crosslinking[57], vapor treatment[58], sing-faced coating[59], floated deposition[60], and sequentially surface modification[61] have been successfully applied.

The thickness of each layer can be precisely and conveniently controlled by both above-mentioned processes. However, most studies use interfacial combination via physical connection, which yields materials that are difficult to modify and that suffer from instability and relatively low surface energy. Herein, we propose to use atomic layer deposition (ALD) as a surface modification method to generate Janus structure.

1.4.2 Introduction to Atomic Layer Deposition and Sequential Infiltration Synthesis

ALD is a novel technology for conformal membrane coating by which alternating reactant vapors (also called precursors) enable atomic layer-by layer growth of different kinds of materials, including metals, metal oxides, metal sulfides, and even organic materials. During the ALD process (Figure 1.8), the alternating pulses of vapor precursors are used to deposit material onto the targeted substrates. Each precursor will irreversibly react with the substrate chemically, and each step is called a “half-reaction”. Subsequently, the ALD reactor chamber is purged with carrying gas (typically N_2 or Ar) to remove all unreacted precursor and by-products. Then following the pulse and purge of the counter-reactant precursor, a single layer of the desired material is formed. The total process of these steps is called one cycle. This process is then cycled until the appropriate film thickness is achieved. In an ideal ALD system, each cycle

deposits a certain uniform layer of targeted material, and the growth rate is known. However, the ALD process is very complicated in reality, and can be affected by temperature, chemistry, flow rate, and precursor diffusion time.

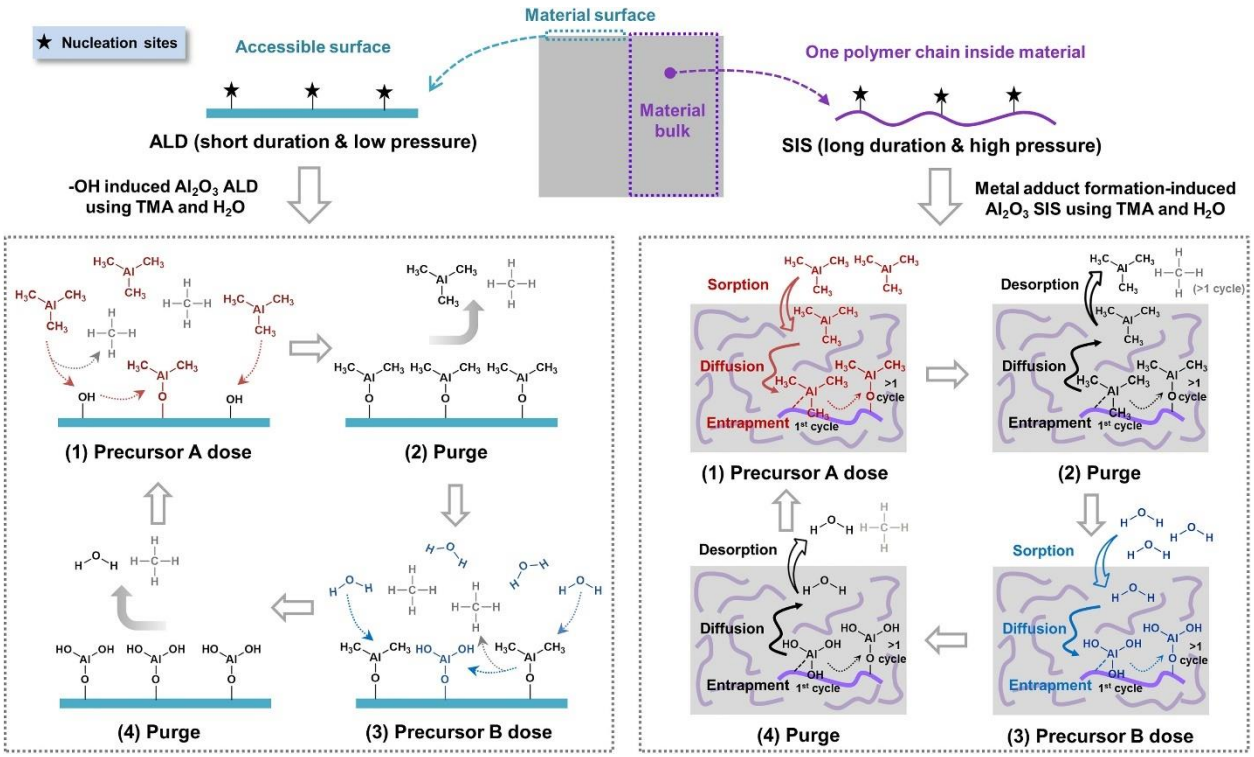

Figure 1.8: Scheme of ALD and SIS interface engineering in terms of nucleation site-induced Al_2O_3 functionalization using precursors trimethylaluminum (TMA) and water. (Reproduced from [62])

Conformality of high aspect ratio and three-dimensional structured materials is made possible by the self-limiting characteristic of ALD, which restricts the reaction at the surface to no more than one layer of precursor. With sufficient precursor pulse times, the precursor can disperse into deep trenches, which not only retains the original pore structure of the membrane but also achieves nearly 100% coverage. This combination of attributes is important for catalytic

or adsorptive membranes requiring high active area. Lastly, the coating thickness can be precisely and continuously tuned across a wide range from nanometers to micrometers.[63]

A new synthesis method developed 10 years ago, sequential infiltration synthesis (SIS) (sometimes referred to as vapor-phase infiltration), extended the capabilities of ALD-like processing via material-bulk-controlled vapor-solid reactions.[64] ALD and recently developed related methods like SIS offer a tremendously diverse library of chemistries for interface functionalization with intimate control over the surface properties. Thickness, stoichiometry, gradient structures, and more can be manipulated with precision.[65] In addition, much has been learned in the past few years regarding the physical chemistry of SIS, which relies on a complex interplay of covalent and non-covalent reactivity and diffusion.[62]

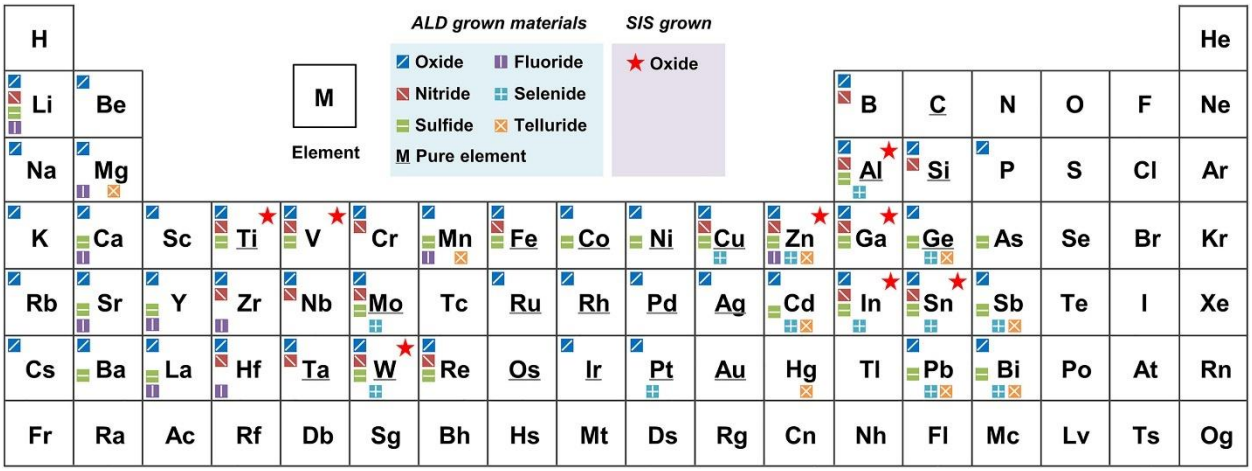

Figure 1.9: Library of ALD- and SIS-grown materials. (Reproduced from [62])

A wide variety of materials have been synthesized via ALD (Figure 1.9). ALD, being a far more mature technology, has established fabrication of many kinds of materials, including

oxides, sulfides, nitrides, and pure elements. Compared to ALD, the library of materials grown by SIS is still very limited far now. The current published library of SIS coating materials includes ZnO, TiO_2, In_2O_3, Ga_2O_3, Al_2O_3, and some few other metal oxides.

Chapter 2: PORPHYRIN COVALENT ORGANIC FRAMEWORK (POF)-BASED INTERFACE ENGINEERING FOR SOLAR STEAM GENERATION

Through replacement of traditional energy sources with sunlight as the heat source, solar steam generation has emerged as a promising technology for water purification and desalination. Despite significant efforts to develop efficient photothermal materials for solar steam devices, challenges associated with scalable fabrication of high-performance materials remain. Moreover, most existing methods cannot be easily engineered to produce steam-generating devices with both arbitrary control over shape and high photothermal efficiency. Herein, a flexible porphyrin organic framework (POF)-based interface engineering method is introduced to produce high-performance solar steam generators. POFs, a recently discovered class of materials, are demonstrated to grow readily on a diverse range of porous substrates, including membranes, fabrics, sponges, and wood. Wood@POF exhibits particularly strong performance, achieving ~80% light-to-steam conversion efficiency. This study demonstrates a universal, simple, and scalable interface engineering strategy for the fabrication of solar steam generators based on POF materials.

2.1 Introduction

Water and energy represent two essential—and intertwined—elements of life and society. With expanding population and rapid urbanization, both freshwater and energy supplies are increasingly strained.[66, 67, 68] Existing methods for mitigating clean water shortage at the expense

of greater energy consumption are unsustainable.[69, 70] Solar-driven distillation/solar steam generation for wastewater treatment and seawater desalination is one promising strategy to help address this challenge in that it draws on plentiful sunlight as the clean and renewable source.[27, 71] To achieve effective solar steam generation, one needs evaporators that can float on water to concentrate heat energy at the water-air interface, where evaporation takes place.[27, 72, 73] Ideally, though, high-performance solar steam generators must also combine all the following characteristics:

(1) buoyant on water, (2) absorbs a broad spectrum of light to utilize the solar irradiation effectively, (3) high light-to-heat conversion efficiency, (4) porous structure that facilitates heat transfer to water while promoting water movement from the bulk to the interface, and (5) low thermal conductivity to minimize heat losses to the underlying water body.

Recently, various photothermal materials have been developed for solar steam generation, including carbon materials,[74, 75, 76, 77, 78, 79] plasmonic metals,[79, 80, 81] and semiconductors.[82, 83, 84] Compared with other materials, carbon materials have high stability and low cost.[85] Carbon nanotubes[76] and graphene[77] have been applied in solar steam generation, and wood,[72, 86, 87] mushrooms,[73] and carbon nanomaterial-based ink[88] have also been implemented in light-to-heat conversion. Relevant localized interfacial heating membranes works a lot in this field.[89, 90] Many of these syntheses cannot be easily Reproduced to impart photothermal properties to arbitrary porous substrates—a necessary attribute in the development of solar steam technologies. There remains a pressing need for scalable, water-stable photothermal coatings. Herein, we introduce a new porphyrin organic framework (POF)-based interface engineering strategy for solar steam generation,[31] demonstrating a simple one-pot method for photothermal material fabrication.

Covalent organic frameworks (COFs) are a class of advanced porous materials with abundant diversity in structure and composition, first reported by Yaghi and coworkers.[3] Since then, COFs have been applied in various research areas including carbon capture,[91] gas storage,[92] and catalysis.[93, 94] Recently, a new sub-class of COFs based on porphyrins (POFs) was reported with demonstrated ability to uniformly grow on the surface of diverse materials with a range of different porosities and hydrophilicity, while also exhibiting useful electrochemical properties.[95] The repeat unit of POF, porphyrin, has unique optical characteristics that may be exploited in the context of new applications. Moreover, porphyrins are conjugated and highly delocalized organic molecules with a strong ability to coordinate metal cations into complexes. These characteristics make porphyrin and porphyrin-derived structures promising candidates for solar steam generation and multifunctional applications in water-energy systems. Li and coworkers recently reported a mild synthesis method to obtain POFs and used it for sustainable applications including Li -S batteriesand Li metal protection.[95, 96, 97, 98]

In this contribution, we apply POFs for the first time as photothermal materials for solar steam generation. This application exploits POFs' light-harvesting characteristics as well as their natural ability to form uniform coatings on porous substrates as a direct result of the synthetic procedure. The fabrication process is one-step, one-pot, and applicable to a wide range of template materials. The chemical structure of the POF is shown in Figure 2.1.

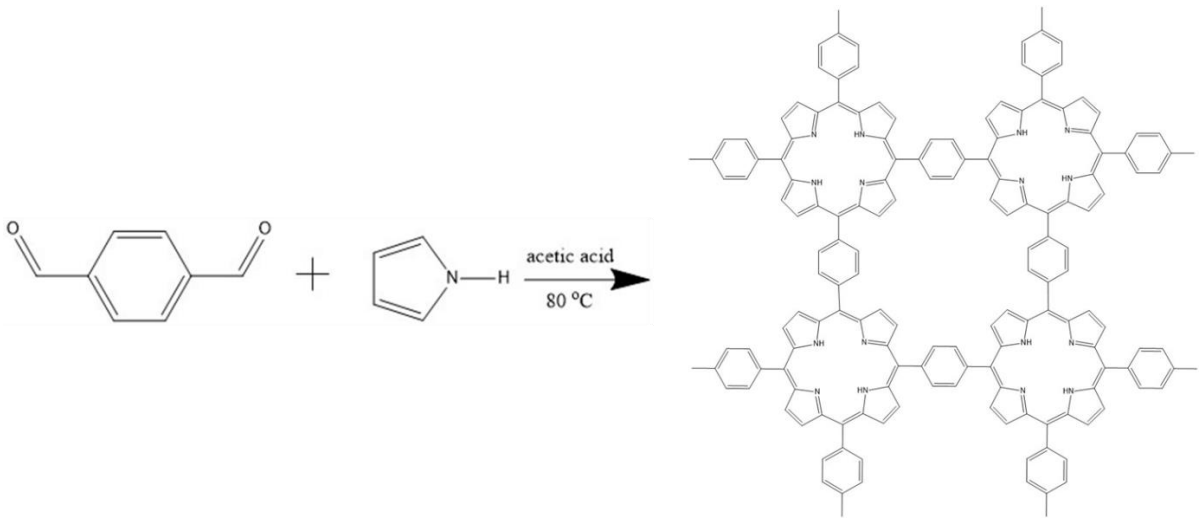

Figure 2.1: Schematic of direct synthesis of POF

There is enormous flexibility regarding the materials used as the supporting scaffold for these POFs, enabling one to select an available material meeting the local needs. The template@POF materials were one-pot synthesized following an acid-catalyzed dehydration reaction of benzene-1, 4-dialdehyde (BDA) and pyrrole and porous structured materials as templates. Pure POF exhibits a dense spherical morphology with a diameter of ca. 1.0 μm (Figure 2.2). Figure 2.3 depicts the scheme for in situ growth of POFs within porous templates. These POF-based materials showed strong performance in sunlight-driven water evaporation. Wood@POF was particularly effective, presenting high evaporation efficiency (79.6 ± 3.0 %).

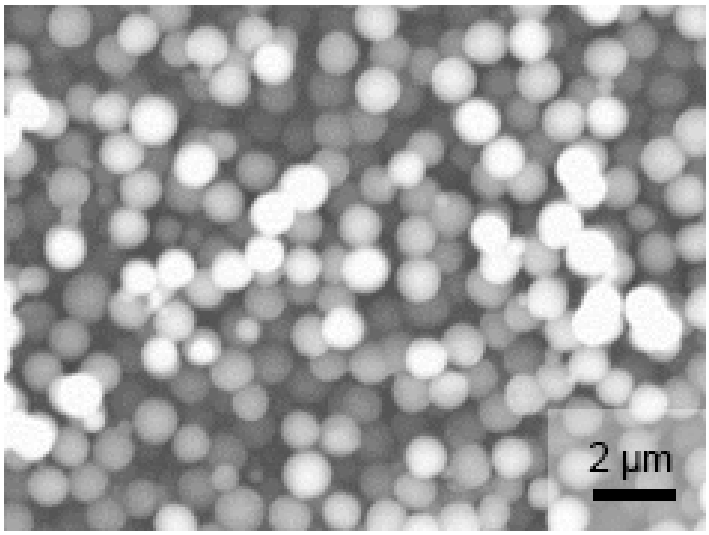

Figure 2.2: Scanning Electron Microscopes (SEM) image of POF particles

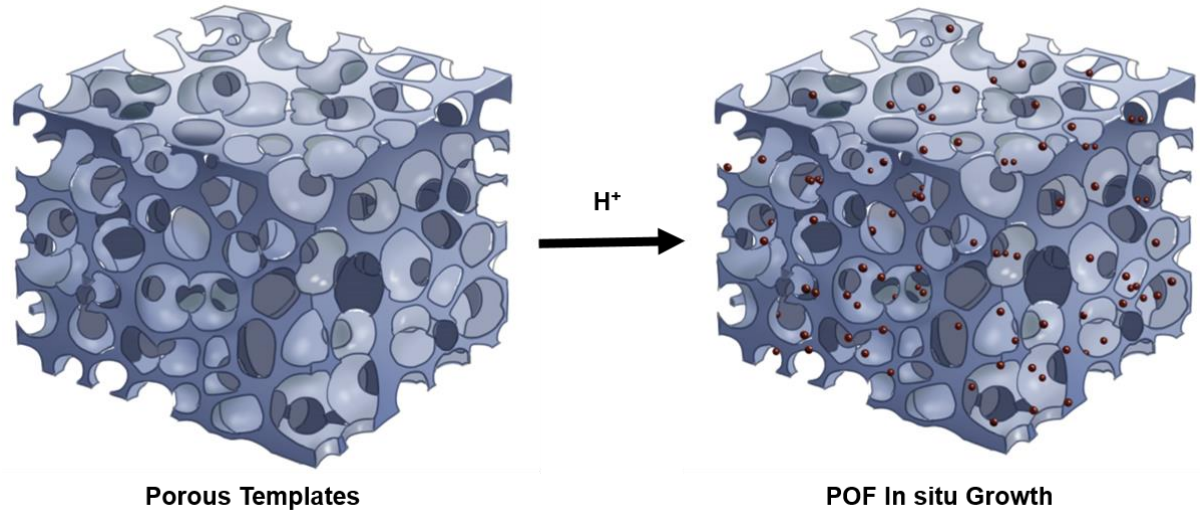

Figure 2.3: Schematic of the synthesis process for POF-based solar steam generator

2.2 Results and Discussion

2.2.1 Fabrication and Characterization of Templates@POF

Assisting template materials were placed into the precursor solution, providing nucleation sites for in situ growth of POF. Several porous materials with widely varying surface chemistry and structure, including wood, anodic aluminum oxide (AAO) membrane, sponge, and fabric, served as the supporting substrates for POF growth, demonstrating the versatility of this method. Among these commonly available materials, wood is a nearly ideal option since it meets most of the requirements for solar steam generators, for example, density lower than water, low thermal conductivity, high hydrophilicity, and a porous internal network comprised of microvoids and cell wall capillaries. These templates were immersed in the precursor solution for 24 h. The as-prepared materials were then washed, sonicated, and dried, producing four types of optically black templates@POF (Figure 2.4 a-h). POFs successfully grew on the outer and interior surfaces of all the tested template materials. Under simulated sunlight irradiation, all the templates@POF show excellent photothermal properties, with a surface temperature above 90 °C (Figure 2.4 i-l), which indicates that POF-based materials are promising candidates for solar steam generation.

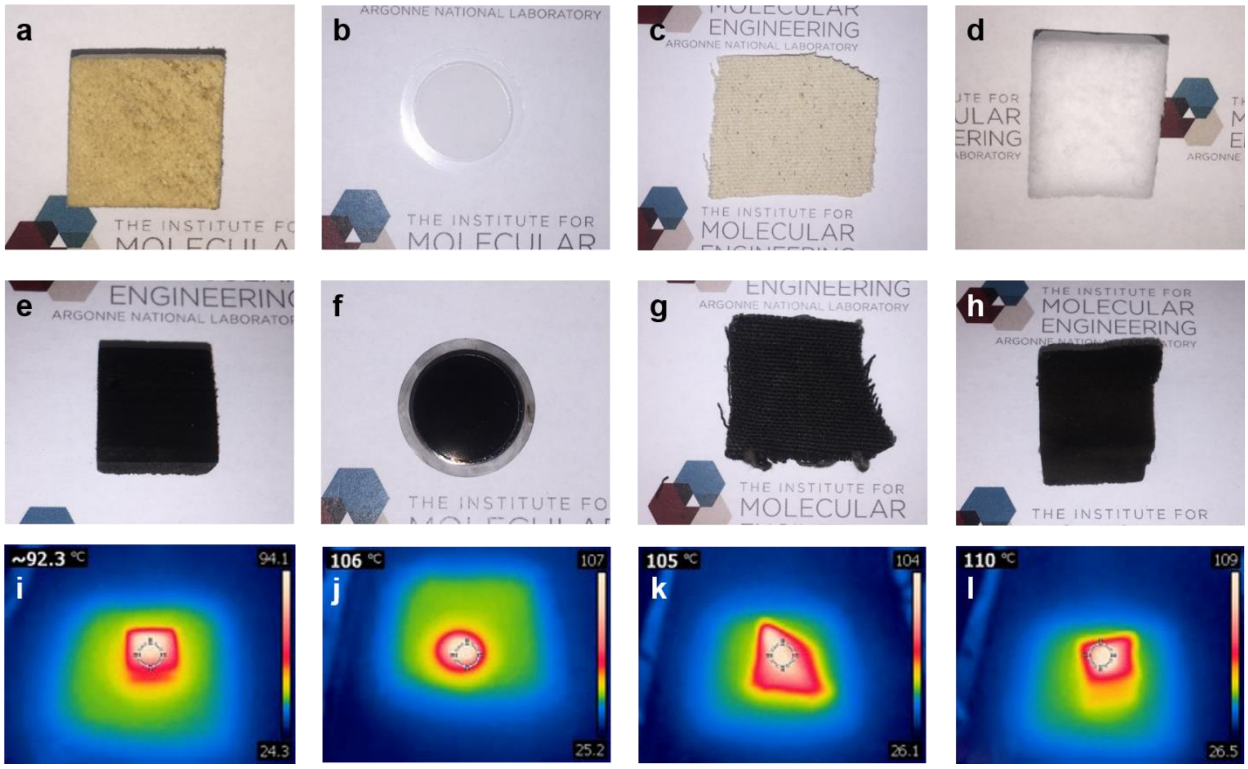

Figure 2.4: Digital pictures of various materials (wood, AAO membrane, fabric, and sponge) a-d) before and e-h) after in situ POF growth. i-l) Infrared images of POF-based materials under simulated sunlight.

The surface morphologies of templates@POF before and after in situ growth were observed by field-emission scanning electron microscopy (FESEM) (Figure 2.5). The nascent template materials exhibit porous or layered structures. POF particles were dispersed evenly on the surfaces of the templates. In this study, all reactions were consistently maintained at 80 °C for 24 hours. The morphology of the scaffolds is unaffected by the synthesis process, other than the appearance of adhered POF particles. The structure of the surface-bound POF particles themselves is also the same as the POF grown in solution (Figure 2.2). X-ray diffraction (XRD) data are shown in Figure 2.6, which shows almost same structure as previous work.[95]

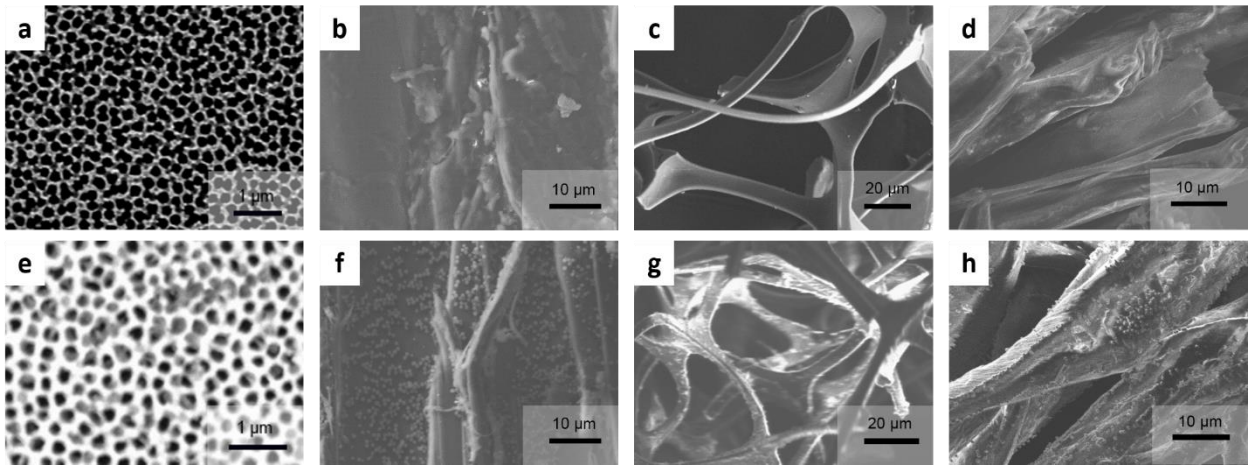

Figure 2.5: SEM images of AAO membrane, wood, sponge, and fiber before and after in situ growth of POF. a-d) are pristine AAO membrane, wood, sponge, and fiber. e-h) are respectively AAO@POF, wood@POF, sponge@POF, and fiber@POF.

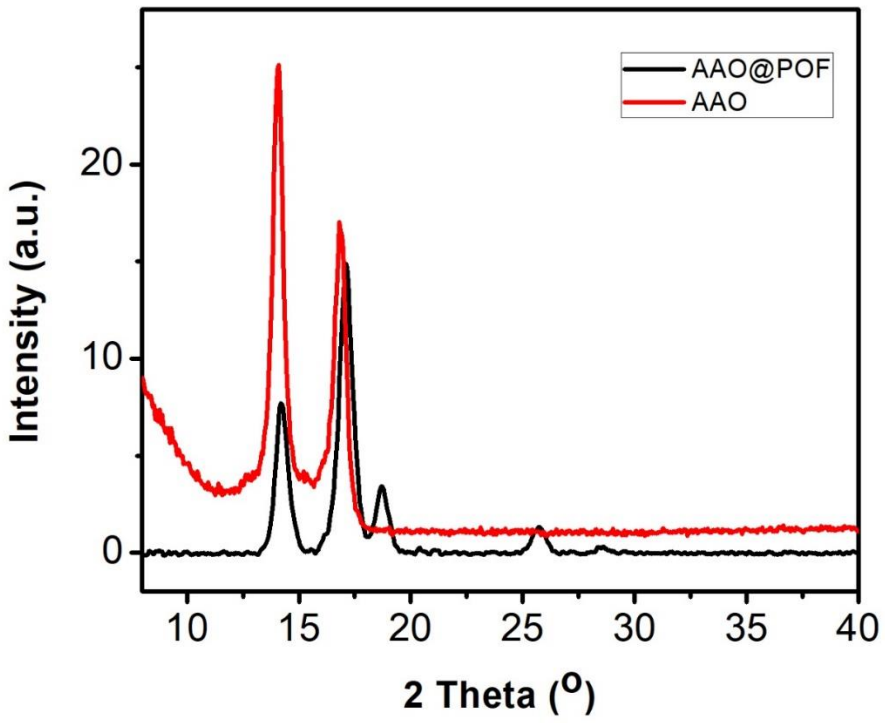

Figure 2.6: XRD spectrum of AAO membrane and AAO@POF

2.2.2 UV-Vis Spectra of POF Particles and Templates@POF

The UV-vis spectrum of POF particle solution (Figure 2.7 a) shows increasing absorption from the UV region to visible region. Time-dependent plane wave (PW) density functional theory (DFT) calculations (Figure 2.8) of POF light absorption also display broad harvesting across the visible and NIR range. The optical properties of templates@POF were also investigated using a UV-vis/NIR spectrometer (Figure 2.7 b, Figure 2.8). In the case of AAO, the nascent material displays negligible absorption over the entire range of wavelengths, as expected from the visible white appearance (Figure 2.7 b). After coating with POF particles, however, the AAO membrane turned black and exhibited a dramatic change in light absorption. The UV-vis spectrum of the POF-coated AAO shows low total reflectance, and the measured transmission is negligible. As a result, the light absorbance of the POF membrane is above 95% over the wavelength range from 300 to 1300 nm, which captures the vast majority of the spectrum of sunlight irradiation. It should be mentioned that the microfiltration membrane surface is relatively smooth on optical length scales, and the reflectance can, therefore, be further reduced by using substrates with macroscopically rough structures such as sponge or wood. After in situ growth of POF, wood, sponge, and fabric all showed much higher absorption ability than the respective nascent materials (Figure 2.9).

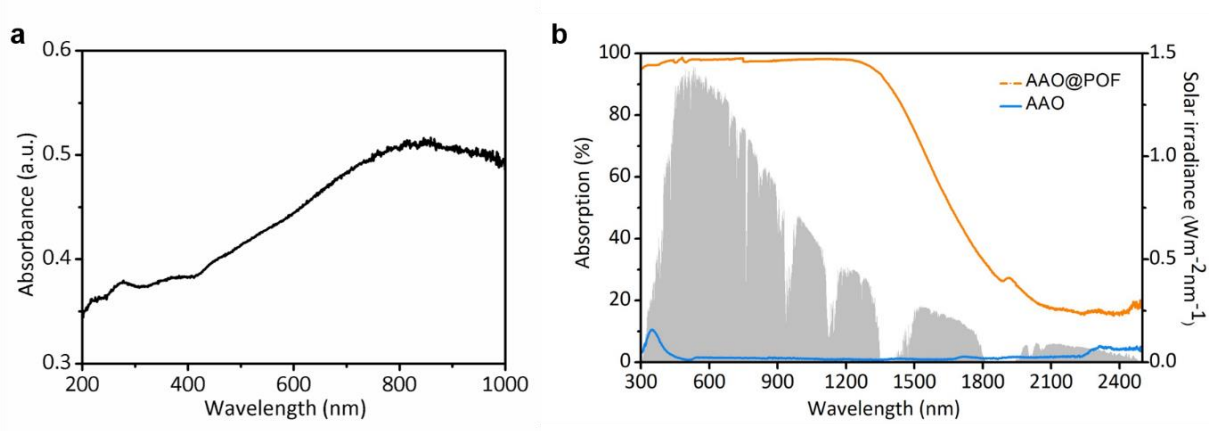

Figure 2.7: a) UV-vis spectrum of POF particle solution. b) UV-vis/NIR spectra of pristine AAO membrane and POF-based AAO membrane, with the AM1.5 standard sunlight spectrum overlaid in gray for comparison.

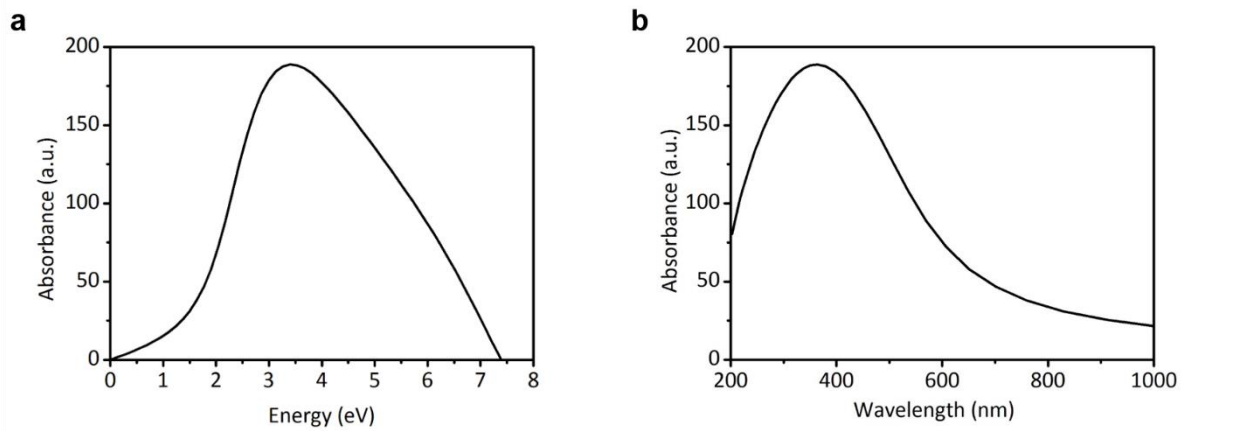

Figure 2.8: PW DFT calculation result of POF light absorbance a) with energy dispersion and b) with wavelength dispersion.

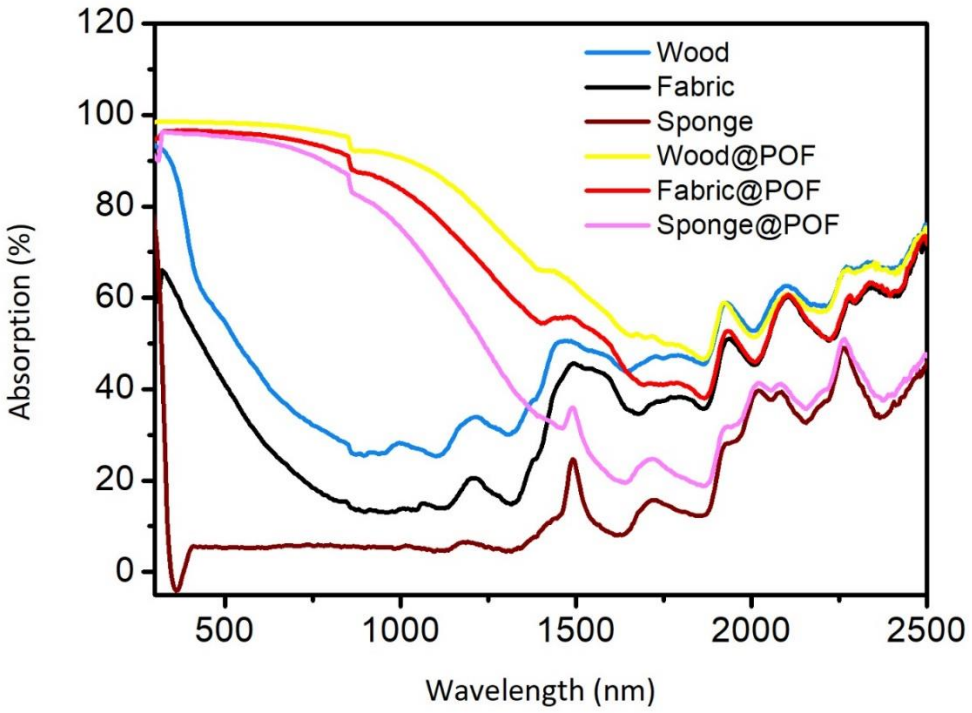

Figure 2.9: UV-vis/NIR spectra of wood, fabric and sponge materials before and after in situ growth of POF.

2.2.3 Evaporation Performance of POF-Based Absorbers

To demonstrate the evaporation performance, POF-based absorbers were floated on water and placed under simulated sunlight illumination. In this work, the optical concentration, C_{opt}, is 1.6. Figure 2.10a schematically illustrates the mode of operation of such a solar steam generator. When light from the solar simulator illuminates the surface of the POF-based material, the optical energy is converted into heat, which is transferred to the water within the material's pores, thereby accelerating evaporation. As low density, good absorption, porous structure, and low thermal conductivity lay a solid foundation for efficient solar steam generation, we highlight the evaporation performance of wood@POF. As shown by infrared imaging in Figure 2.10b, the

heat was localized on the surface (water-air interface) of the template@POF material. The surface temperature of wood@POF raised quickly with illumination, reaching 45 °C in 20 minutes, while bulk water will only achieve 33 °C in a comparable time period (Figure 2.10c). This temperature rise is non-linear. In the initial two minutes, the surface temperature of wood@POF increased to 36.8 °C from 21.8 °C, corresponding to a change rate more than three times that of bulk water (22.3 °C to 26.5 °C).

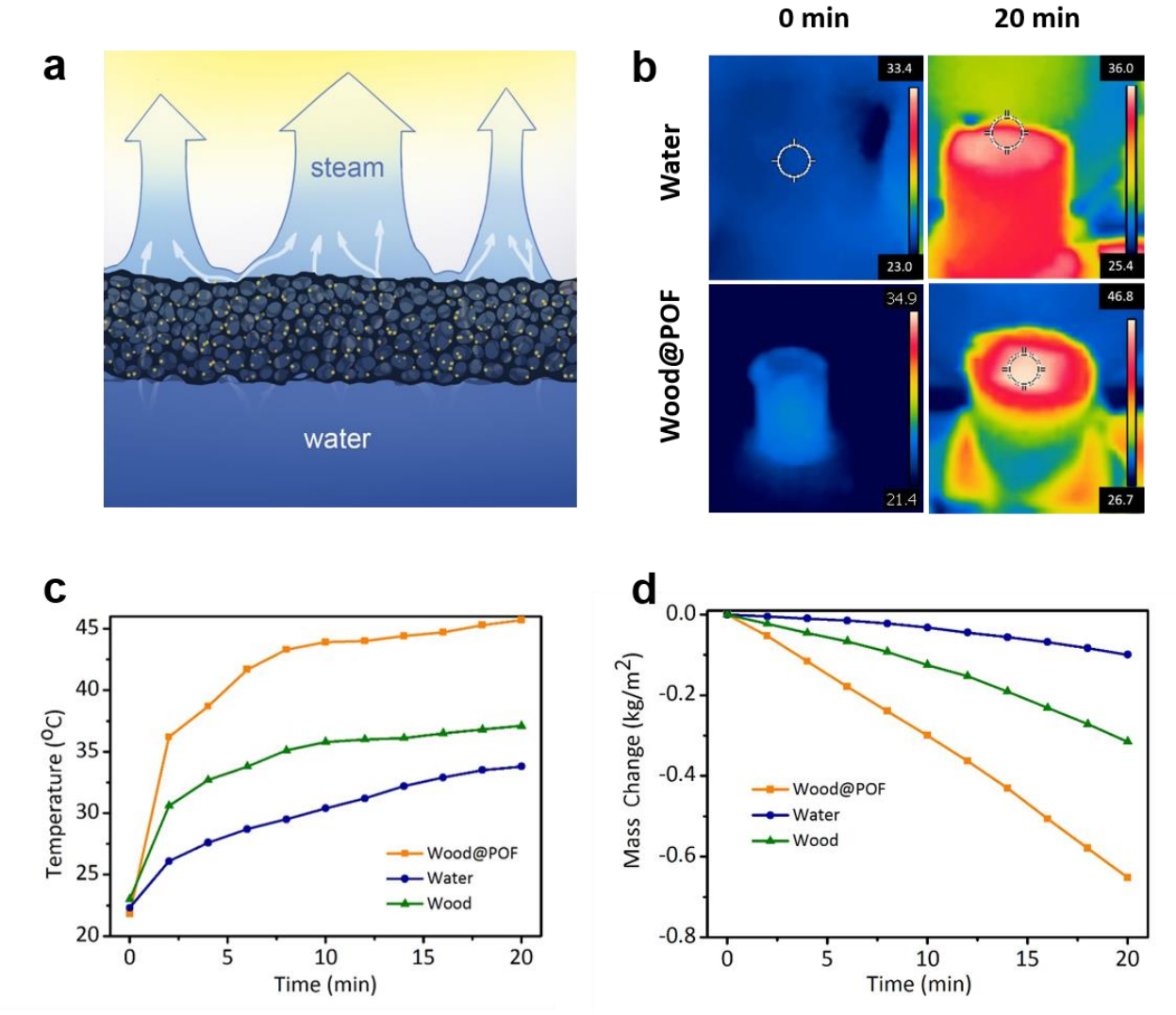

Figure 2.10: a) Scheme of water evaporation through the POF-based materials. b) Infrared images of beakers of water with and without POF-based wood before and after simulated

sunlight irradiation. c) Temperature change and d) mass change of beakers with only water, floating wood on water, and POF-based wood on water.

The evaporation tests were performed under simulated sunlight illumination (1.6 Suns intensity in this work). The water evaporation rate associated with wood@POF is 1.95 ± 0.06 kg m^{-2} h^{-1}. As a comparison, the evaporation of pure water and uncoated wood under the same condition are also recorded, 0.30 and 0.94 kg m^{-2} h^{-1}, respectively. Clearly, the evaporation efficiency of wood@POF far surpasses that of both pure water and bare wood, as expected from the enhanced light harvesting. The steam generation efficiency can be calculated by the following equation:[99]

$$\eta = \dot{m} h_{LV} / C_{opt} P_0$$

Where $\dot{m}$ refers to the mass change rate, h_{LV} to total enthalpy of sensible heat and the liquid–vapor phase change enthalpy, C_{opt} to the optical concentration, and P_0 the nominal solar irradiation value of 1 kW m^{-2}. Thus, the calculated evaporation efficiency is 79.6 ± 3.0 % for wood@POF. This high performance is not only attributed to the POF molecular structure itself, but also the in-situ growth method, which preserves the nature of hierarchical cellulose-based structure and low thermal conductivity.

2.2.4 Long Term Stability of POF-Based Materials

After the evaporation tests, we investigated the structures of wood@POF, also AAO@POF, sponge@POF, and fiber@POF after solar irradiance. These materials show no obvious difference after solar irradiance or solar steam generation as shown in Figure 2.11.

Operational lifetime is indeed an important performance aspect for solar steam generators. A full evaluation of this for the POF-based materials would be beyond the scope of this initial report, but we have performed some preliminary experiments for evaporation of simulated seawater (0.6 M NaCl). After 20 minutes of evaporation, there is no apparent effect on the photothermal surface. However, after 5 hours, salt crystals do begin to appear on the surface. These results are included in Figure 2.12.

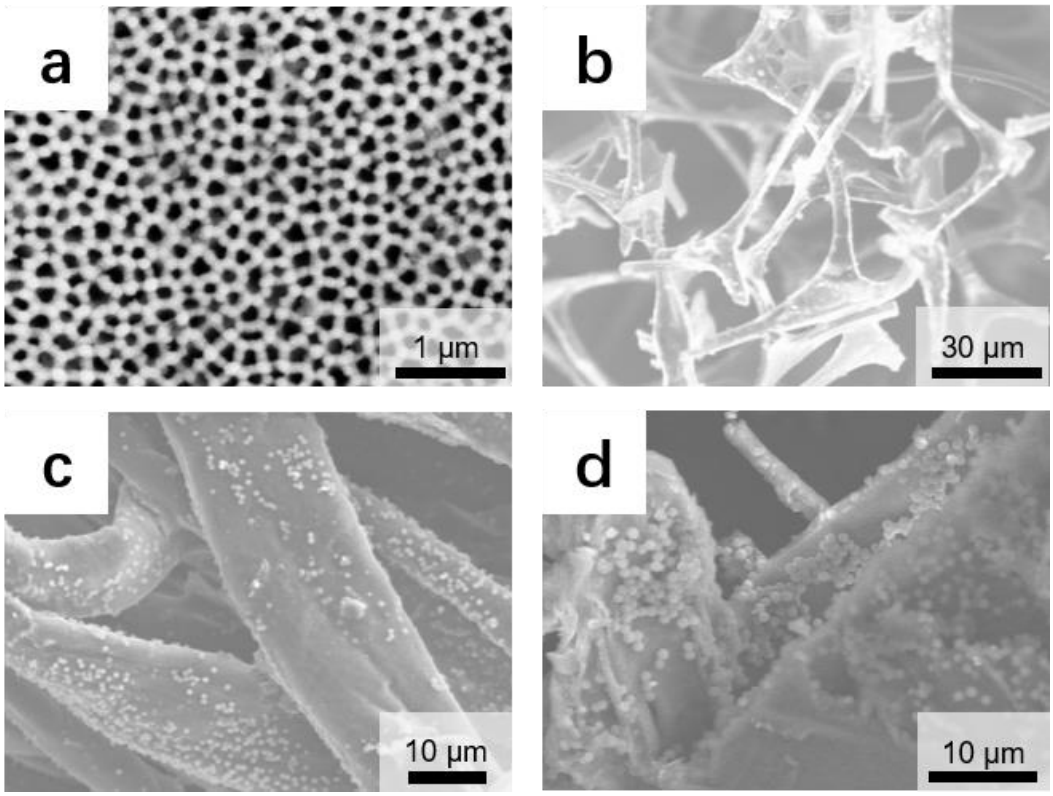

Figure 2.11: a-c) SEM images of AAO@POF, sponge@POF, and fiber@POF after solar irradiance treatment. d) SEM image of wood@POF after solar steam generation. These materials show no obvious difference after solar irradiance or solar steam generation.

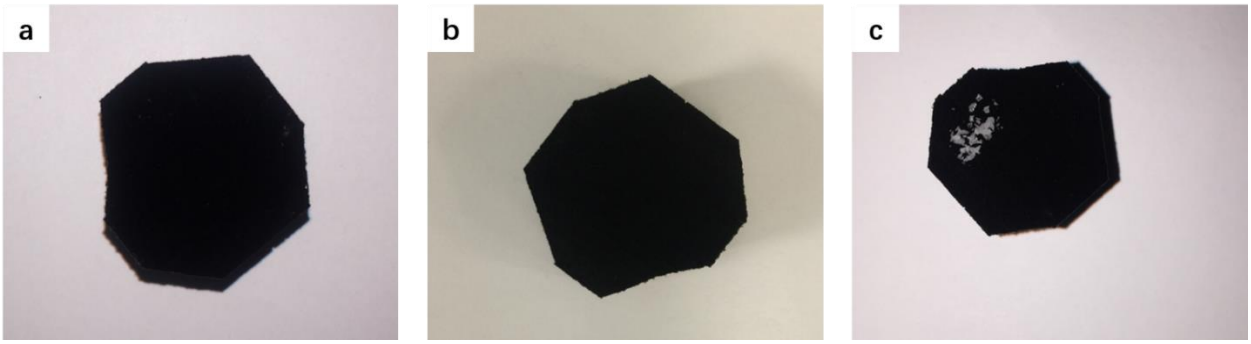

Figure 2.12: Digital image for wood@POF after solar steam generation for 20 minutes in a) deionized water, b) 0.6 M NaCl solution. No salt crystals appear on the surface. c) Digital image for wood@POF after solar steam generation for 5 hours in 0.6 M NaCl solution. Salt Crystals appear on the top surface of wood@POF.

2.3 Conclusions and Perspectives

In summary, we have demonstrated a universal, simple, and scalable interface engineering strategy for the fabrication of a solar steam generator based on POF material. POFs can uniformly in situ grow on the surface of diverse materials with a range of different porosities and hydrophilicity. Wood@POF, using wood as the template, shows about 80% overall efficiency for steam generation under 1.6 Suns illumination. Table 2.1 compares the water evaporation efficiency of this wood@POF with some other photothermal materials. This high performance is attributed to both the superior qualities of wood materials as a scaffold material and the exceptional solar absorptivity of POF particles. This method was also demonstrated with other templates, including sponge@POF, fabric@POF, and membrane@POF. They are all promising candidates as solar steam generators, with the selection of material for a specific application guided by availability, cost, and other factors. POF-based interface engineering design provides a pathway for the scalable fabrication of solar steam generators, with potential ramifications for desalination, wastewater treatment, and beyond.

Table 2.1: Water evaporation efficiency for different photothermal materials under different suns.

Materials	Suns	Efficiency	Reference
Wood@POF	1.6	80%	This work
3D-CG/GN	1	85.6%	Ref. [74]
CNT-silicon	1	82%	Ref. [76]
Graphene Foam	1	90%	Ref. [77]
GDY/CuO nanowires	1	91%	Ref. [78]
Plasmonic wood	10	85%	Ref. [81]
MXene Ti3C2	1	84%	Ref. [82]
Chinese ink	1	82%	Ref. [88]
Carbon foam/ graphite	1	64%	Ref. [99]
	10	85%	
Black Titania	1	70.9%	Ref. [83]
Au/NPT	4	90%	Ref. [80]
Carbonized mushrooms	1	78%	Ref. [73]
Graphitized carbon black	10	69%	Ref. [85]

COFs, due to their high porosity, highly organized pore structures, adjustable chemostability, tunable surface properties, and controllable aperture size, have been demonstrated in research labs for water treatment applications in desalination, organic contaminant removal, metal ion capture, as well as in several additional emerging areas.

COFs with highly uniform and ordered aperture size provide passages that can, in principle, deliver ultrahigh-selectivity molecular sieving. Defect-free COF thin membranes can be assembled onto UF substrates as a selective layer, and COF powders can be used as nanofillers in active layers of MMMs. COFs particles are often implemented as adsorbents because of the high surface area and abundant surface active sites (chelating sites) for heavy metal ions, radioactive ions, or organic pollutants. The design and the introduction of surface functionality govern the adsorption performance of COFs. COFs with broad sunlight wavelength absorption property and photothermal conversion efficiency have shown potential for solar steam generation, and the use of COFs as photocatalysts or capacitive deionization electrodes materials has only just begun.

The history of COFs materials for water treatment is only about five years old; the opportunities going forward are vast, presuming detailed foundational studies continue. Much remains to be learned about the relationships between COF structure and performance/properties. The mechanism of ion adsorption in COFs, development of tailored active sites for selective ion capture, and the role that COFs particles play as nanofillers during separation processes still need further investigation. With more in-depth understanding of the relationship between performance and structure, more COF-based materials could be designed and explored effectively for water treatment. A closely related application space is in sensor technology, where selectivity of adsorption is also paramount. This is a topic ripe for additional exploration.

COF applications in desalination have only recently begun. Computational results hint at tremendous promise, but the practical use of COFs as sieving channels has been limited because this process relies on a difficult-to-achieve aperture size (less than 1 nm). Post-synthesis methods may be utilized by anchoring side groups on the interior pore walls. There is still a pressing need for stable COF membranes with high salt rejection and relatively high flux.

COF particle adsorbents have displayed limited practical use to date, but introducing COF adsorbents into membrane technology may be beneficial for ion adsorption performance. Generally, technoeconomic assessment will be essential, as COF syntheses may cost more than current commercial materials. Guided by such analysis, new fabrication methods with cost-effective and large-scale fabrication strategies could be developed for industrial applications. Moreover, COF environmental compatibility has not been investigated yet; environmental risk assessment should be considered before practical applications.[113] Reusability and long-term operational stability of COF-based membranes and adsorbents will also need to be realized to enable most real-world applications. We note that COF-based materials are still absent in some other significant areas of water treatment, such as electrodialysis and membrane distillation, which may offer some interesting opportunities as well.

With more comprehensive understanding of the structure-performance relationships present in this diverse class of materials, COFs may indeed play an important role for water treatment in the future. As new COF platforms are developed, including engineering of their interfacial charge and chemistry,[114] it is certain that there will be exciting new discoveries with untold impact in addressing our society's water challenges.

2.4 Experimental Section

Fabrication of Templates@POF. The AAO and PVDF membranes were purchased from Sterlitech (USA) and MilliporeSigma (USA), respectively. The cotton fabric, melamine sponges, and basswood were obtained from Fisher Scientific (USA). The terephthalaldehyde, pyrrole, trifluoroacetic acid (TFA), nitrobenzene, and acetic acid were purchased from Sigma-Aldrich (USA). Templates@POF were synthesized using a one-pot method. An acid-catalyzed dehydration reaction leads to uniform in situ growth on a variety of different substrates. The selected substrate material (AAO membrane, fabric, sponge, or wood) is trimmed as needed to achieve the desired form factor and placed into the reactor. 100 mL acetic acid is added to the vessel, followed by addition of 50 μL TFA to serve as an acid catalyst. Next, 22.72 μL pyrrole, 300 μL nitrobenzene, and 23.44 mg terephthalaldehyde are mixed with the suspension. The as-obtained mixture was kept at 80 °C under continuous magnetic stirring for 24 h and then cooled down to room temperature. The black products were washed using acetone, isopropyl alcohol, and deionized water twice. Ultrasonic cleaning for 30 minutes served to remove any weakly bonded POF particles. After drying in a vacuum oven at 100 °C for 2 hours, the black templates@POF were obtained for further characterization.

Characterization. The particle size distribution was detected by a particle size analyzer (Zetasizer Nano, Malvern). The surface structures and morphologies of templates@POF and pristine templates were characterized using a JSM7500F (JEOL Ltd., Tokyo, Japan) field emission scanning electron microscope (FE-SEM) at 3.0 kV. The UV-Vis-NIR reflection and absorption spectra of templates@POF and POF solution were collected using an UV-Vis-NIR spectrometer (Lambda 950, PerkinElmer). The infrared images were taken with a FLIR C2 Compact Thermal Imaging Camera, and the temperature vs. time data were collected using an

infrared gun. The water evaporation tests were all conducted using a solar simulator (Oriel 300 W, Newport). In the experiment, we put wood or wood@POF in a 20 mL beaker full of deionized water. The outer wall of the beaker was covered with an opaque layer to make sure the light only input from the top of the beaker. Because the wood was a little smaller than the opening area of the beaker, a polypropylene mask combined with heat-insulating film was used to cover the remaining exposed water surface. Evaporation was quantified by measuring the mass loss using a precision balance.

Density Functional Theory. The QUANTUM ESPRESSO package[100] was applied. SG15 ONCV pseudopotential[101] is used for all elements. The exchange-correlation part of the density functional was treated within the generalized gradient approximation (GGA) of Perdew–Burke–Ernzerhof (PBE).[102, 103] The cut-off energy for the plane-wave basis was 50 Ry. The basic calculations were performed in the unit cell consisting of 54 atoms ($C_{32}N_4H_{18}$), with a k-point mesh of 5×5×1, and the total energy is converged to 1×10^{-4} eV.

Chapter 3: TUNABLE ION TRANSPORT WITH FREESTANDING VERMICULITE MEMBRANES

Membranes integrating two-dimensional (2D) materials have emerged as a category with good ion transport and separation applications in both aqueous and non-aqueous systems. The interlayer galleries in these membranes drive separation and selectivity, with specific transport properties determined by the chemical and structural modifications within the inherently different interlayers. Here we report an approach to tuning interlayer spacing with a single source material—exfoliated and restacked vermiculite with alkanediamine crosslinkers to both control the gallery height and enhance the membrane stability. The as-prepared crosslinked 2D vermiculite membranes exhibit ion diffusivities tuned by the length of the selected diamine molecule. The 2D nanochannels in these stabilized vermiculite membranes enable a systematic study of confined ionic transport and may provide a pathway for applications of 2D material membranes in water treatment, energy storage, and beyond.

3.1 Introduction

Membrane technology has proven viable in water purification and other separation applications with decades of productive use. As a process without the requirement of phase change, it involves low energy input, high efficiency, and continuous operation.[104, 105, 106, 2, 107] However, membrane technology continues to struggle with the challenge of trade-offs between selectivity and permeability.[108] Most methods to increase selectivity (e.g., narrowing pore size) inevitably decrease the permeability; reducing the membrane thickness to increase permeability

will generally decrease selectivity due to inevitable pore size variations. There has been only limited success in pushing the boundaries of these trade-offs with advanced membrane materials. Molecular-sieving fillers with nanostructuring (e.g., nanocrystals or 2D nanosheets) can simultaneously improve both permeability and selectivity.[109, 110] Anomalous transport phenomena observed with 2D material membranes, such as ultrafast water transport[111, 112] and selective ion transport[113, 114] in particular, have attracted attention for promising applications in water treatment. To date, graphene oxide (GO) and other graphene family materials have been the primary focus for researchers in this field.[115, 116] Beyond the graphene family, boron nitride[117], MXenes[118], transition metal dichalcogenides (TMDs) such as MoS_2 [119] and WS_2 [120], and layered double hydroxides (LDHs)[121] have also been explored. Each of these classes of materials carries challenges in translating laboratory-scale studies to practical technological applications:

(1) During typical exfoliation processes, acids, oxidants, or solvents are used to break the bonding between layers, which carry adverse environmental impacts. (2) For some 2D materials, precursor materials are limited in supply and therefore expensive. (3) For practical application as separation membranes, long-term water stability and chemical resistance are important factors to be considered, and some 2D materials will evolve in aqueous environments due to oxidation or hydroxylation of the surface functional groups and other reactive species.

Clay minerals are naturally occurring phyllosilicates that can be found in sedimentary rocks and hydrothermal deposits and have found widespread applications from the beginning of human civilization.[122] Vermiculite, $Mg_{0.7}(Mg,Fe,Al)_6(Si,Al)_8O_{20}(OH)_4 \cdot 8H_2O$, is a hydrous layered aluminosilicate compound with each layer composed of one Mg (or Fe)-based octahedral sheet sandwiched between two tetrahedral silicate sheets (Figure 3.1a).[123] The global production of vermiculite is approximately 0.5 million tons with the average price of around $350 per ton,

suggesting a plentiful and low-cost source material.[124] Vermiculite layers have strong negative surface charge, which is typically compensated by hydrated cations in the interlayers.[122,125] These interlayer cations enable simple exfoliation of vermiculite via ion exchange.[126] Vermiculite also has extraordinary water and chemical stability.[125, 127] Although the layered structure has been recognized since the 1990s, vermiculite's primary application is in traditional industries such as construction. Membrane applications have only emerged in recent years. Vermiculite membranes have shown promising potential in batteries[128, 129] and water treatment[125, 127, 130].

In the quest to overcome the selectivity-permeability trade-off, attention has turned primarily to engineering improved selectivity. For many applications, the challenge centers on tuning selectivity in the nanofiltration regime, roughly spanning the range of 0.5-10 nm. Ideally, a high-performance membrane will have transport channels with uniform size, chemistry, and charge to maintain the maximal permeability for a given size/charge exclusion behavior. In this work, we successfully demonstrate a route to *tunable* ion-transport properties of vermiculite membranes (VMs) by introduction of alkanediamine molecules to crosslink the layers (Figure 3.1b), which also enhances the water stability. We show that the interlayer spacing can be tuned by introducing diamines of different molecular length. The crosslinked VMs exhibit distinct ion-separation performance, dictated by a combination of the tuned layer spacing and interlayer (negative) surface charge. The methodology outlined here could likely be extended to other layered materials having different inherent layer spacing and electrostatic properties and therefore represents a pathway for designing a diverse range of 2D membrane materials with tunable ion transport.

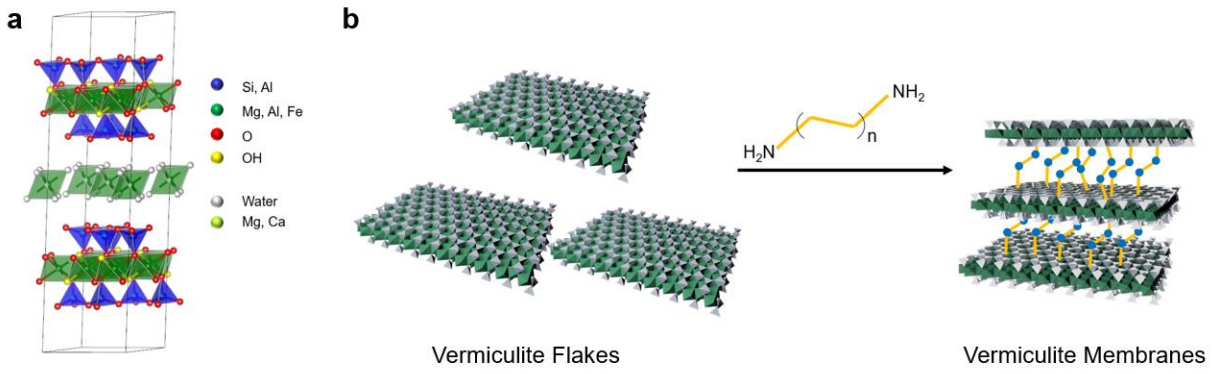

Figure 3.1: a) Crystal structure of vermiculite, which contains two tetrahedral sheets with an octahedral sheet, and balance of hydrated cations (Mg^{2+}/Ca^{2+}/Fe^{2+}) between layers. b) Schematic illustration of the fabrication process of an alkanediamine crosslinked VM (xDAVM).

3.2 Results and Discussion

3.2.1 Fabrication and Characterization of Vermiculite Membranes

Stable aqueous dispersion of vermiculite flakes was prepared from thermally expanded vermiculite crystals by two steps of ion exchange, as reported previously.[126, 122] Process details are provided in the **Experimental section**. Optical images of thermally expanded bulk vermiculite (Figure 3.2a) indicated the multilayered structural nature of the raw mineral. Flexible, thin, free-standing VMs (Figure 3.2b) are readily achieved by vacuum filtration of the exfoliated material. Cross-section scanning electron microscopy (SEM) images of a VM (Figure 3.2c) reveal its lamellar microstructure. The final thickness of such VMs is determined by the concentration and volume of vermiculite colloidal dispersion used in the vacuum filtration process. Restacked vermiculite has a relatively uniform interlayer spacing with some variation owing to the presence of different balancing cations, different degrees of hydration, and stacking disorder. As shown in Figure 3.2d, the X-ray diffraction (XRD) pattern of VMs in this work has a strong peak at 7.1°, corresponding to the {001} *d*-spacing of 12.4 Å. Figure 3.2e is an atomic

force microscopy (AFM) image of typical exfoliated vermiculite flakes. The height profile extracted from this image (Figure 3.2f) shows that the thinnest layer of flakes is around 1.2 nm, corresponding to the monolayer height of exfoliated vermiculite.

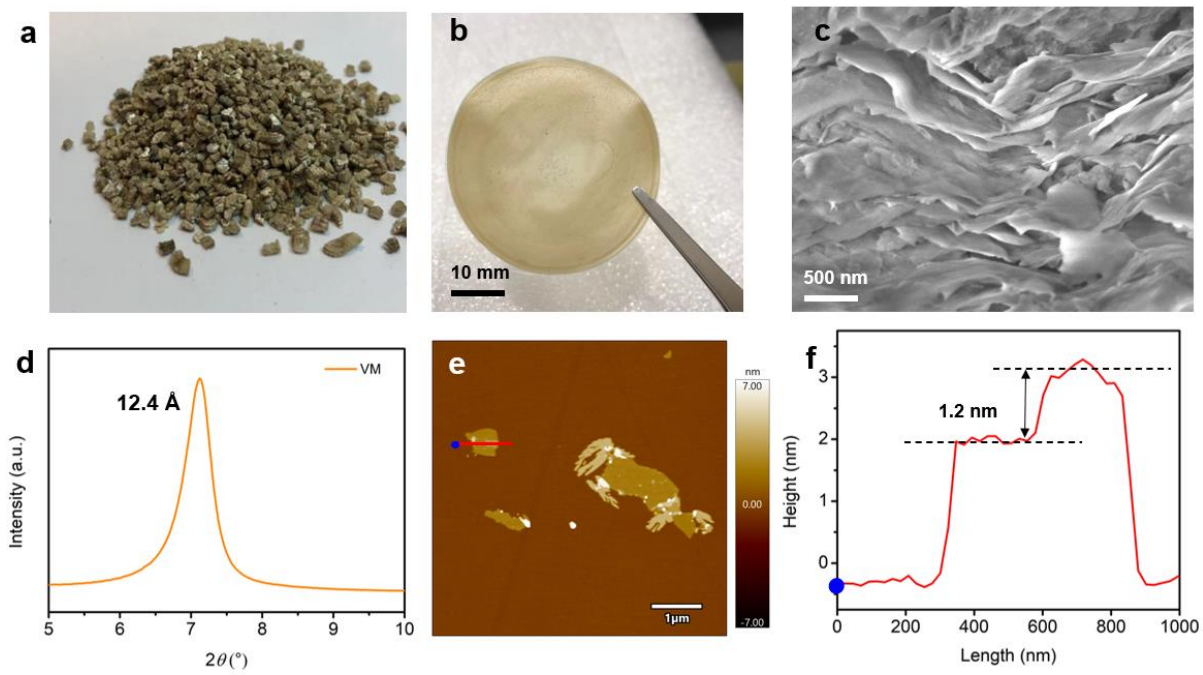

Figure 3.2: Exfoliation of bulk vermiculite and the fabrication of free-standing vermiculite membranes. a) Thermally expanded bulk vermiculite, which can be exfoliated by two steps of ion exchange. b) Flexible free-standing vermiculite membrane fabricated by vacuum filtration. c) Cross-section SEM image of a VM. d) XRD scan of a VM showing the {001} layer spacing. e) AFM topography image of exfoliated vermiculite flakes, and f) Line scan extracted from AFM data showing the monolayer height.

3.2.2 Crosslinked Vermiculite Membranes

To demonstrate the concept of alkanediamine crosslinking of vermiculite sheets, three different diamines are chosen: 1,2-ethanediamine (EDA), 1,4-butanediamine (BDA), and 1,6-hexanediamine (HDA). Following membrane fabrication (see Methods), three free-standing crosslinked VMs are obtained successfully (Figure 3.3). The morphology and the surface

structure of as-fabricated diamine-crosslinked vermiculite membranes (xDAVMs, x=E, B, or H) exhibit no qualitative change compared with the uncrosslinked VM (Figure 3.4a-f). The diamine modified VMs retain the lamellar microstructure, as shown in cross-section SEM images.

Figure 3.3: Optical images of crosslinked EDAVM, BDAVM, and HDAVM.

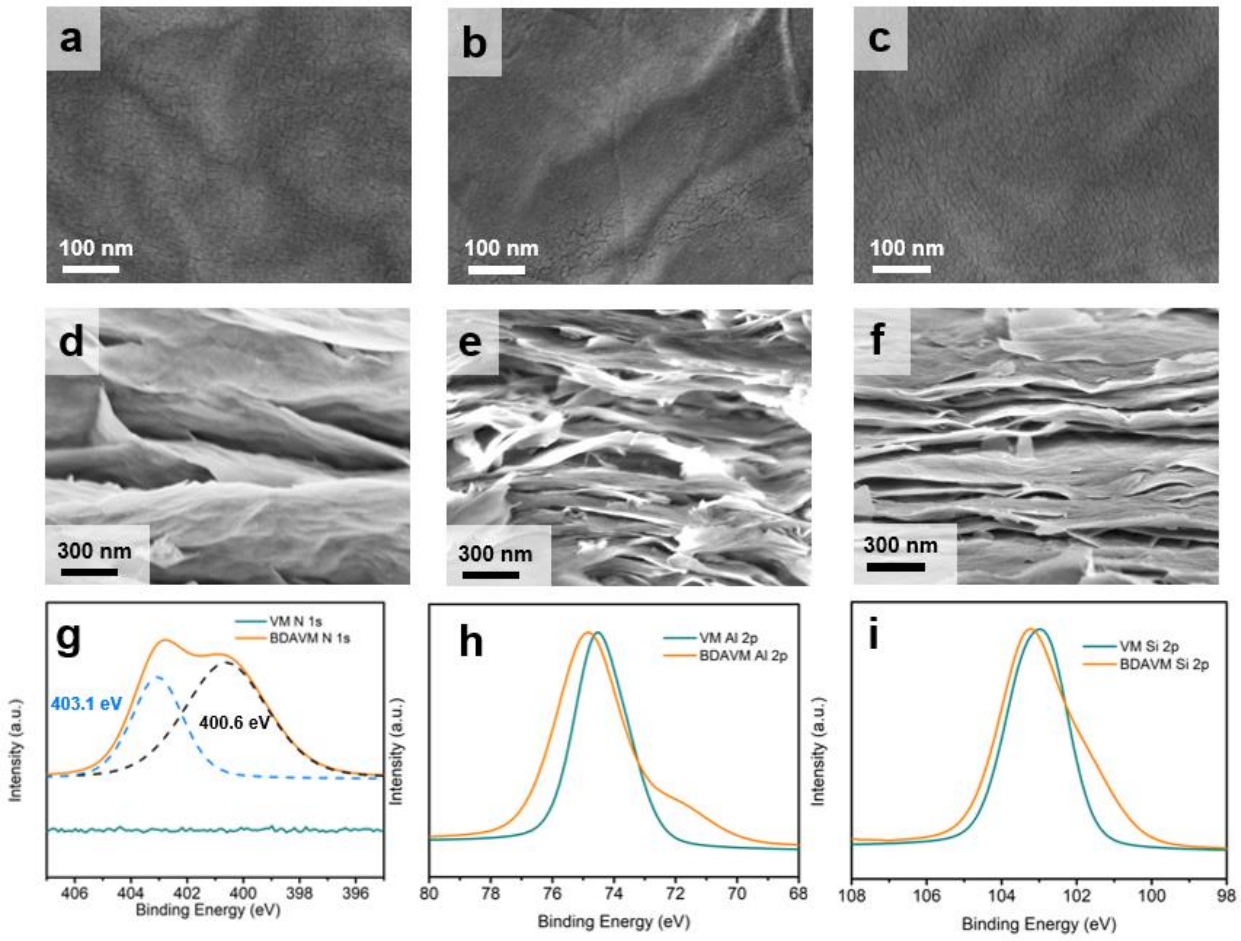

Figure 3.4: a-c) Top-view SEM images of EDAVM, BDAVM, and HDAVM. d-f) Cross-section SEM images of EDAVM, BDAVM, and HDAVM. g) XPS spectra of N1s of VM and BDAVM showing the integration of diamines in the latter. h) XPS spectra of Al 2p of VM and BDAVM. i) XPS spectra of Si 2s of VM and BDAVM.

To confirm the integration of diamines into the final membranes, X-ray photoelectron spectroscopy (XPS) measurements were carried out. Figure 3.4g exhibits the N 1s XPS spectra of VM and BDAVM; there is no nitrogen peak apparent for the original VM, whereas the BDAVM N 1s XPS spectrum indicates substantial presence of diamines in the material. The high-resolution N 1s peak in BDAVM membrane is broad and asymmetric. Curve deconvolution indicates two types of binding configurations for the nitrogen atoms and can be fitted for

unbound/free (-NH_2) and bound/crosslinked (-NH-) shifted to the high-binding-energy side.[131] The fitted XPS peaks at 400.6 eV and 403.1 eV likely correspond to C-NH_2 and N-O-Al/-N-O-Si/Al bonding, respectively. Depth profiling (Figure 3.5a) indicates that the diamines are both at the surface and within the bulk of the crosslinked vermiculite membranes. Based on XPS elemental analysis, the density of diamines linked to vermiculite interlayer surfaces is approximately 1-2.4 molecules per nm^2. The C/N ratio provides further evidence for VM crosslinking. We find good agreement between the experimentally determined and theoretically expected C:N values for BDAVM (observed = 2.16:1; theoretical = 2:1) and HDAVM (observed = 3.2:1; theoretical = 3:1) (Figure 3.5b). While we expect a C:N ratio of 1:1 for EDAVM membrane, the observed value was 0.4:1. Comparing the percent N/(Al+Si) values between the different alkanediamine crosslinked vermiculite membranes (Figure 3.5c), we found that EDAVM films yielded higher degree of crosslinking (38%) compared to BDAVM and HDAVM, which exhibited a similar degree of crosslinking (10%). The lower degree of crosslinking can be attributed to the molecular size-dependent steric hindrance of diamines (EDA, length = 3.7 Å; BDA, length = 6.2 Å; and HDA, length = 8.7 Å) limiting their access to the space between the vermiculite interlayers, attracted by long-range van der Waals attraction.[132] Further studies of crosslinking sites, crosslinking time, and crosslinker-VM interactions may be fruitful, particularly in terms of highlighting the factors affecting the degree of crosslinking. To explore the nature of the bonding between diamines and vermiculite layers, we examine the high-resolution Al 2p, Si 2p, and O 1s XPS spectra (Figure 3.4h, Figure 3.4i and Figure 3.6); the BDAVM Al 2p peak shifts from 74.5 eV to 74.8 eV, and the BDAVM Si 2p peak shifts from 102.5 eV to 103.2 eV. Also, the BDAVM O 1s peak shifts from 531.6 to 532.1 eV, which suggests the Al-O/Si-O in the tetrahedral layers is interacting with the diamine (Figure

3.1a shows the vermiculite crystal structure). (All spectra were referenced to the C1s peak at 284.8 eV.)

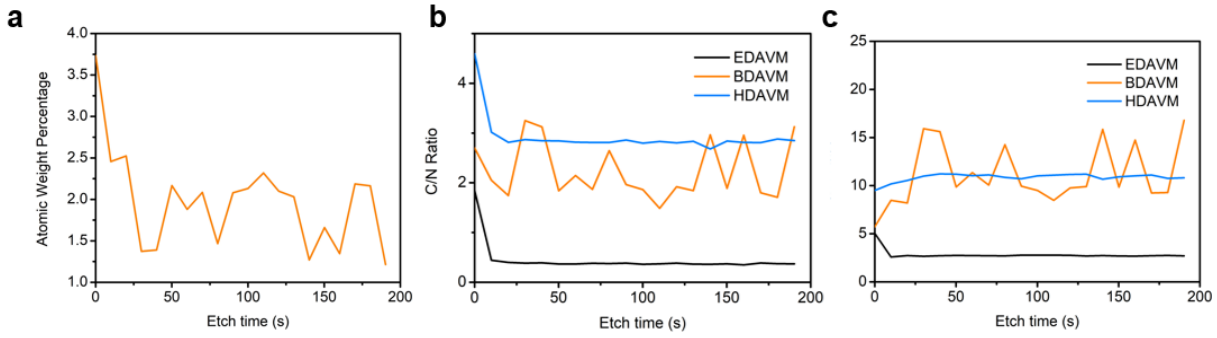

Figure 3.5: a) XPS depth profile of nitrogen element for BDAVM. b) C:N values for xDAVMs. c) (Al+Si):N values for xDAVMs.

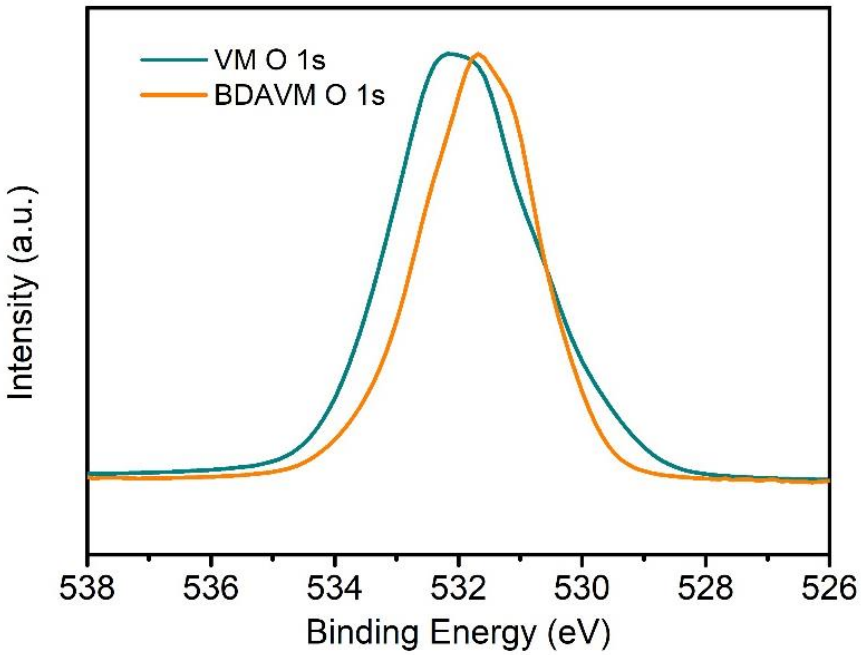

Figure 3.6: XPS spectra of O 1s of VM and BDAVM.

Extended membrane stability in aqueous environments is a critical prerequisite for application in water treatment. However, the as-synthesized, uncrosslinked VM is not stable in water. After submersion in deionized water (DI) for 20 minutes with mild shaking, the VM was redispersed in water because of its highly hydrophilic nature (Figure 3.7 and 3.8). In contrast, after crosslinking with diamines, the membrane water stability is enhanced. The thickness of HDAVM, for example, remains unchanged after extended submersion in water or in 0.1 M KCl aqueous solution (Figure 3.9).

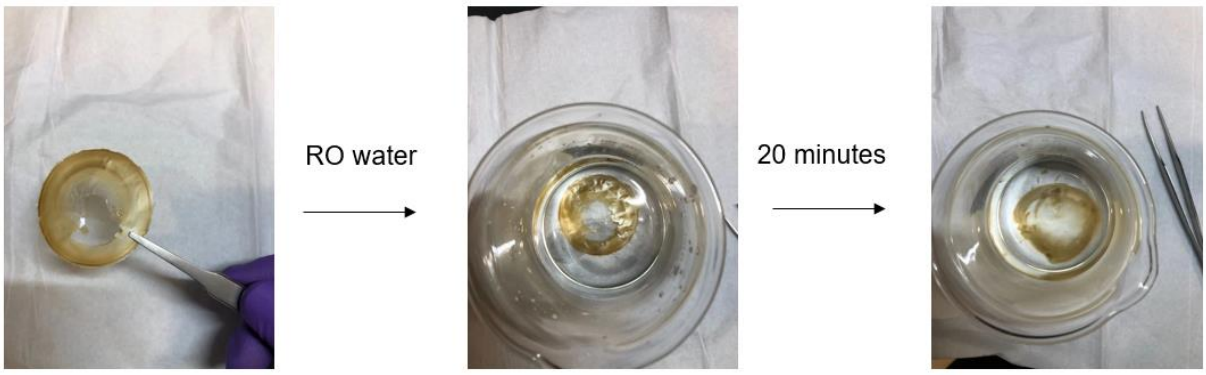

Figure 3.7: VM has poor water stability because of its highly hydrophilic nature.

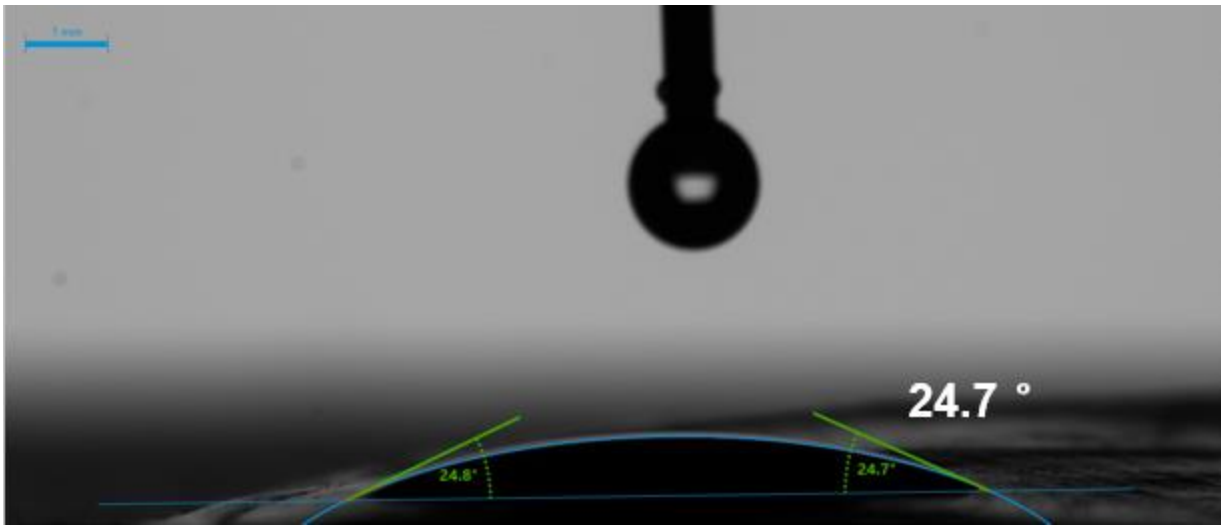

Figure 3.8: VMs are hydrophilic with a water contact angle of 24.7°.

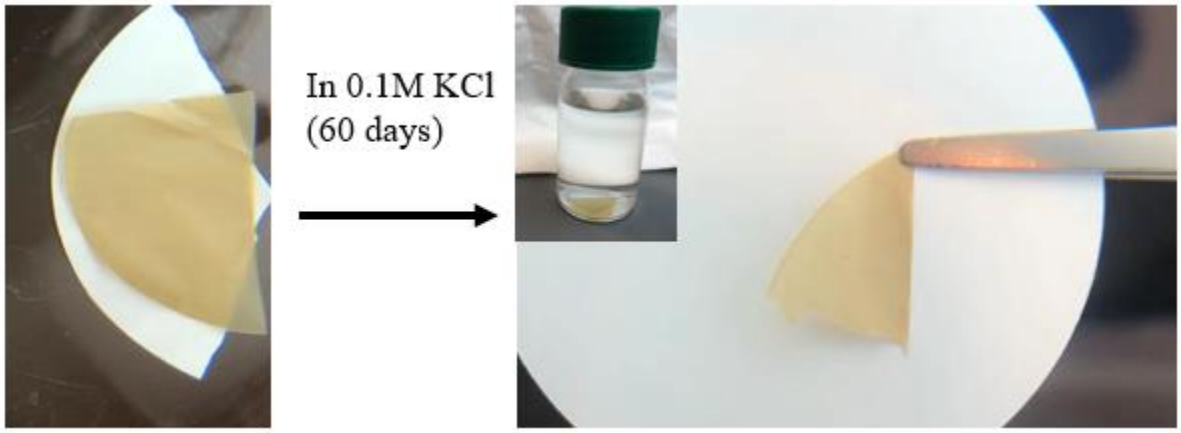

Figure 3.9: 10 μm HDAVM was soaked in 0.1 M KCl aqueous solution. After 60 days, the thickness remains 10 μm.

3.2.3 Water Permeance of xDAVMs

With the introduction of diamines, the interlayer spacing is modified. The measured *d*-spacings of VM, EDAVM, BDAVM, and HDAVM are 12.40, 12.87, 13.10, and 13.18 Å, respectively, when dry (Figure 3.10a). Hydration by soaking in DI water for 24 hours slightly increases the *d*-spacings of EDAVM, BDAVM, and HDAVM to 12.91, 13.14, and 13.22 Å,

respectively (Figure 3.11). As would be expected, the varying interlayer spacing correlates with different water permeance. Different crosslinked VMs were punch-cut to 25 mm standard membrane disks and tested using a lab-scale dead-end filtration system. After the thickness is normalized to 20 μm, the water permeance for EDAVM, BDAVM, and HDAVM are 17 ± 2, 40 ± 5, and 77 ± 3 L m^{-2} h^{-1} bar^{-1}, (Figure 3.10b) respectively, revealing the sensitive dependence of permeability on layer spacing.

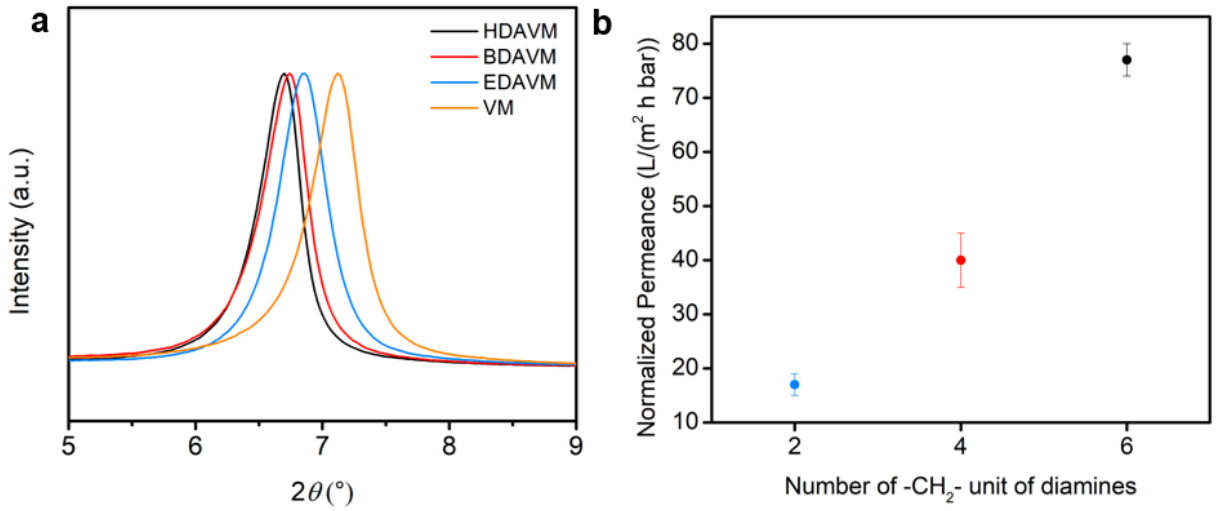

Figure 3.10: a) XRD data show that the interlayer spacing of VMs is systematically tuned by integrating different diamine crosslinkers. b) Water permeance through VMs correlates with the interlayer spacing.

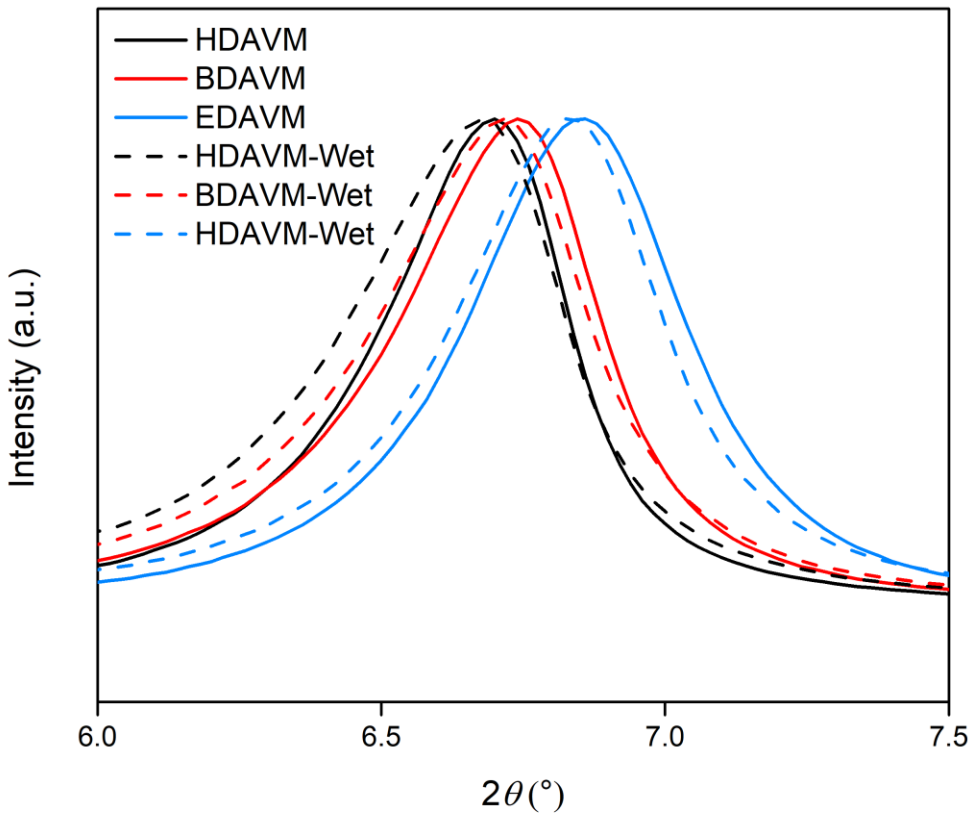

Figure 3.11: XRD patterns of xDAVMs in wet state (dash line) and ambient state (solid line).

3.2.4 Ion Transport of xDAVMs

With the ability to tune water permeability demonstrated, we turn our attention to characterization of the ion-transport properties of this xDAVM series to ascertain the potential for tuning sieving performance with different crosslinking species. Ion transport was performed with an H-cell permeability device using the concentration gradient as the driving force. The feed half-cell contained 90 mL 0.1 M of different salt solutions (KCl, NaCl, LiCl, $MgCl_2$, $CaCl_2$, YCl_3, K_2SO_4, or K_3PO_4), and the permeate half-cell was filled with the same volume DI water. Both sides of the H-cell were stirred at 400 rpm to minimize the potential influence of

concentration polarization. Ionic conductivity of the permeate solution was continuously recorded using a conductivity meter, and permeation rates were obtained based on a calibrated linear relationship between the conductivity and concentration of salt solutions. Inductively coupled plasma - optical emission spectrometry (ICP-OES) was used to confirm the reliability of this simple conductivity measurement method.

Permeation experiments of both some common anions and cations were performed. As shown in Figure 3.12a, the ion permeability for anions with various valences and sizes exhibit a clear trend of $Cl^- > SO_4^{2-} > PO_4^{3-}$. The diffusion of chloride ions is significantly faster than that of sulfate and phosphate because the transport is governed largely by a size-exclusion process, and chloride ions have the smallest size among this set. The larger negative charge of the multivalent anions likely also plays a role through Donnan effect, resulting from electrostatic interactions between solutes and membrane surfaces. Membranes with the same charge repel the ions while attract ions with opposite charge.[133, 134] Moreover, the ion permeability of an individual anion for different xDAVMs has the trend HDAVM > BDAVM > EDAVM. Because of the negative (repulsive) surface charge property of xDAVMs (see zeta potential data in Figure 3.13), and the fact that the interlayer spacing of HDAVM is larger than the other two membranes, HDAVM would be expected to exhibit the highest anion permeability.

Cations, in contrast, exhibit different behavior. Positively charged species transporting through xDAVMs face the same two mechanisms, namely, size exclusion and electrostatics, but the latter will be attractive in this case. This distinction appears to have a qualitatively different impact on ion transport because of the possibility for more significant dehydration of the diffusing ions. When cations pass through the nanochannels of VMs, the negatively charged nanosheets have strong electrostatic interactions upon them when the channel scale is on the

order of the Debye length, which is around 1 nm in this system (depending on the ionic strength for each electrolyte). As shown in Figure 3.12b, the ion permeability of individual cations for different xDAVMs often follows the same trend of HDAVM > BDAVM > EDAVM (although the difference between EDAVM and BDAVM is smaller).

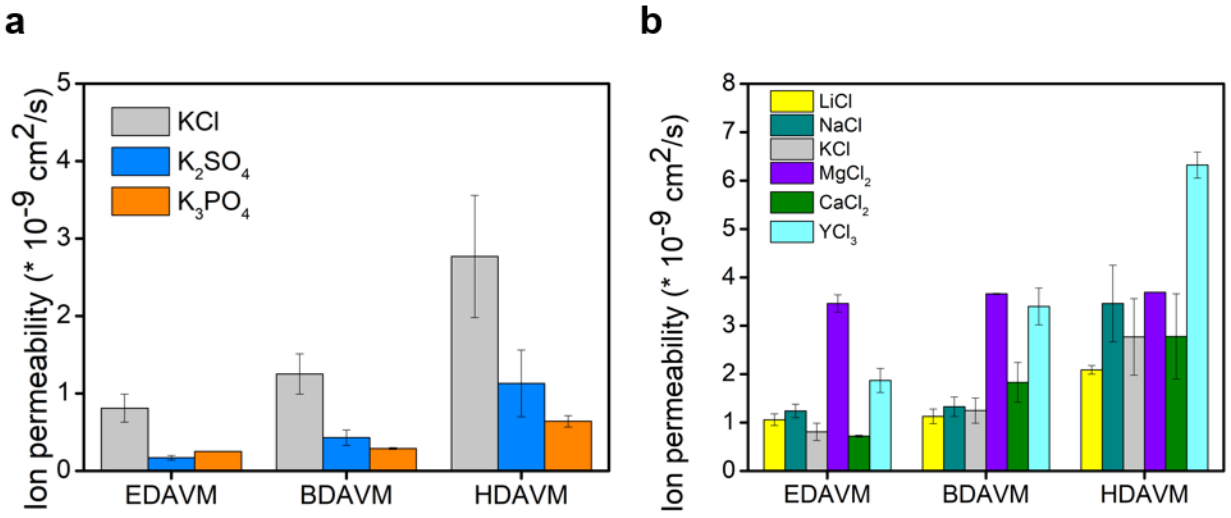

Figure 3.12: a) Tunable anion permeability through xDAVMs. b) Tunable cation permeability through xDAVMs.

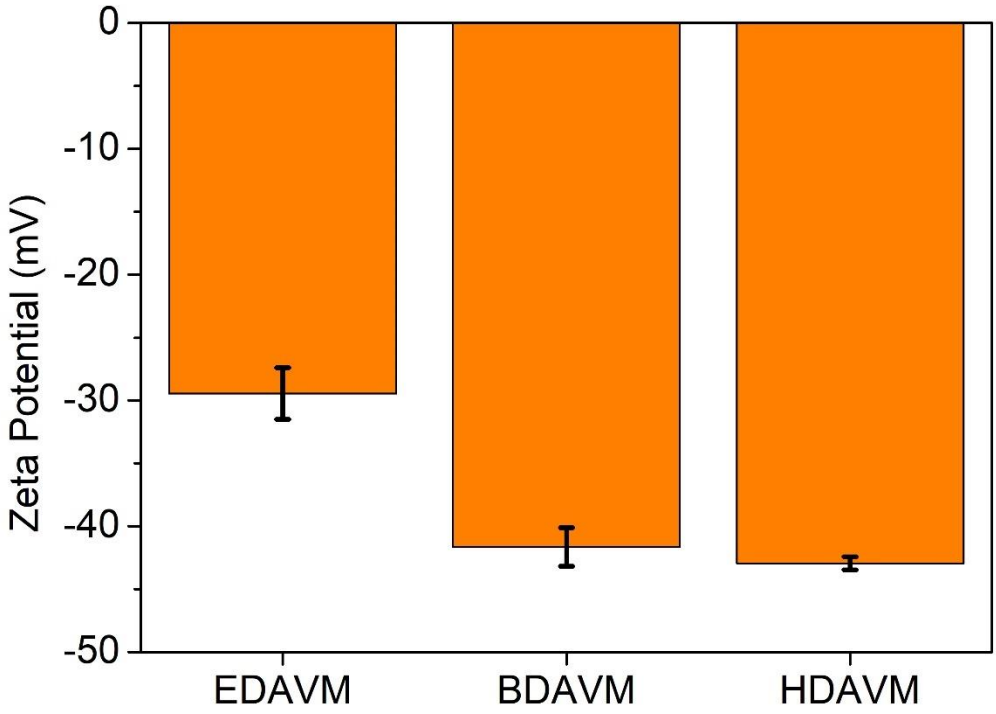

Figure 3.13: Zeta potential measurement of xDAVMs in 0.01 M KCl_{aq} at pH=5.0.

Comparisons across different cations (with respect to their size and valence), however, reveals different behavior. When the ion transport process is governed by size exclusion, the hydrated ion size is the most important factor. In this context, K^+, with the smallest hydration radius, should possess the highest ion permeability; Mg^{2+} with a larger hydrated radius would be expected to have relatively lower ion permeability. Surprisingly, as reported for (non-crosslinked) VMs[127], higher Mg^{2+} permeability was observed here for EDAVM, BDAVM, and HDAVM. A possible explanation for the high permeability could lie in a mechanism strongly dominated by the dielectric interaction with some contribution of steric and Donnan effects;

association of counter-ions with fixed charges accompanied by charge reversal for divalent cations may be responsible for the observed behavior.[135, 136] Compared to monovalent cation, Mg^{2+} is expected to pass more readily due to stronger attraction to negative membrane charges according to Donnan effect. We further investigated the ion permeability for another trivalent cation Y^{3+}. xDAVMs all exhibited higher ion permeability value compared to monovalent cations, which further prove the explanation. We note that hydrated magnesium ions are present in natural vermiculite interlayers, suggesting a potential favored interaction with this specific cation; these and other mechanisms are an interesting topic for future studies. Importantly, beyond the overall permeabilities changing, the *permeability ratios* of ions also vary as the layer spacing changes, suggesting a possible route to rational membrane design for targeted ion separations. At last, we compared the ion rejection performance of xDAVMs with different single salts through a dead-end filtration system. Because the relatively large interlayer spacing compared to the ion sizes, the ion rejection ratio is limited (shown in Figure 3.14).

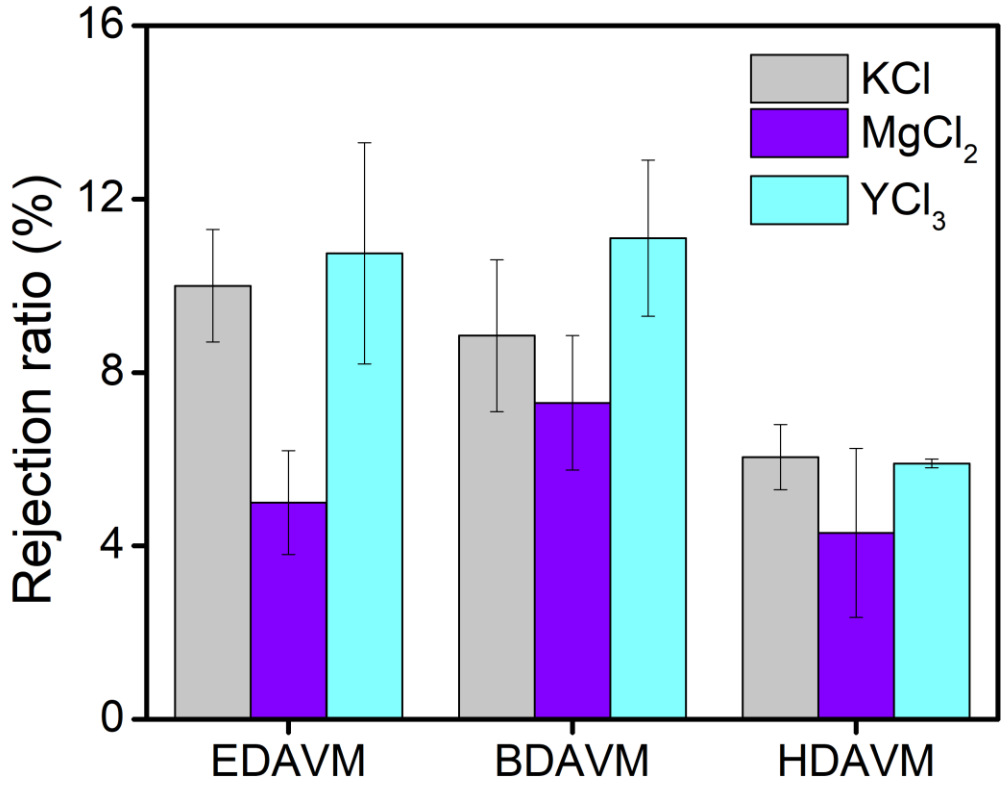

Figure 3.14: Ion rejection performance of xDAVMs with single salts

3.3 Conclusion

We have demonstrated a method for tuning the 2D interlayer galleries of phyllosilicate mineral membranes via judicious selection of different molecular crosslinkers. The water stability (including in electrolyte solutions) is enhanced while preserving the general layer morphology and structure. Control of the nanochannel height enables tuning of both water and ion permeabilities via delicate manipulation of the balance between steric hindrance and electrostatic interaction. In principle, since the ion permeability ratios vary with different

interlayer spacings, one could rationally design a particular spacing to promote transport of certain ions while inhibiting others, providing a broad array of applications for such membranes for ion separation, battery separators, wastewater treatment, resource recovery, and beyond.

3.4 Experimental Section

Vermiculite Exfoliation. Vermiculite was obtained from Sigma Aldrich, which is in bulk condition. The vermiculite was exfoliated by the ion-exchange process as reported previously. [122, 126] 100 mg of bulk vermiculites was added into 500 mL of saturated sodium chloride (NaCl) solution and stirred under refluxing at 100 °C for 24 h to replace the interlayer Mg^{2+} cations with Na^{+}. The solution was filtered, and then the sediment was rinsed repeatedly with deionized (DI) water and ethanol in sequence to remove the remaining salt. In the next step, the as-prepared sodium vermiculite (NaV) was dispersed in 500 mL 2M LiCl aqueous solution; the as-obtained mixture was kept at 100 °C under continuous magnetic stirring for 24 h to further replace the interlayer Na^{+} with Li^{+} cations and then cooled down to room temperature. After the same cleaning procedure, the lithium vermiculite (LiV) flakes were sonicated in DI water for 1 hour to exfoliate them into monolayer LiV nanosheets. Centrifugation at 3000 rpm was applied for 20 minutes to remove the multilayer vermiculite nanosheets and other bulk residues.

Fabrication of Vermiculite Membranes. The vermiculite membranes were prepared by vacuum filtration of the 50 mL diluted vermiculite nanosheet–aqueous solution mixture through a porous commercial hydrophilic PVDF membrane substrate (pore size of 0.22 μm and diameter of 47 μm). The as-prepared vermiculite film on PVDF can be peeled off from the substrate easily after dried to obtain a free-standing vermiculite membrane.

Fabrication of Crosslinked Vermiculite Membranes. To further modify the interlayer spacing to control the ion-transport properties through the membrane and enhance the water stability of vermiculite membranes, different crosslinkers were applied. To precisely control and compare the effect of the crosslinker, 1,2-ethanediamine, 1,4- butanediamine, and 1,6-hexanediamine were chosen as the crosslinkers. After the diluted vermiculite nanosheet solution was obtained following the vermiculite exfoliation process, 50 mg of crosslinker was dropped into the 50 mL solution and followed by a sonication process for 1 hour. The crosslinked vermiculite nanosheet solution were filtered through a PVDF substrate and peeled off to obtain free-standing EDAVM, BDAVM, and HDAVM.

Structural and Chemical Characterization. The surface structures and morphologies of vermiculite powder and different VMs were characterized using a Carl Zeiss Merlin high-resolution field emission scanning electron microscope (FE-SEM) at 3.0 kV. The X-ray diffraction (XRD) patterns in the Bragg-Brentano geometry were obtained using a Rigaku benchtop X-ray diffractometer equipped with HyPix-400 MF 2D hybrid pixel array detector (HPAD) and a Cu Kα X-ray source (wavelength of 1.5418 Å) operating at 40 kV and 15 mA. X-ray photoelectron spectroscopy (XPS) measurements were carried out on a Thermo Fisher k-Alpha+, and the spectra were analyzed using Thermo Fisher Avantage software. The X-ray source was a micro-focused monochromatic Al Kα (1487 eV) with a spot size of 400 μm. Survey scans used a pass energy of 200.0 eV and a step size of 1.000 eV, and high-resolution XPS scans used a pass energy of 50.0 eV and a step size of 0.100 eV. Ar^+ ion sputtering was performed for depth profile measurement and the sputter rate was calibrated using Ta_2O_5, accounting for a Ta_2O_5-equivalent rate of 0.28 nm/s (time of etch cycle: 10s; ion energy: 1000 eV). Thermo Avantage (v. 5.977, Build 06436) post-processing software was used for spectral analysis. High

resolution peak deconvolution was performed using the Powell peak fitting algorithm with mixed Gaussian-Lorentzian line shapes and a Smart background. All the spectra were referenced to the C1s peak at 284.8 eV. Surface wettability was investigated using a static water contact angle measurements system (DSA 25E, KRÜSS) and the sessile drop method. The morphologies of VMs were characterized using an MFP-3D atomic force microscopy (Asylum Research). The clay mineral flakes deposited on a silicon wafer were imaged with Nanosensors PPP-NCHR-W tips (Resonance frequency: 204–497 kHz; Force constant: 10–130 N/m; and nominal tip radius: 10 nm) in a tapping mode. The collected images were analyzed using the Asylum Research software to determine the thickness and size of the individual particles.

Water Permeance Measurement. The water permeance performance of the as-prepared VMs was tested with a lab-scale dead-end filtration system with an effective membrane area of 4.9 cm^2. The flux test experiments were operated under 2.2 bar at 25 °C. The water flux (F_w, L m^{-2} h^{-1} bar^{-1}) was calculated by the following equation.

$$F_w = \frac{Q}{At\Delta P}$$

where Q, A, t, and ΔP represent the volume of permeated water, effective membrane area, permeation time, and driving pressure on the feed side, respectively.

Zeta Potential Measurement. VM zeta potentials were measured using streaming potential measurements performed with an adjustable gap cell in an Anton Paar SurPASS 3 system, averaging over at least three samples of each material. The electrolyte for all the measurements is 0.01 M KCl aqueous solution. The reference material is a polyvinylidene fluoride (PVDF) membrane provided by Anton Paar. The zeta potential can be calculated based on the Smoluchowski equation. [137, 138]

$$\zeta = \frac{dU}{dp}\frac{\eta}{\varepsilon\varepsilon_0}\kappa$$

Ion Transport Measurement. The ion-transport properties were tested with an H-cell permeability device. The free-standing crosslinked VMs were immersed in DI water before testing to remove impurity particles and ions on the surface. The feed half-cell contains 90 mL 0.1 M of different salt solutions (KCl, NaCl, LiCl, $MgCl_2$, $CaCl_2$, YCl_3, K_2SO_4, or K_3PO_4), and the permeate half-cell was filled with the same volume DI water. Both sides of the H-cell were stirred under 400 rpm to avoid the potential influence of concentration polarization. The ionic conductivity of permeate solution was continuously recorded using an ionic conductivity meter (Orion Versa Star Pro Conductivity Benchtop Meters) and then permeation rates were obtained based on the linear relationship between the conductivity and concentration of salt solutions. Two to four different samples are tested for each xDAVM. The reliability of the conductivity method was further confirmed with Thermo Scientific iCAP PRO XP ICP-OES measurement. The samples for the ICP-OES tests were collected and diluted 100 times in 1.0 wt% HNO_3 solution.

In the concentration-driven diffusion and crossover tests, the increase of concentration in the permeate solution over the initial period without any volume change follows Fick's first law.[139] The ions permeation rate (J) across a membrane is calculated from the following equation.

$$J = \frac{V}{A}\left(\frac{\partial C}{\partial t}\right)$$

where J, V, A, C, and t are the flux, solution volume, effective area of the membranes, concentration of permeate, and diffusion time, respectively.

During the process with a constant flux, the previous equation can be simplified as follows:

$$J = D\left(\frac{C_1 - C_2}{l}\right) = P(C_1 - C_2)$$

where D is the permeability, C_1 and C_2 are the concentration of feed and permeate solutions, l is the membrane thickness, and P is the permeance. The membrane thickness is measured by a micrometer with the accuracy of 1 μm.

Appendix A

Figure 3.15: H-cell systems for ion diffusion tests.

Chapter 4: SURFACE ZETA POTENTIAL OF ALD-GROWN METAL OXIDE FILMS

Membranes are among the most promising technologies for energy-efficient and highly selective separations, and the surface charge property of membranes plays a critical role in their broad applications. Atomic layer deposition (ALD) can deposit materials uniformly and with high precision and controllability on arbitrarily complex and large substrates, which renders it a promising method to tune the electrostatics of water/solid interfaces. However, a systematic study of surface charge properties of ALD grown films in aqueous environments is still lacking. In this work, 17 ALD-grown metal oxide films are synthesized, and a comprehensive study of their water stability, wetting properties, and surface charge properties are provided. This work represents a resource guide for researchers, and ultimately for materials and process engineers, seeking to tailor interfacial charge properties of membranes and other porous water treatment components.

4.1 Introduction

The global interplay of supply and demand for water is largely dictated by the growth of the world population, ongoing societal development, and climate change. The fraction of the world's population experiencing water scarcity increased from 0.24 billion in the 1900s to 3.8 billion people in 2009 and is forecast to reach 6.3 billion in the next few decades.[140, 141] At the same time, society is undergoing significant expansion of manufacturing, energy production, and

other water-intensive activities. Thus, demand for fresh water is growing dramatically. Beyond water scarcity, extensive pollution of water is an emerging global issue that needs to be addressed to maintain a sustainable environment. [141, 142] Current methods to address water pollution are often energy-intensive. As with water, energy supplies are increasingly strained with our expanding population, so utilization of existing methods for mitigating clean water shortages at the expense of greater energy consumption is unsustainable. New materials-based strategies are of increasing interest in the development of efficient approaches to water treatment.

The interaction between water and solid interfaces represents an essential topic of profound interest from both fundamental and applied science and engineering perspectives of almost all water treatment components, including sorbents, membranes, catalysts, electrodes, and beyond.[31] Intimately understanding and then tailoring interfacial structure and chemistry is a foundational basis for controlling the performance of these components. Membranes, in particular, offer enticing prospects for energy-efficient and highly selective separations to help address the treatment of progressively challenging source waters.[2]

The surface-charge property of a membrane is a critical parameter for a broad range of functions, such as fouling mitigation[143], ion separation[144], salinity-based energy conversion[52, 145], and adsorption[146]. In the context of biofouling, the membrane surface charge can be controlled to induce electrostatic repulsion and hinder the adhesion of biomolecules/biomacromolecules on the membrane surface.[143] Electrostatics are also central to many separations processes. Xu's group attached ionizable functional groups on graphene oxide (GO) membranes to change the surface charge, and the charged membrane surface provided interactions with ions to deliver high salt rejection and water permeance.[144] Membranes with asymmetric charge properties across the membrane thickness, which are called Janus membranes, provide an inner driving force at the

junction barrier with the potential to affect the ion-transport process inside pores. This uniform structure offered an additional potential, which could boost selective ion transport when aligning with the external driving force.[52,145] Reversed electrodialysis (RED) based on this membrane can directly convert osmotic energy into electricity. Moreover, charged membranes can sequester metal ions, whether to address toxicity or capture critical resources for recycling.[146]

Because the actual surface potential is challenging to characterize experimentally, the zeta potential, or ζ-potential, is widely used for quantifying the magnitude of the surface charge. Zeta potential is the electrical potential at the electrokinetic slipping plane at the material surface (Figure 4.1). A positive zeta potential means that this material surface has a net positive surface charge in this condition, and conversely a negative zeta potential represents a negative surface charge. The value of this parameter depends on the nature of ions in the solution and also the properties of the solid surface itself.[147] Material surfaces with a zeta potential between -10 and +10 mV are considered approximately neutral, while surfaces with a zeta potential greater than +30 mV or less than -30 mV are considered strongly cationic and anionic, respectively.[148]

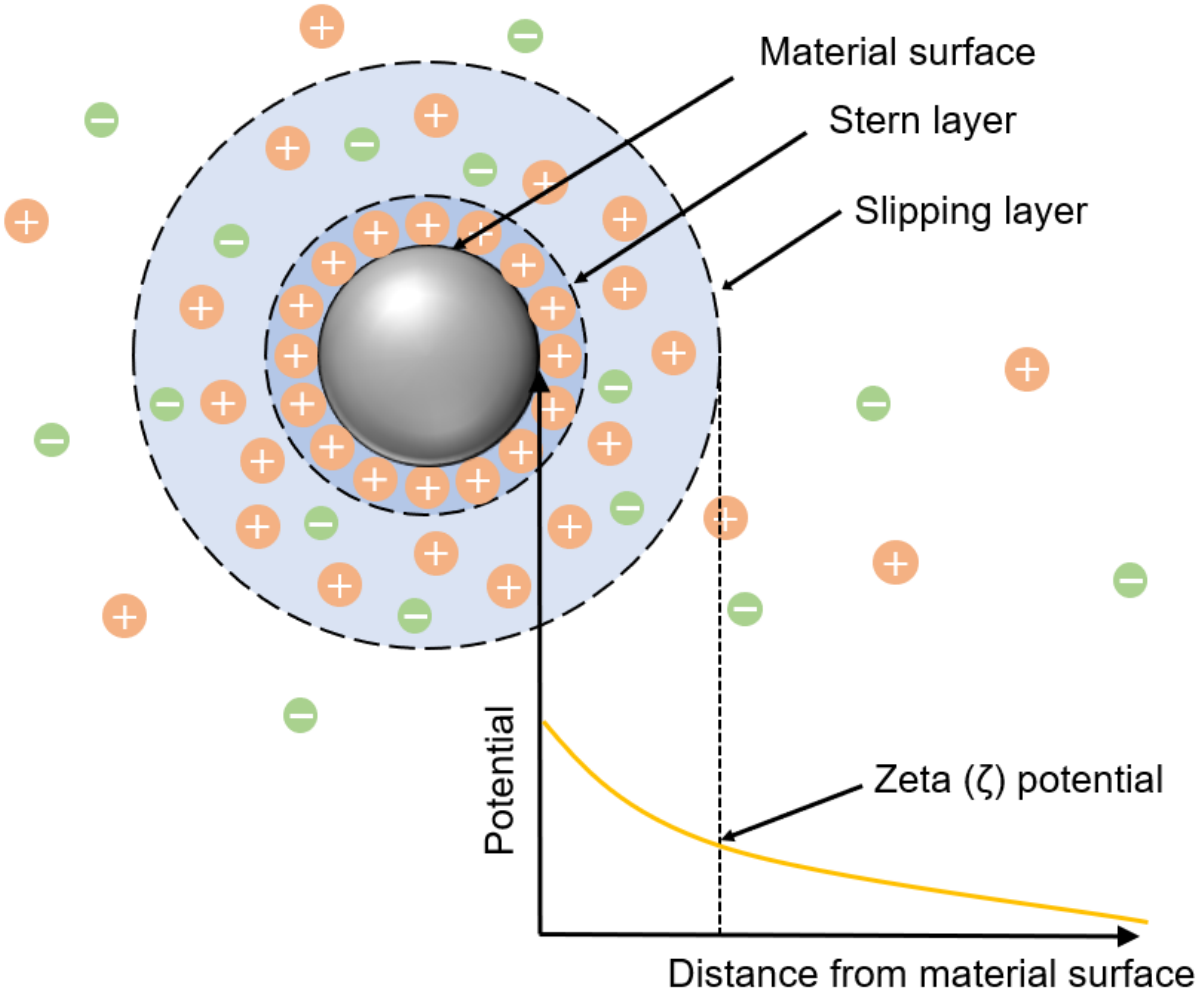

Figure 4.1: Diagram of zeta potential surrounding a material in an aqueous electrolyte.

Since the zeta potential is a property of the solid material in contact with a liquid, control of the potential can be achieved by depositing thin layers of various dielectric materials. A variety of deposition techniques have been developed to create a thin film on a substrate.[149] Most deposition techniques can categorized as either solution-phase, like dip coating or spin coating, and vapor-phase, such as thermal evaporation or sputtering. These deposition methods are simple and cost-effective, but they often suffer from poor thickness control, uneven coverage, and

inability to coat porous substrates, limiting application in membrane functionalization. Compared with these techniques, atomic layer deposition (ALD) can deposit materials uniformly and with high precision and controllability on arbitrarily complex and large substrates, which is especially important for porous substrates like membranes.[150, 151] Moreover, there is a large library of materials that can be grown via ALD, offering a broad range of potential surface properties.[65, 152] Thus, ALD is a promising method to tune the electrostatics of water/solid interfaces. For ALD to successfully modify a polymeric membrane, there must be a binding interaction between the vapor-phase precursor and a functional group on the polymer. Many commercial membranes have such functional groups natively, such as carbonyls and sulfones. For polymers lacking such ALD-reactive moieties, the membrane can be sensitized before ALD processing using either plasma[153] or dip-coating[154].

Zeta potential is difficult to predict a priori, so experimental measurements are an essential tool in guiding the selection of materials for targeted applications. Furthermore, the zeta potential depends not only on the composition of the material at the interface but also on its atomic-scale structure (e.g., crystallinity) and mesoscale morphology. There are several studies in the literature reporting zeta potentials for different metal oxides, but the vast majority of these measurements were performed on particulate materials, and such particles are often stabilized by grafted molecules that can significantly influence the electrostatic environment.[155, 156, 157, 158] Results for ALD films, even for identical stoichiometries, are likely to vary from these particle studies because of the different surface-charge densities caused by atomic ordering as well as electrolyte selection. A few groups have reported zeta potential properties for ALD films[159], but many technologically and scientifically interesting ALD materials have yet to be characterized by zeta potential measurements. Here, we provide a systematic analysis of zeta potentials for a

diverse library of ALD film materials. We synthesize over 15 metal oxide films and investigate their stability, wettability, and surface-charge properties, which will serve as a reference for a range of future studies on water treatment through manipulating the surface charge properties with ALD.

4.2 Results and Discussion

4.2.1 Films Grown Using ALD

XPS analysis was carried out to characterize the composition and oxidation states of as-prepared samples. These results in Figure 4.2-4.19 demonstrate the successful growth of each of the oxide films through ALD. Transition metals can typically assume multiple oxidations states. The XPS spectra in Figure 4.17-4.19 show multiple oxidation states for the ALD metal oxides of Co, V, and Mn. These different oxidation states are formed during the ALD or upon exposure to the air. In the oxygen 1s spectra of all oxides, in addition to oxides, there are also hydroxide features due to the surface bound hydroxides and adsorbed water.[160] The XPS spectra of Y_2O_3, MgO, and NiO revealed the presence of carbonates. For instance, in Figure 4.12, the Ni 2p spectrum shows the NiO film to be a composite of NiO, $Ni(OH)_2$, and $NiCO_3$ and the Mg 1s peaks MgO film show $Mg(OH)_2$ and $MgCO_3$ features (Figure 4.16) exhibiting their reactive nature with water and CO_2 in the air. Note that very small or no Si 2p features are observed for any of the films, indicating the films are continuous with no pinholes. The results of XPS surface scans of films, Table 4.1, also revealed the high content of carbon, primarily due to the adventitious carbon and contamination during the ALD reaction of carbon-based precursors. In a common XPS measurement, Ar^+ sputtering is used to clean the adventitious carbon. However,

here we avoided Ar^+ sputtering because it can reduce the metal ions that result in the inaccurate composition of oxidation states. To confirm that there is minimal carbon within the films other than adventitious carbon, we also performed surface etching. C1s spectra were obtained after 10 s of Ar^+ sputter etching using 2000 eV energy at medium current. The elemental carbon content and spectra from before and after surface etching are summarized in Table 4.2. As can be seen from Table 4.2, most of the carbon disappeared after surface cleaning. However, there is a small amount of carbon left after cleaning for many of the films. This carbon originates from residuals of the ALD precursors.

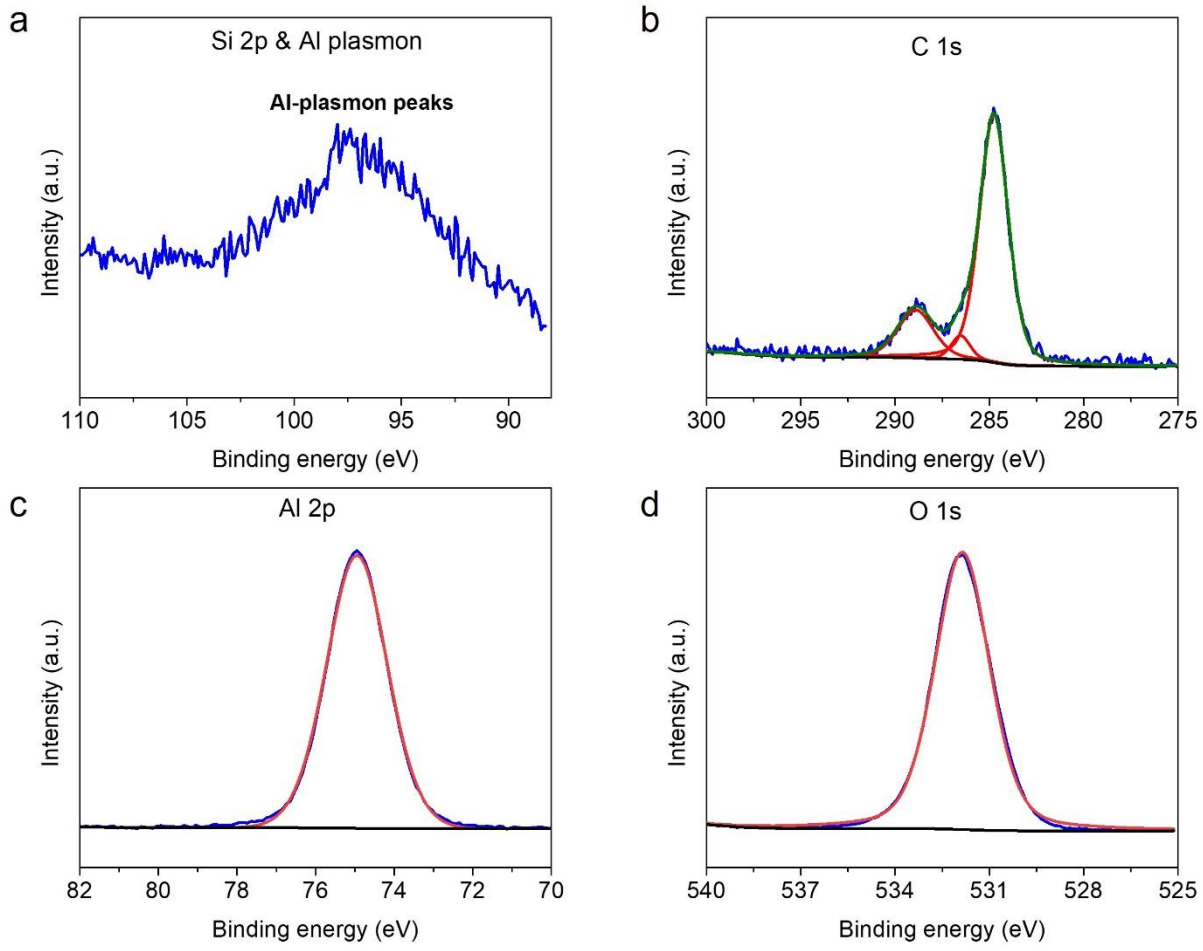

Figure 4.2: XPS spectra of Si 2p, C 1s, Al 2p and O1s signals of Al_2O_3

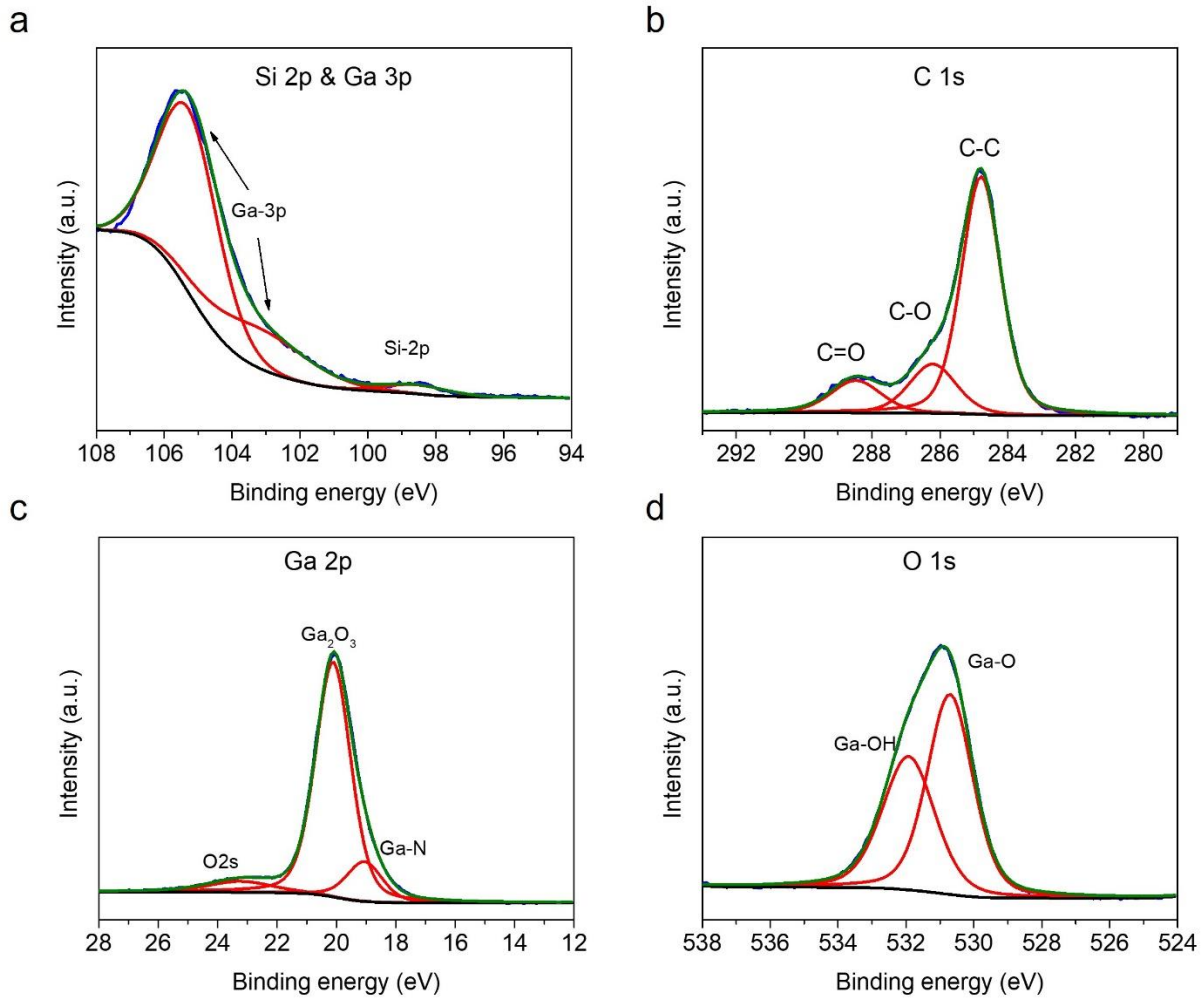

Figure 4.3: XPS spectra of Si 2p, C 1s, Ga 2p, and O 1s signals of Ga_2O_3

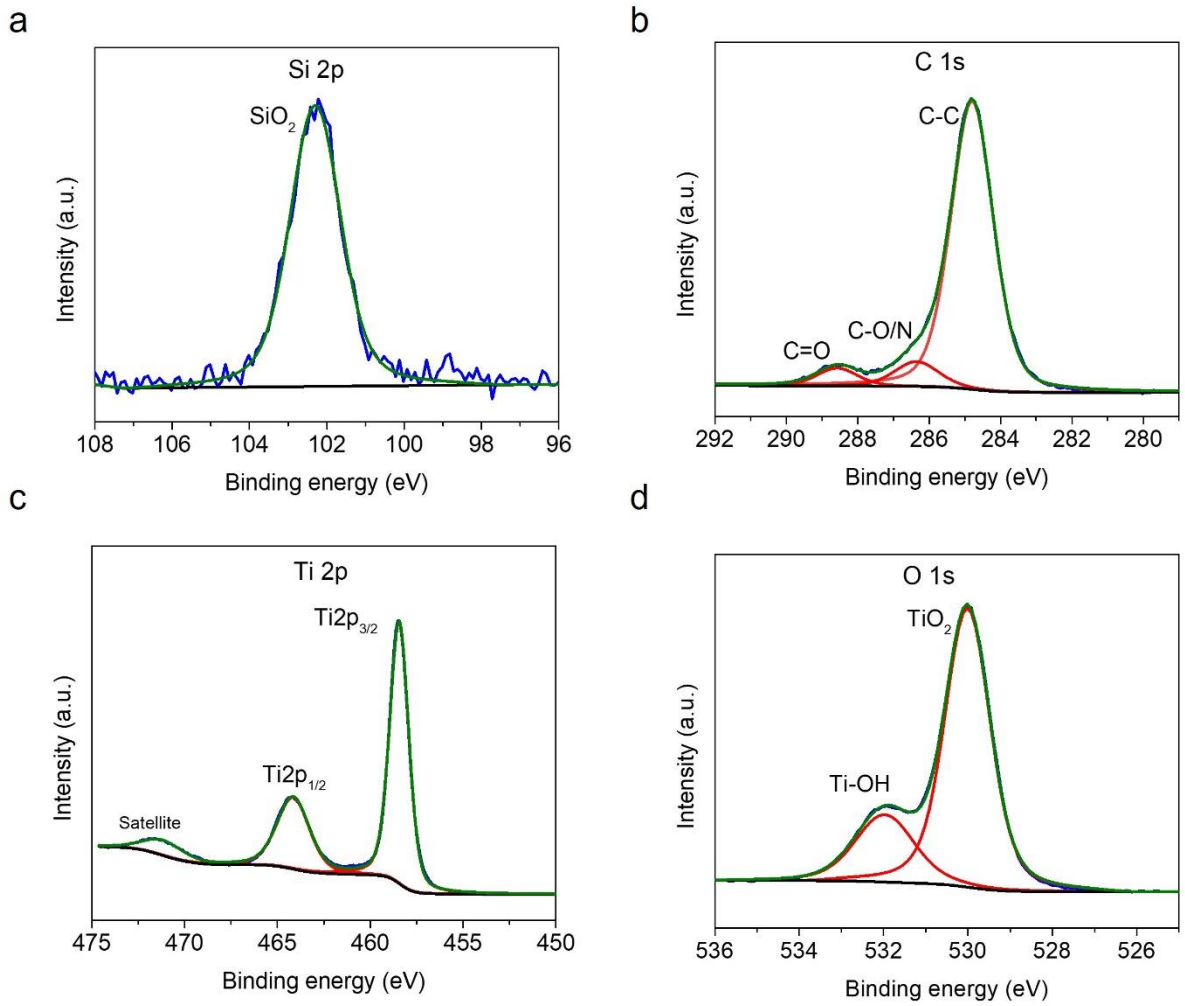

Figure 4.4: XPS spectra of Si 2p, C 1s, Ti 2p, and O 1s signals of TiO_2

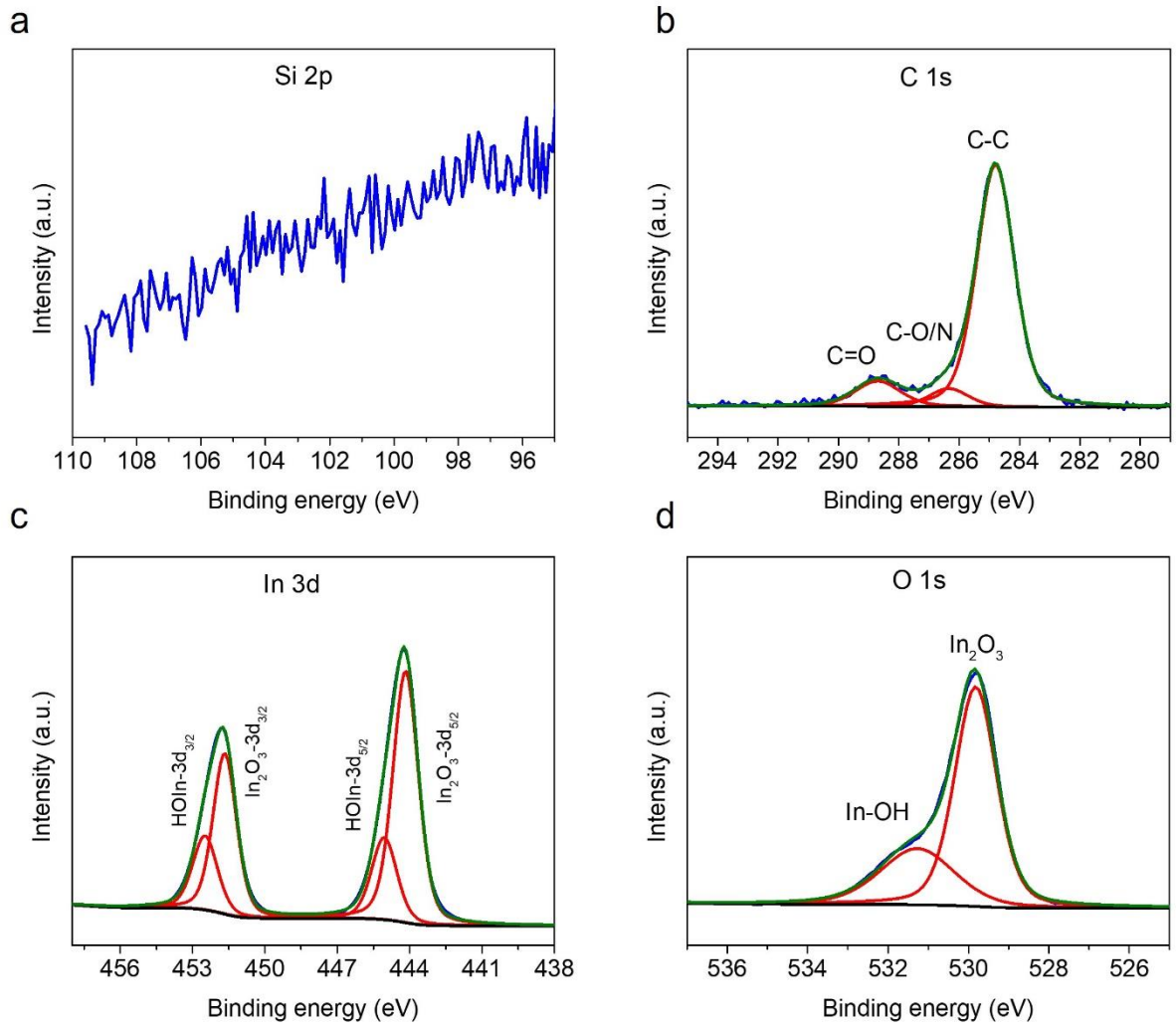

Figure 4.5: XPS spectra of Si 2p, C 1s, In 3d, and O 1s signals of In_2O_3

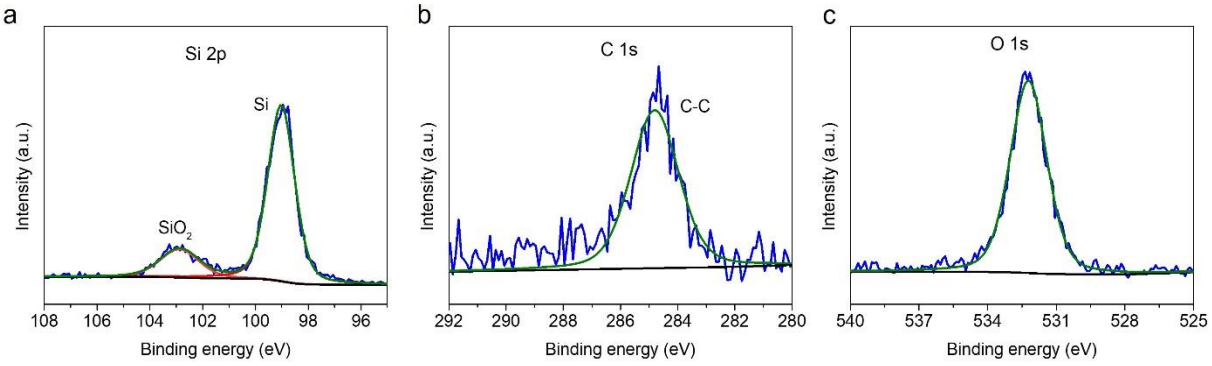

Figure 4.6: XPS spectra of Si 2p, C 1s, and O 1s signals of Native SiO_2

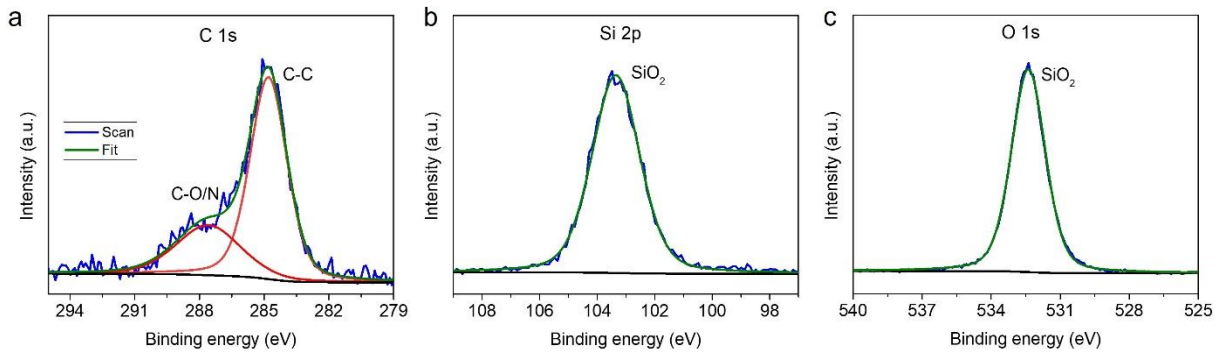

Figure 4.7: XPS spectra of Si 2p, C 1s, and O 1s signals of SiO_2

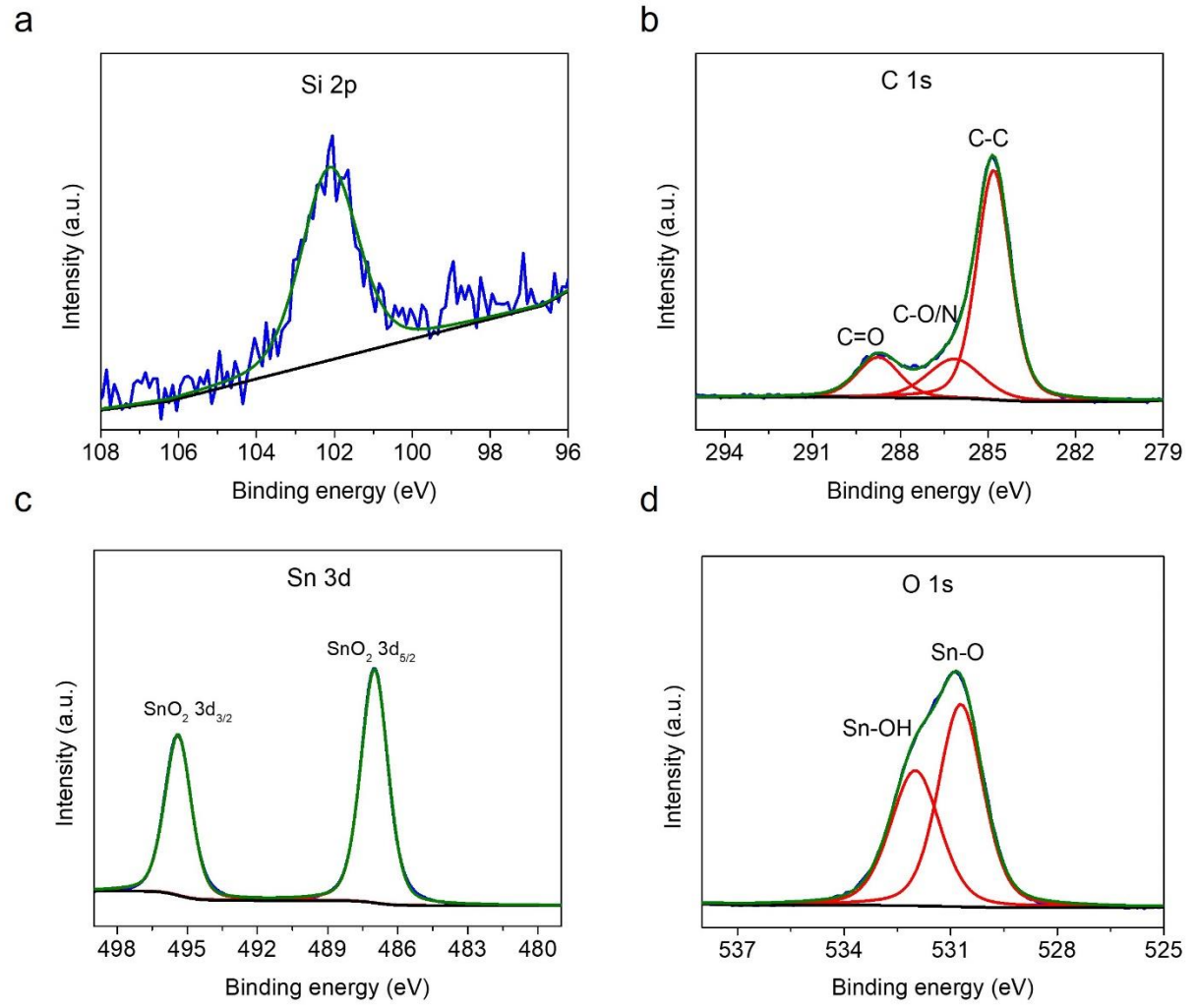

Figure 4.8: XPS spectra of Si 2p, C 1s, Sn 3d, and O 1s signals of SnO_2

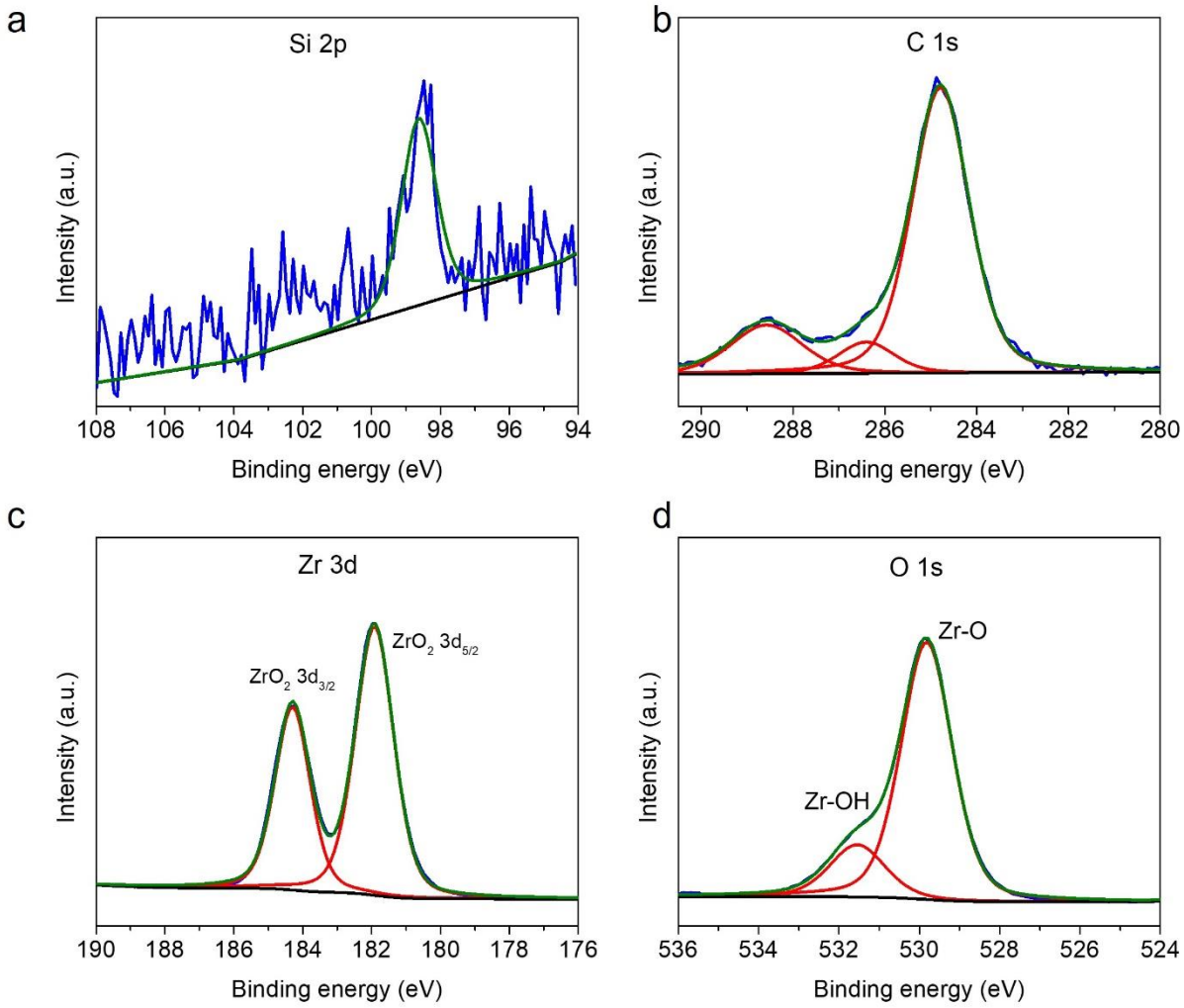

Figure 4.9: XPS spectra of Si 2p, C 1s, Zr 3d, and O 1s signals of ZrO_2

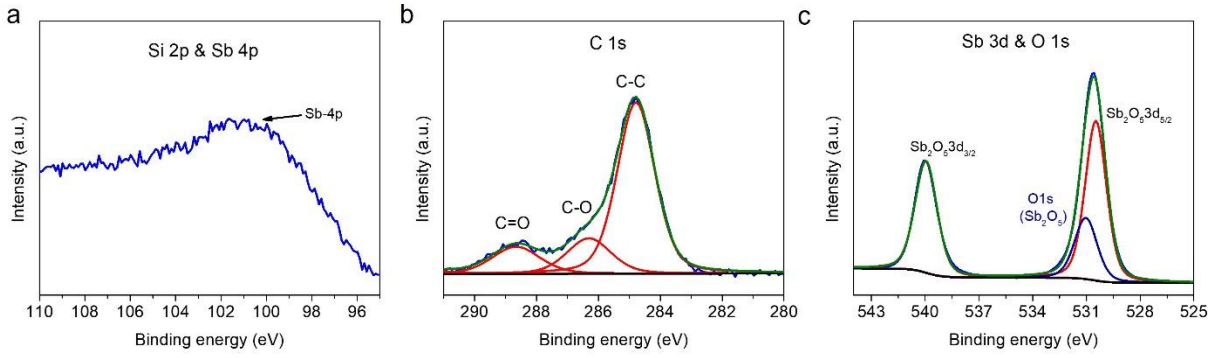

Figure 4.10: XPS spectra of Si 2p, C 1s, Sb 3d, and O 1s signals of Sb_2O_5

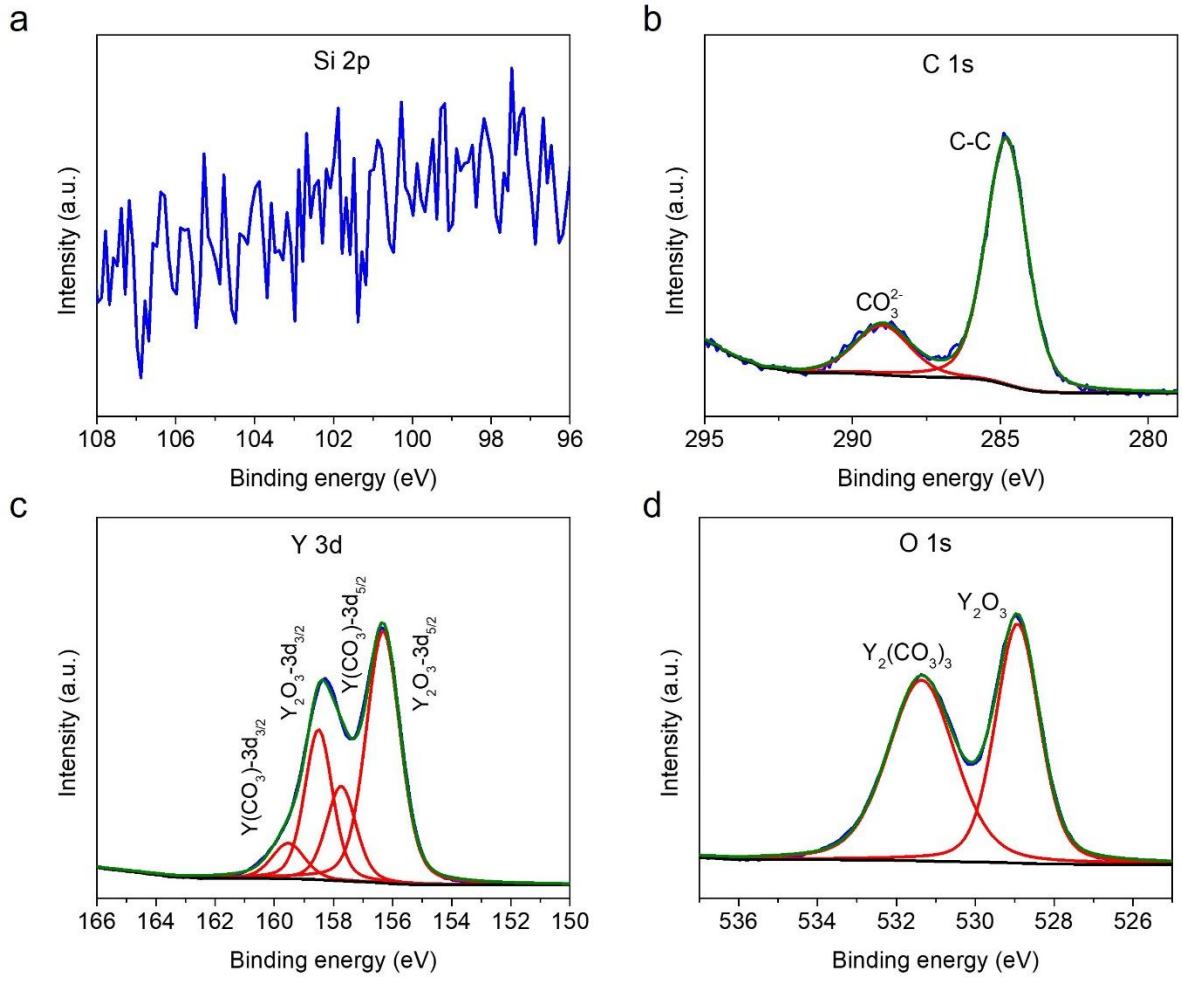

Figure 4.11: XPS spectra of Si 2p, C 1s, Y 3d, and O 1s signals of Y_2O_3

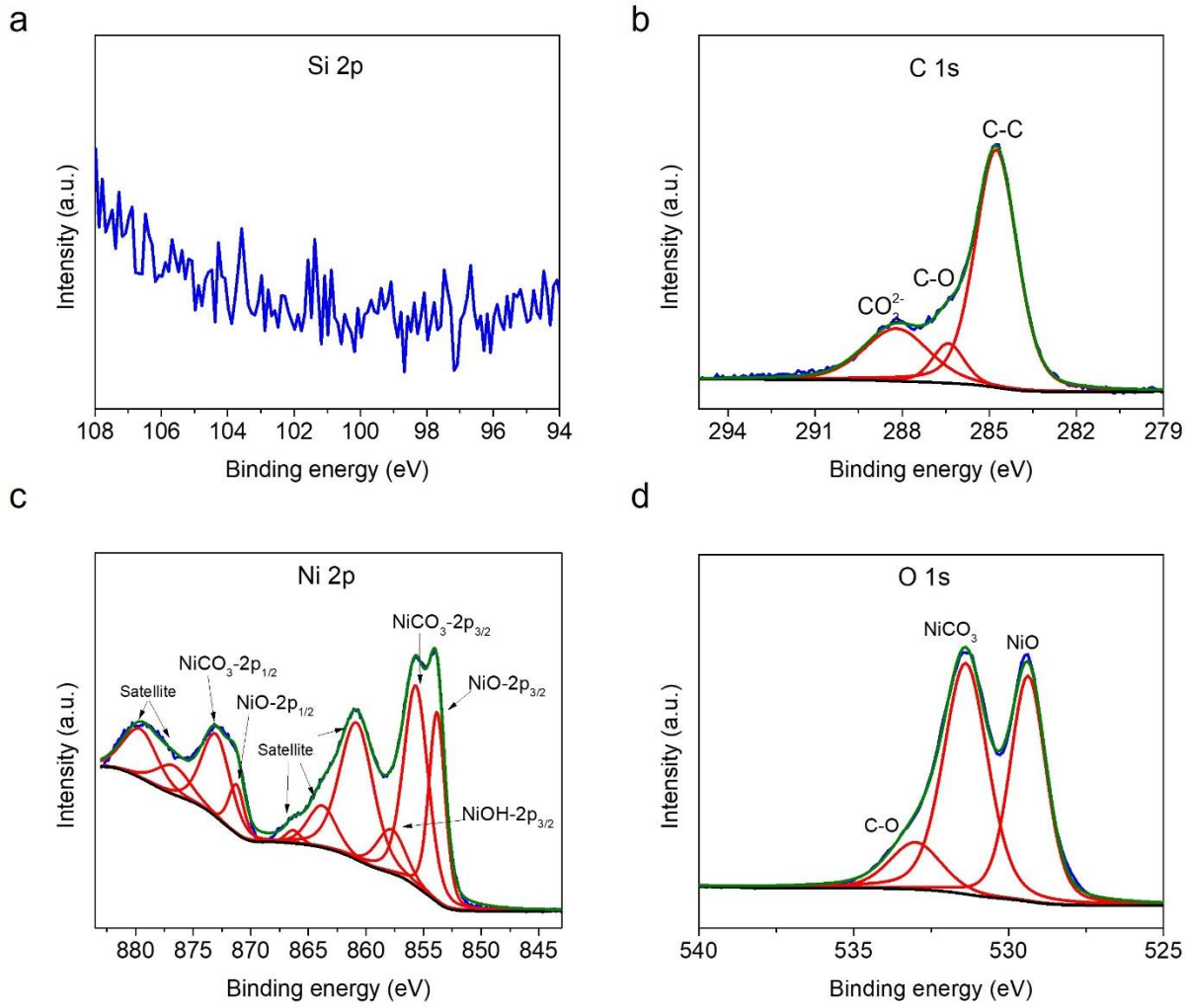

Figure 4.12: XPS spectra of Si 2p, C 1s, Ni 2p, and O 1s signals of NiO

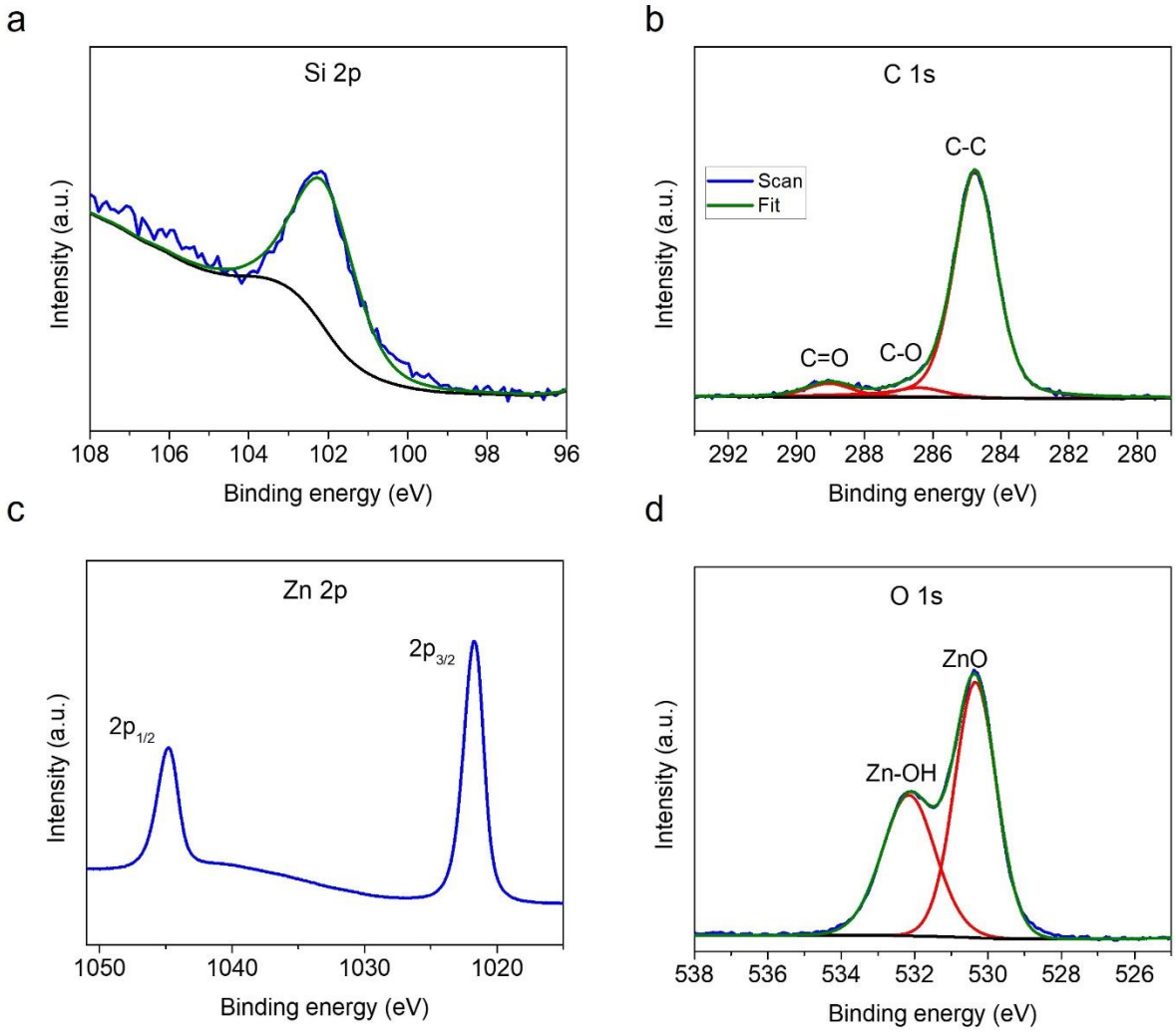

Figure 4.13: XPS spectra of Si 2p, C 1s, Zn 2p, and O 1s signals of ZnO

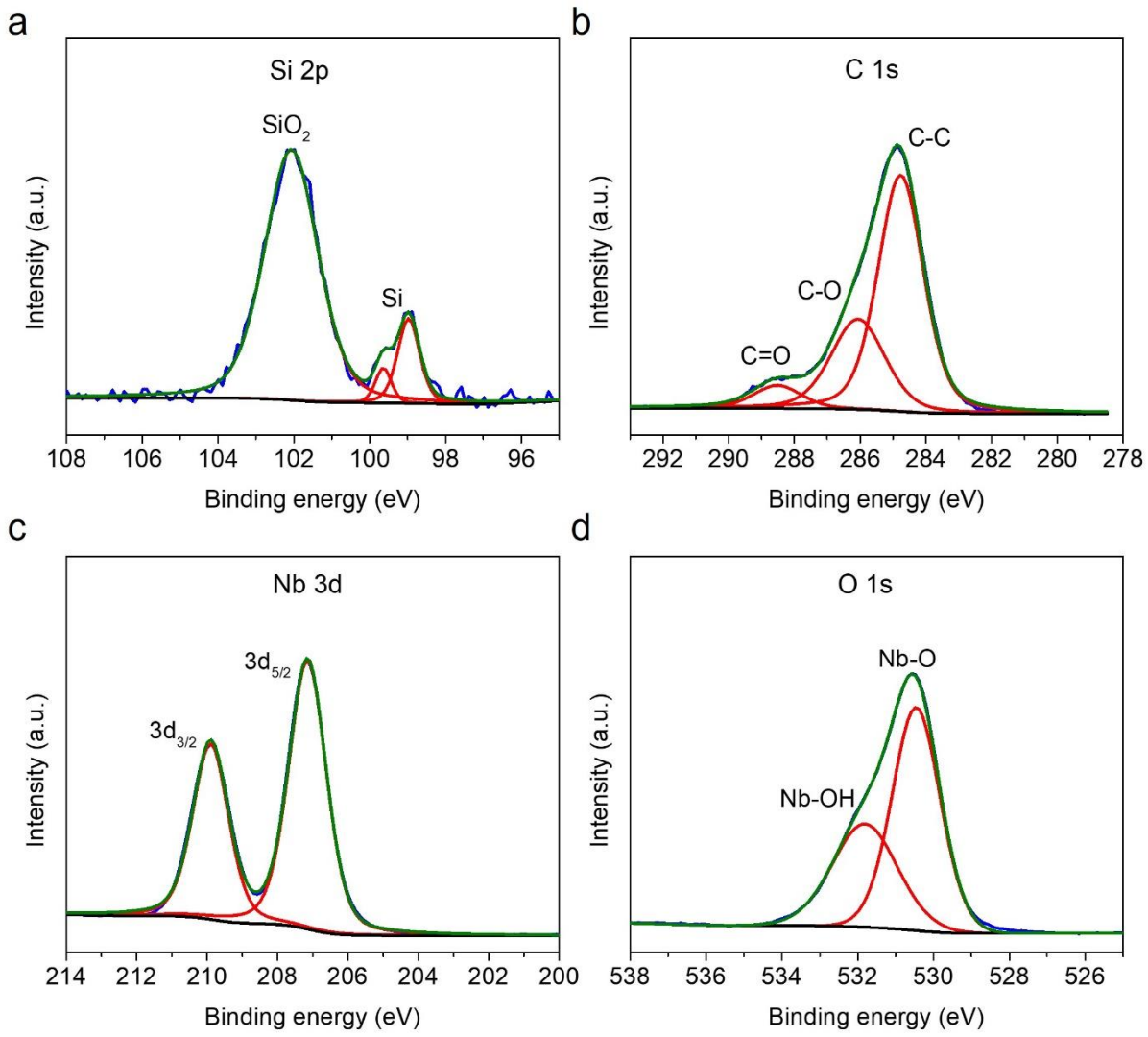

Figure 4.14: XPS spectra of Si 2p, C 1s, Nb 3d, and O 1s signals of Nb_2O_5

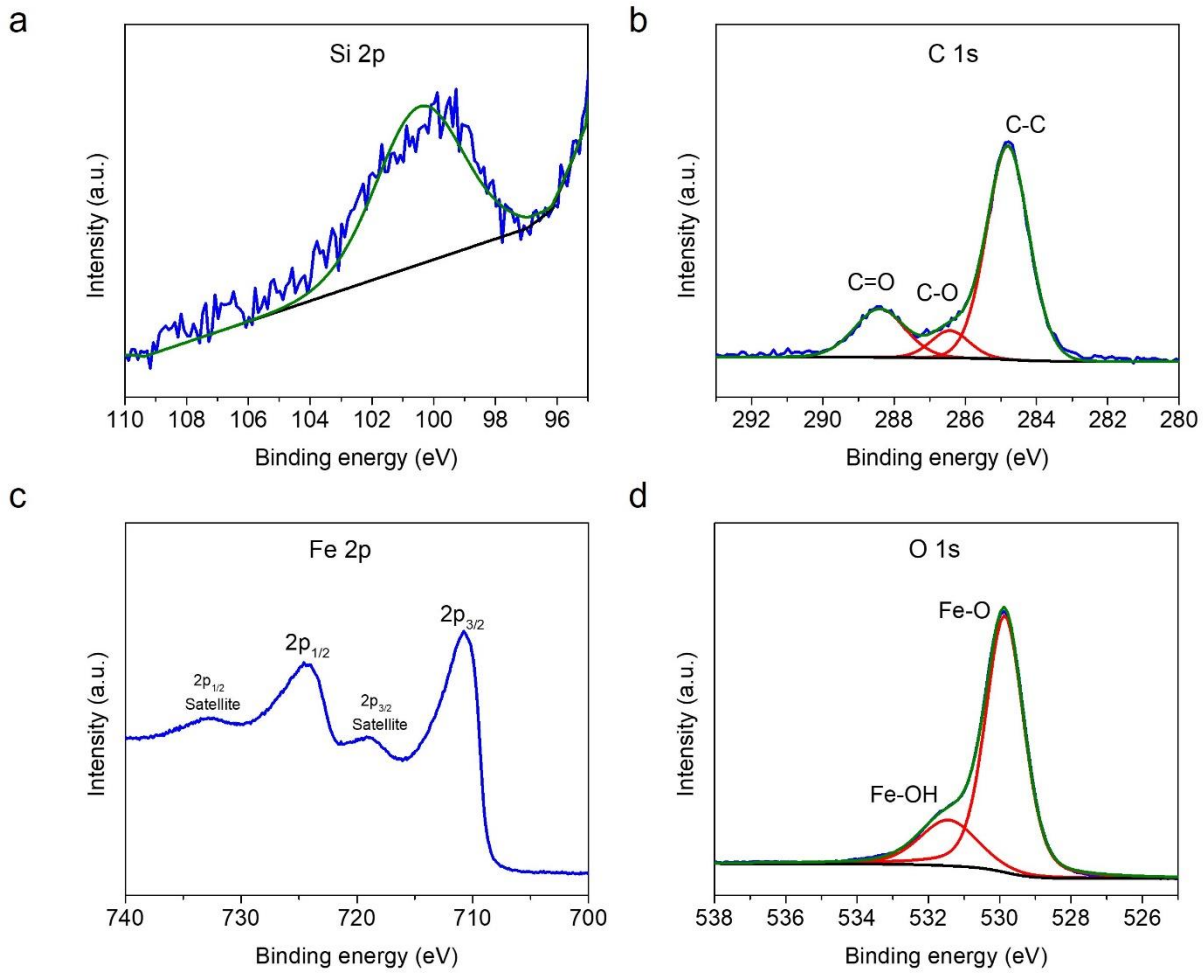

Figure 4.15: XPS spectra of Si 2p, C 1s, Fe 2p, and O 1s signals of Fe_2O_3

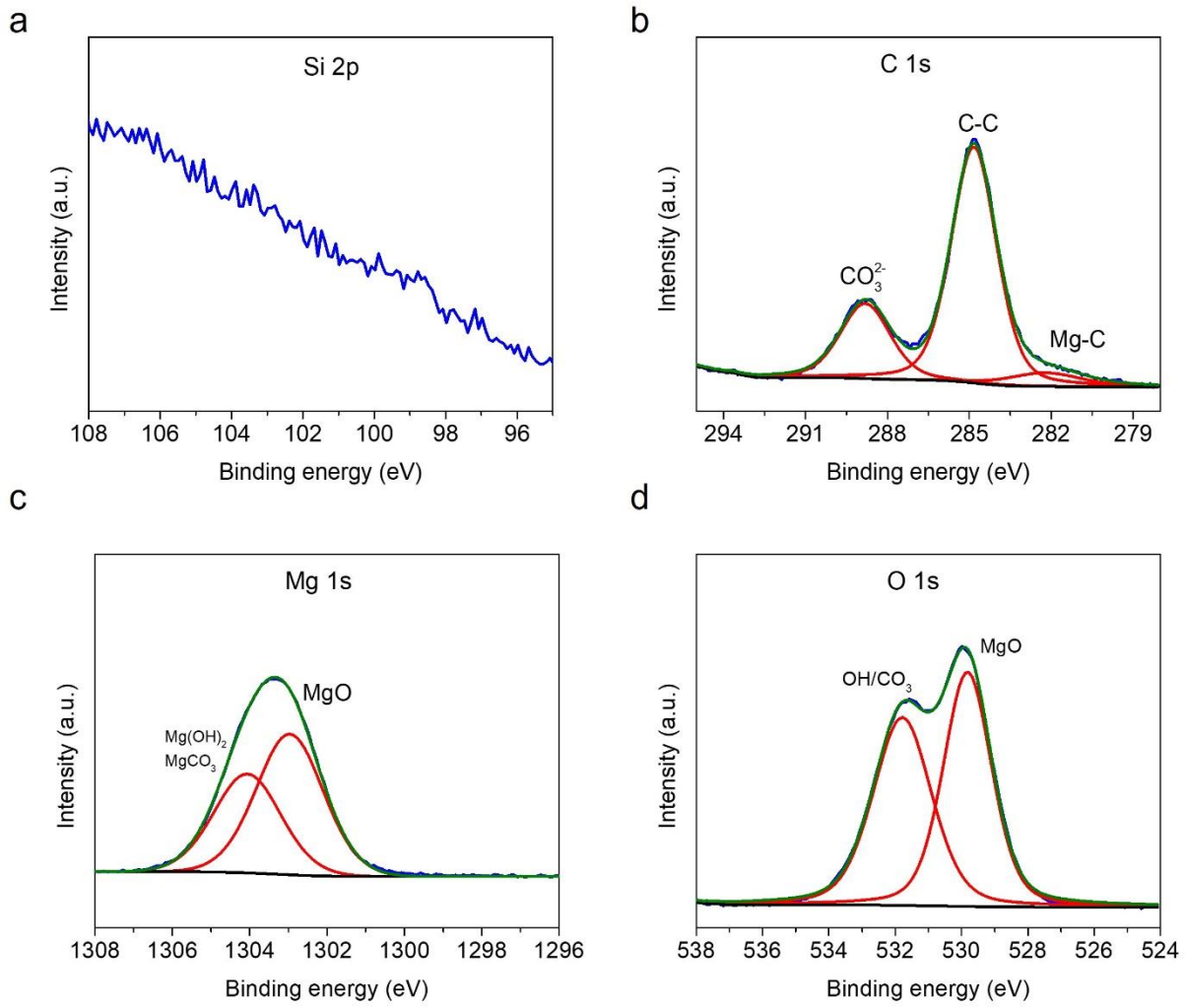

Figure 4.16: XPS spectra of Si 2p, C 1s, Mg 1s, and O 1s signals of MgO

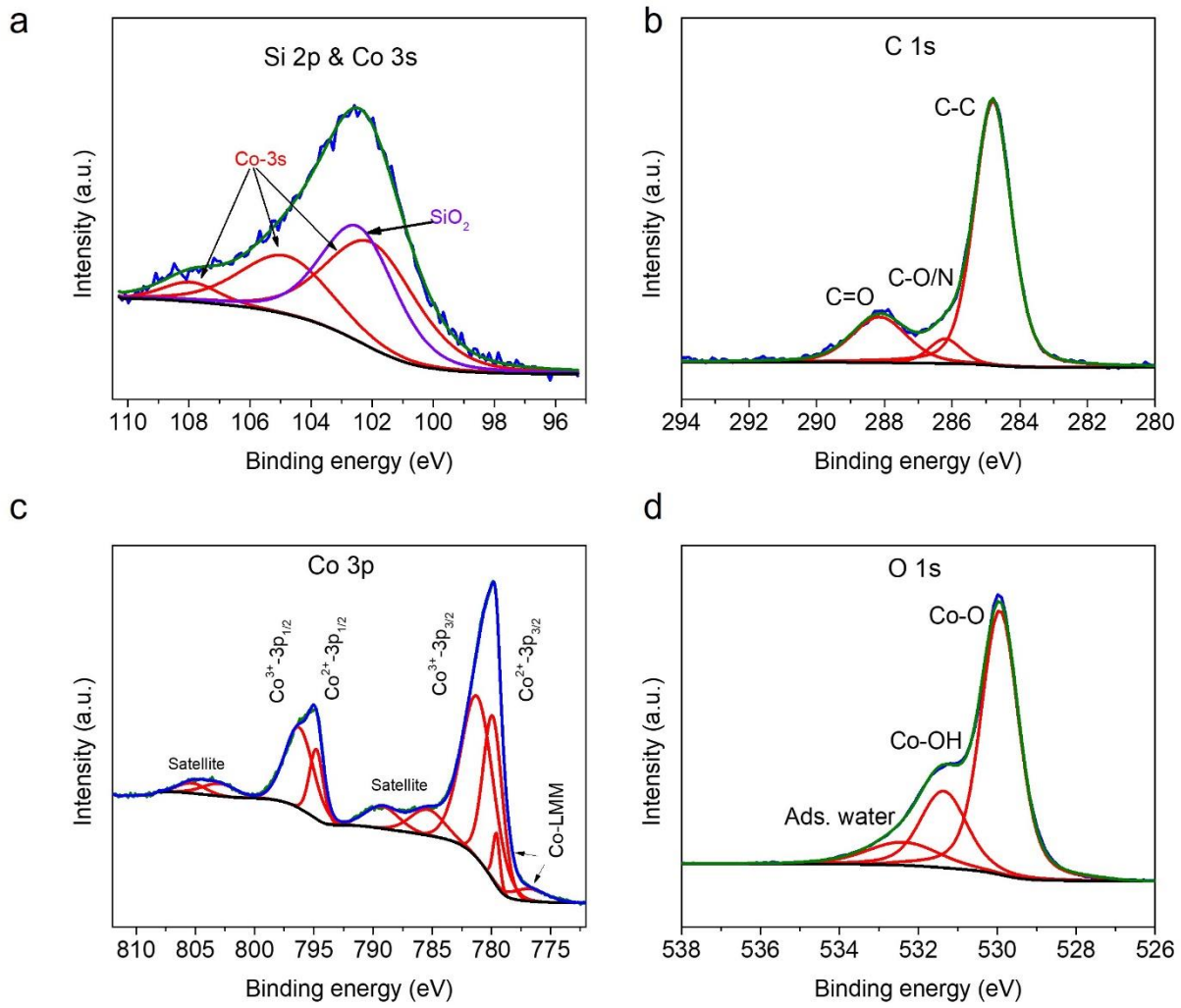

Figure 4.17: XPS spectra of Si 2p, C 1s, Co 3p, and O 1s signals of CoO_x

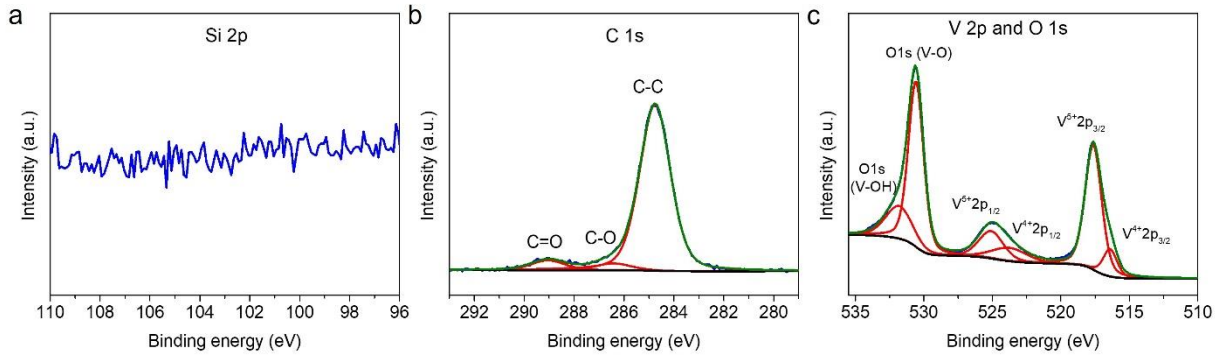

Figure 4.18: XPS spectra of Si 2p, C 1s, V 2p, and O 1s signals of V_2O_5

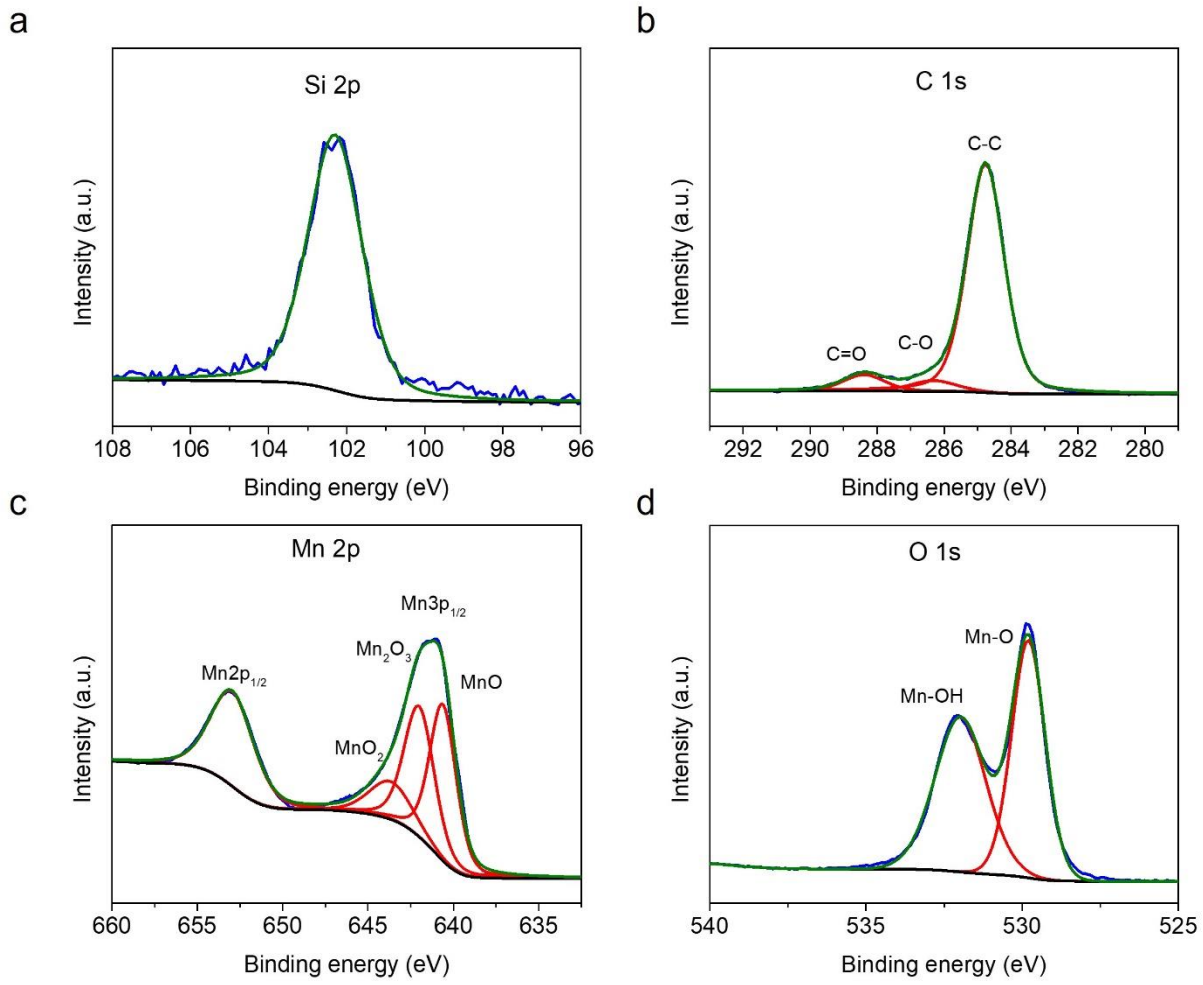

Figure 4.19: XPS spectra of Si 2p, C 1s, Mn 2p, and O 1s signals of MnO_x

Table 4.1: XPS elemental composition of ALD films

Oxides	Metal at. %	O at. %	C at. %	Si at. %	Other at. %
Native SiO_2	10.57 % (Si^{4+})	35.75	9.2	44.49 (Si^0)	-
Al_2O_3	34.84 (Al)	58.19	6.98	0	-
CoO	23.23 (Co)	44.09	21.38	6.8	0 (N)
MnO_x	12.41 (Mn)	40.49	39.4	7.4	0.27 (N)
SiO_2	28.19 (Si)	42.55	26.24	-	3.01 (N)
TiO_2	19.75 (Ti)	44.85	31.17	3.72	0.51 (Cl)
In_2O_3	27.72 (In)	51.21	21.09	0	-
Y_2O_3	26.09 (Y)	50.33	23.57	0	-
V_2O_5	16.86 (V)	50.24	32.89	0	-
SnO_2	15.89 (Sn)	50.44	28.19	2.02	3.46 (N)
Sb_2O_5	22.92 (Sb)	62.14	13.49	0	1.45 (N)
NiO	22.9 (Ni)	45.44	31.68	0	-
ZrO_2	22.18 (Zr)	55.87	21.52	0.43	0.9 (N)
ZnO	29.52 (Zn)	44.03	26.45	0	-
Nb_2O_5	12.01 (Nb)	45.11	37.19	5.7	-
Fe_2O_3	29.61 (Fe)	50.83	16.38	3.17	-
MgO	13.07 (Mg)	57.03	29.5	0	-
Ga_2O_3	23.2 (Ga)	43.59	31.12	1.36	0 (N)

Table 4.2: Elemental carbon composition before and after surface etching

Oxides	C1s before etching at. %	C1s after etching at. %
Native SiO_2	9.2	2.65
Al_2O_3	6.98	3.69
CoO	21.38	1.98
MnO_x	39.4	2.09
SiO_2	26.24	3.5
TiO_2	31.17	3.06
In_2O_3	21.09	2.57
Y_2O_3	23.57	0
V_2O_5	32.89	2.59
SnO_2	28.19	2.26
Sb_2O_5	13.49	0
NiO	31.68	6.58
ZrO_2	21.52	0
ZnO	26.45	2.97
Nb_2O_5	37.19	4.32
Fe_2O_3	16.38	0
MgO	29.5	4.04
Ga_2O_3	31.12	0.79

4.2.2 Stability of ALD-Grown Films in Aqueous System

Zeta potential measurements are conducted with aqueous solutions of different pH conditions. Therefore, here we tested the stability of all ALD films prepared in this study. Figure 4.20 shows the stability of each ALD-grown metal oxide film in three different pH values: alkaline (pH=10.5), near neutral (pH=6), and acidic (pH=3.5). Blue represents high stability, where the thickness change is <10% after 2 hours. Orange represents moderate stability, where the thickness reduction ranges from 10% to 50%. Gray represents high instability; the thickness reduction is larger than 50% after 2 hours for these materials. As shown in Figure 4.20, MgO, V_2O_5, and Sb_2O_5 films are generally unstable in water at any pH, which limits their applications in water treatment if no further reinforcement methods are applied. SnO_2, TiO_2, ZrO_2, CoO, MnO_x, SiO_2, In_2O_3, Nb_2O_5, Fe_2O_3, and NiO films are relatively stable over the pH range 3.5 to 10.5. Thus, these metal oxides are potential candidate coating materials for water treatment. For the third category of oxides including Ga_2O_3, ZnO and Y_2O_3 are not stable under acidic conditions, while Al_2O_3 is unstable under basic conditions.

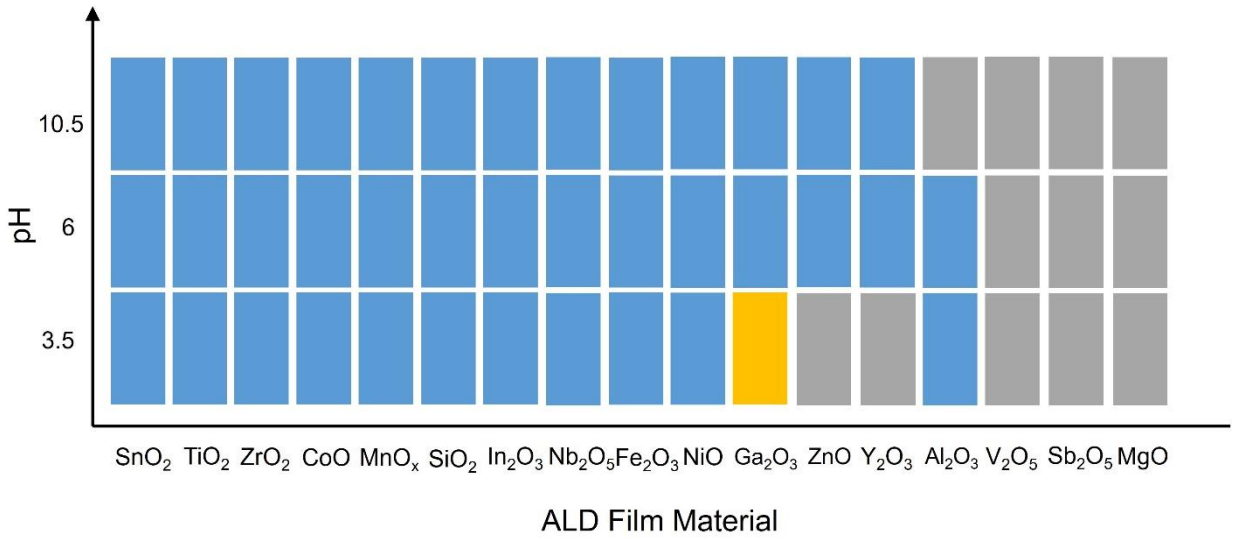

Figure 4.20: Stability of metal oxide films in acidic, neutral, and alkaline aqueous solution. Gray, orange, and blue represent low, moderate, and high stability, respectively.

4.2.3 Water Contact Angle of ALD-Grown Films

Considering the potential of these meal oxides for use as membrane coatings, a thorough understanding of their wetting properties is essential. We characterized the surface wetting properties of these film materials using water contact angle (WCA) measurements (Figure 4.21). The WCAs in air were 15.4°, 21.1°, 21.9°, 22.7°, 23.9°, 31.1°, 32.6°, 33.5°, 42.8°, 43.8°, 44.9°, 45.7°, 46.9°, 47.2°, 48.4°, 57.3°, and 105.3° for SnO_2, MnO_x, ZrO_2, native SiO_2, TiO_2, CoO, NiO, Fe_2O_3, Sb_2O_5, Al_2O_3, Ga_2O_3, ZnO, V_2O_5, Nb_2O_5, SiO_2, Y_2O_3, and In_2O_3, respectively. Among these films, most of the materials exhibit hydrophilic properties, whereas In_2O_3 presents the highest water contact angle, revealing its hydrophobicity. SnO_2 has a highly hydrophilic surface, retaining a tightly bound hydration layer, which can passively repel foulants such as hydrophobic organic molecules and oils. [161, 125] A previous study of ALD Y_2O_3 found that the WCA increased with increasing film thickness from ~42° at 3 nm to 100° at 50 nm due to the

evolution in film crystallinity with thickness.[162] Our finding of WCA = 57.3° at 10 nm Y_2O_3 is consistent with this previous study.

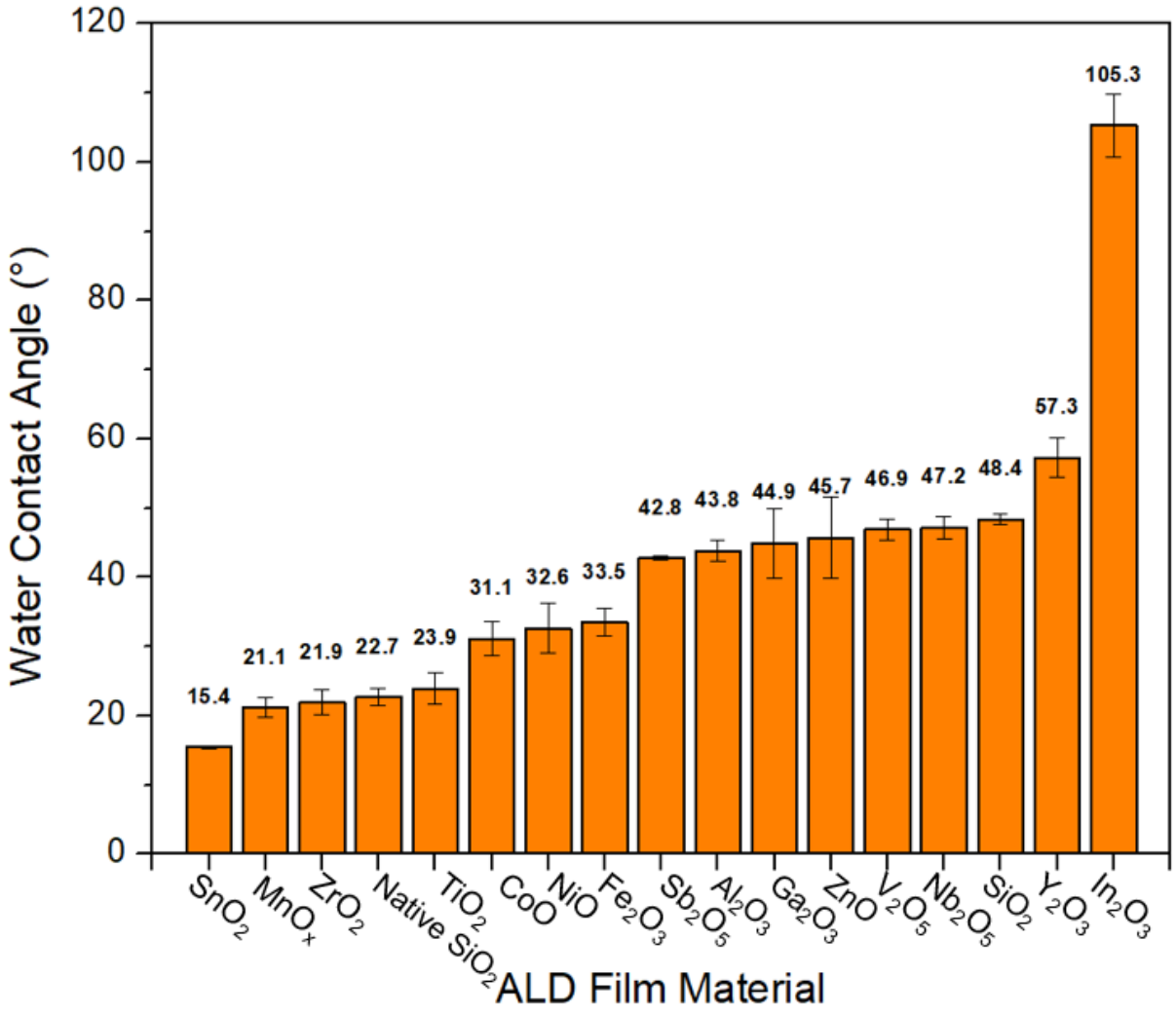

Figure 4.21: Water contact angles of ALD film materials.

4.2.4 Zeta Potential of ALD-Grown Films

Figure 4.22 presents the zeta potential as a function of pH for ALD films under the same KCl concentration of 0.01 M. For each material, the pH at which the transition from positive to

negative zeta potential occurs is called the isoelectric point (IEP), which reflects the pH value for different material surfaces where they carry no net electric charge. Based on the experimental measurements, the IEPs for these ALD films from low to high are NiO, SiO_2, Nb_2O_5, Fe_2O_3, ZrO_2, ZnO (~Fe_2O_3), CoO (~Al_2O_3), Y_2O_3, TiO_2, Ga_2O_3, SnO_2, and MnO_x. These data also reveal that MnO_x, Ga_2O_3, Y_2O_3, and TiO_2 have a relatively higher (positive) surface charge at neutral conditions, while SiO_2 has a strongly negative surface charge. Table 4.3 compares the IEP of these oxides grown through ALD with the IEP values reported in the literature. There is no generally accepted approach to the preparation of materials and characterization conditions when assessing IEP, so some discrepancy in reported values is to be expected. Oxides of certain metals may differ in their degree of hydration and crystallographic form even when carrying the same name. Thermodynamically unstable phases may also undergo phase transformation or hydration/dehydration during an experiment.[163] This variation among nominally similar materials emphasizes the importance of characterizing the zeta potential of interfaces prepared under synthetic conditions as closely as possible to those in the intended application. Particles are unlikely to be a suitable proxy for films, and even among films, those grown by, for example, chemical vapor deposition (CVD) are likely to differ from those grown with ALD. As shown in the Table 4.3, some ALD-grown oxides exhibit similar IEP values compared with values reported in the literature, but there are also some notable exceptions. SnO_2, MnO_x and NiO, for example, vary substantially from earlier reports. For NiO, the discrepancy may be attributed to the film being a composite of NiO, $Ni(OH)_2$, and $NiCO_3$. The existence of multiple oxidation states likely impacts the results for MnO_x. Tin oxide is a more interesting case, and it highlights how much the specifics of material synthesis can influence interfacial electrostatics. ALD-grown SnO_2 films exhibit an IEP of 8, while most reported SnO_2 particles have a much lower IEP (~4).

Looking at the data for a Si wafer with native SiO_2 (~2 nm thickness) and with the data for 200 ALD cycles of SiO_2 whose thickness is around 19.2 nm, the zeta potential is essentially unchanged. This suggests that the film thickness does not play a significant role in determining the zeta potential for the ALD SiO_2 films. Different thicknesses of ZrO_2 (or SnO_2) films also present similar zeta potential profiles. Figure 4.23 shows that 7.1 nm and 15.6 nm ZrO_2 films, for example, have a similar surface charge properties. A previous study found a distinct correlation between the WCA and thickness of ALD Y_2O_3 films and attributed this variation in surface properties to changes in the crystallinity of the ALD Y_2O_3 coatings.[162] The Si native oxide and the ALD SiO_2 coatings are amorphous as-deposited so the crystallinity does not change with thickness. We hypothesize that the zeta potential and other surface properties will not change with thickness for the ALD metal oxide films in this study that deposit in an amorphous state, SiO_2, Al_2O_3, Ga_2O_3, and Nb_2O_5. However, the zeta potential may vary for the other metal oxides that can deposit in a crystalline state if the size and orientation of the crystal change with thickness and deposition conditions.

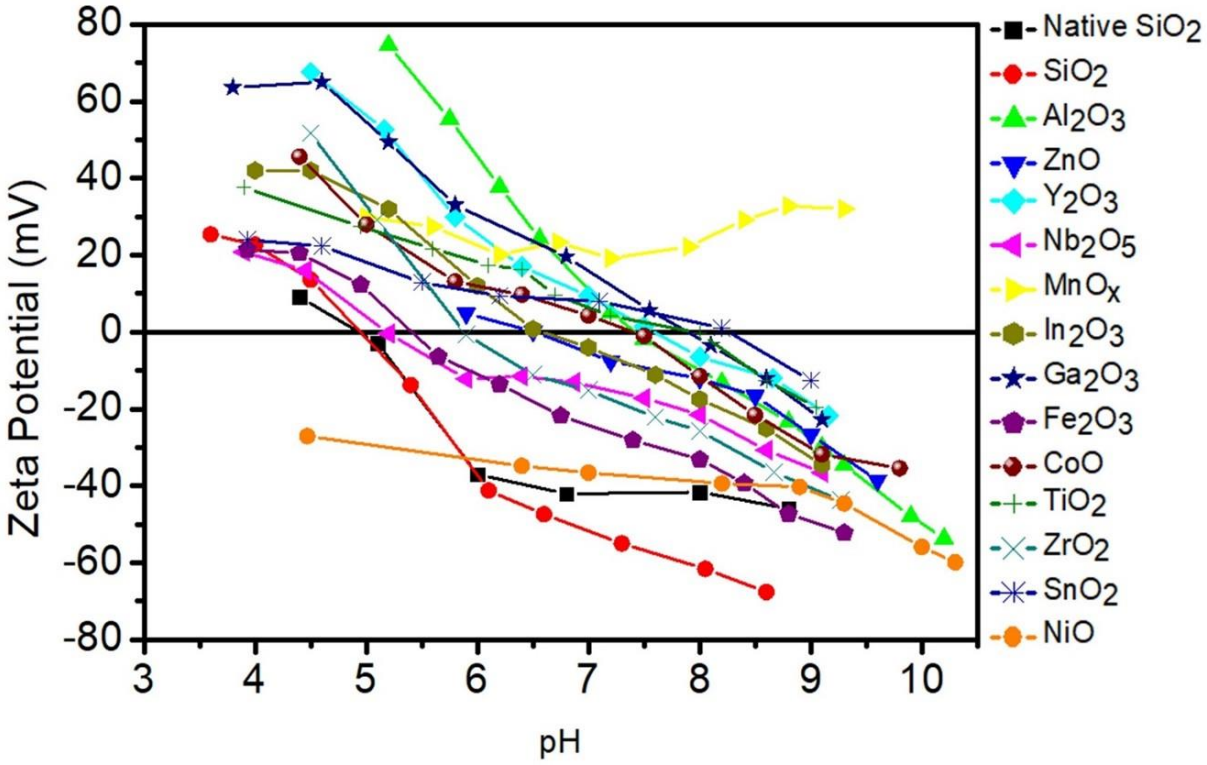

Figure 4.22: Zeta potential curves of a variety of ALD-grown metal oxide films

Table 4.3: IEP comparison with oxides reported in the literature.[163]

Film	IEP from Literature	IEP from this Work
Al_2O_3	7.6 [164]	7.4
TiO_2	5.5-8 [165]	7.9
ZnO	6-10.3 [166]	6.5
ZrO_2	6 [167]	5.9
MnO_x	9.1 [168]	> 9.5
CoO	7.4 [169]	7.4
SnO_2	3.8 [170]	8.2
Ga_2O_3	8.4 [171]	7.9
SiO_2	4.1 [172]	4.9
Nb_2O_5	3.5-5 [173]	5.2
In_2O_3	8.7 [174]	6.5
Y_2O_3	7.6 [175]	7.6
NiO	8.1-9.1 [176, 177]	< 4.5
Fe_2O_3	3-9.4 [178, 179]	5.4

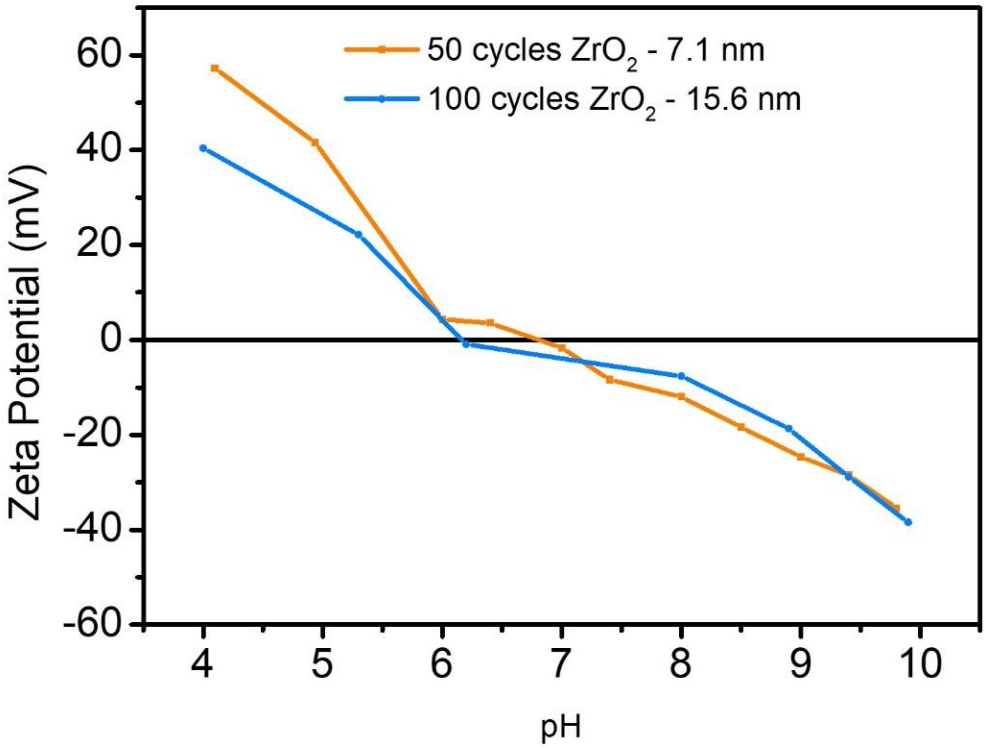

Figure 4.23: Zeta potential curves of different thicknesses for ZrO_2.

4.3 Conclusion

In summary, we have presented characterization of a diverse range of ALD-grown metal oxide films. Some materials (MgO, V_2O_5, and Sb_2O_5) were found to exhibit poor stability in aqueous environments, with thickness decreasing by over 50% within 2 hours of soaking in water, eliminating them from consideration for interface engineering of membranes and other water treatment devices. As a prelude to zeta potential measurement, those films that were sufficiently stable in water were characterized for their wetting properties, which were almost uniformly hydrophilic, with the notable exception of indium oxide. Zeta potential measurements were conducted to investigate the surface charge property for these films. NiO and SiO_2 are

promising candidates as ALD coatings with negative surface charge in aqueous solution, whereas ZrO_2, Al_2O_3, and Ga_2O_3 are promising for positive surface charge coatings at near-neutral pH. Collectively, these results represent a comprehensive study of the water stability, wetting properties, and surface charge properties for many common ALD-grown metal oxide films. We believe this work provides a guideline resource for researchers and technologists in selecting ALD materials for a range of water treatment applications.

4.4 Experimental Methods

Films Grown Using ALD. Growth of ALD oxides was performed in a custom-made hot-wall viscous flow ALD reactor that is described in detail in another study.[180] Ultrahigh purity N_2 was used as a carrier gas with a total mass flow rate of 225 sccm and a background pressure of 0.9-1 Torr. The temperature of the reactor was maintained by a proportional-integral-differential temperature controller with an accuracy of ±0.03 °C. Metal oxide films were deposited on Si (100) substrates with a native oxide layer through self-limiting binary ALD reactions. Table 4.4 shows the ALD processes for the films for this work. For example, for Al_2O_3, trimethylaluminum (TMA, $Al(CH_3)_3$) and H_2O are the metal precursor and co-reactant, respectively. The temperature for both precursors is room temperature (RT). The Al_2O_3 ALD was performed at 200 °C using the time sequence: 1 s TMA dose/ 10 s N_2 purge / 1 s H_2O dose/ 10 s N_2 purge, which we denote as 1:10:1:10 in the recipe column in Table 4.4. The ligands and compounds listed in Table 4.4 are methyl (Me), ethyl (Et), cyclopentadienyl (Cp), methylcyclopentadienyl (MeCp), ethoxide (OEt), 3-aminopropyltriethoxysilane (APTES), isopropyloxide (OiPr), dimethylamido (NMe_2), and N, N′ -di-isopropylacetamidinato (AMD).

The thicknesses of the grown films were measured using spectroscopic ellipsometry. Each metal oxide film showed a distinct growth per cycle value, a characteristic of ALD processes. The number of ALD cycles were adjusted to yield a consistent film thickness of ~10 nm for each material and to ensure a continuous coating where the surface chemical properties are independent of the substrate.

Table 4.4: Summary of ALD process parameters used to prepare the films in this study.

Film	Precursor/Co-reactant	Precursor/Co-reactant Temperatures (°C)	Recipe Time Sequence (s)	Reaction Temperature (°C)
Al_2O_3[181]	$Al(CH_3)_3/H_2O$	RT/RT	1:10:1:10	200
TiO_2[181]	$TiCl_4/H_2O$	RT/RT	1:10:1:10	200
ZnO[181]	$Zn(Et)_2/H_2O$	RT/RT	1:10:1:10	200
MgO[182]	$Mg(Cp)_2/H_2O$	65/RT	2:10:1:10	200
ZrO_2[183]	$Zr(NMe_2)_4/H_2O$	75/RT	1:10:1:10	200
MnO_x[184]	$Mn(EtCp)_2/H_2O$	90/RT	1:10:1:10	200
CoO[185]	$Co(AMD)_2/H_2O$	100/RT	5:20:5:20	200
SnO_2[186]	$Sn(NMe_2)_4/O_3$	45/RT	1:20:1:20	200
Sb_2O_5[187]	$Sb(NMe_2)_3/O_3$	43/RT	2:20:2:20	200

Continued on next page

Table 4.4 - *Continued from previous page*

Ga_2O_3[188]	$Ga_2(NMe_2)_6/H_2O$	75/RT	3:15:1:10	200
V_2O_5[189]	$VO(OiPr)_3/H_2O$	72/RT	2:20:2:20	200
SiO_2[190]	$APTES/H_2O/O_3$	100/RT/RT	2:15:2:10:10:15	200
Nb_2O_5[191]	$Nb(OEt)_5/H_2O$	150/RT	2:10:1:10	250
In_2O_3[192]	$In(Cp)_3/H_2O/O_2$	45/RT/RT	3:5:4:5:4:5	200
Y_2O_3[193]	$Y(MeCp)_3/H_2O$	154/RT	1:5:1:5	270
NiO[194]	$Ni(Cp)_2/O_3$	100/RT	5:10:5:10	250
Fe_2O_3[195]	$Fe(Cp)_2/O_3$	85/RT	2:10:5:10	250

XPS Characterization. XPS measurements were carried out on a Thermo Fisher k-Alpha+, and the spectra were analyzed using Thermo Fisher Avantage software. The X-ray source was a micro-focused monochromatic Al Kα (1487 eV) with a spot size of 400 μm. Survey scans used a pass energy of 200.0 eV and a step size of 1.000 eV, and high-resolution XPS scans used a pass energy of 50.0 eV and a step size of 0.100 eV. For each measurement, an average of five scans was reported. All the spectra were referenced to the C1s peak at 284.8 eV.

Water Contact Angle Measurements. Surface wettability was investigated using a static water contact angle measurements system (DSA 25E, KRÜSS) and the sessile drop method. Before the measurement, all films are cleaned through a sequence of sonication in toluene, acetone, isopropyl alcohol (IPA), and reverse osmosis (RO) water for at least 10 minutes each. Impurities from exposure to ambient environments can influence wetting and electrostatic properties. All substrates were cleaned immediately before characterization to remove such contamination. In applications, it is likely that exposure to a process stream would achieve a similar washing effect. RO water is used to test the water contact angle. Values of at least three different spots on each sample were averaged to obtain the reported angles.

Ellipsometry Measurements. Measurements were performed on a J.A. Woollam M-2000 ellipsometer and a J.A. Woollam alpha-SE ellipsometer. The data were collected at multiple angles with 328 wavelength steps from 380 to 900 nm. Analysis was performed using CompleteEASE 5.1 software. The thickness of the native oxide layer on the Si substrates is ~20 Å. Thicknesses of the films were fitted based Cauchy model. Before the measurement, all films are cleaned through a sequence of sonication in toluene, acetone, isopropyl alcohol (IPA), and reverse osmosis (RO) water for at least 10 minutes each.

Zeta Potential Measurements. Before the zeta potential measurement for each film, a stability test is conducted. Coated samples are soaked in three aqueous solutions: $HCl_{(aq)}$ (pH = 3.5), RO water (pH = 6), and $KOH_{(aq)}$ (pH = 10.5) for two hours, separately. The thickness of the ALD films is measured before and after soaking using an ellipsometer to monitor for partial or total dissolution of the coated material. Subsequent zeta potential measurements are conducted over a pH range for which each material is stable as determined by these dissolution measurements.

Membrane zeta potentials were measured using streaming potential measurements performed with an adjustable gap cell in a SurPASS 3 system (Anton Paar). The zeta potential can be calculated based on the Smoluchowski equation. [196, 197]

$$\zeta = \frac{dU}{dp}\frac{\eta}{\varepsilon\varepsilon_0}\kappa$$

Before the measurement, all films are cleaned through a sequence of sonication in toluene, acetone, IPA, and RO water for at least 10 minutes each. The electrolyte for all the measurements is 0.01 M KCl aqueous solution. pH is adjusted via two syringe pumps dispensing titration reagent (0.05 M HCl and 0.05 M KOH). The reference material is a polyvinylidene fluoride (PVDF) membrane provided by Anton Paar. Each zeta potential data point is calculated by repeating the measurement four times, and two to four different samples are tested for each metal oxide film. The experimental error of the zeta potential is within $\pm$ 10 mV.

Appendix B

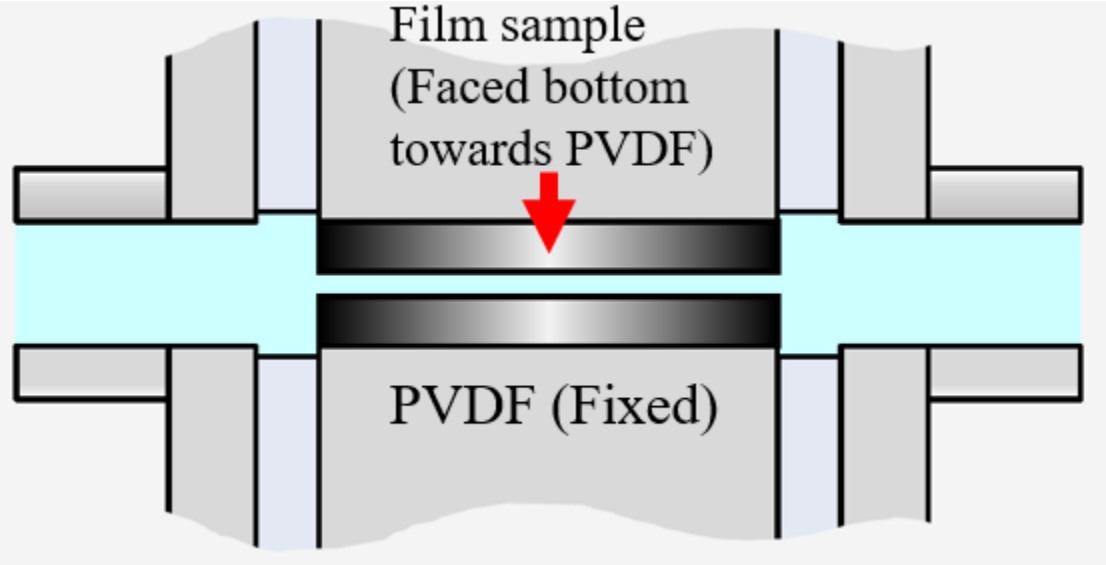

Figure 4.24: Schematic of the sample holder for the zeta potential measurement.

The bottom side of the sample holder is fixed, the material is PVDF, we can put the film on the top side. The as-measured zeta potential value ($U_{measured}$) combine the data of both PVDF and film sample. Thus, before the measurement, we put another PVDF on the top, and get the zeta potential of PVDF reference (U_{ref}). Then the zeta potential of the film sample could be calculated.

$$U_{film} = 2U_{measured} - U_{ref}$$

Chapter 5: ALD-GROWN JANUS MEMBRANES FOR IONIC RECTIFICATION

Ion transport through porous media within aqueous systems is a topic of profound interest from both fundamental and applied science and engineering perspectives. Intimately understanding and tailoring transport properties is a grand challenge in the field. Engineered membranes with non-trivial interfacial properties offer a powerful new tool toward this end. Intelligent molecular and ionic transport control at the nanoscale has the potential to impact applications including osmotic energy conversion, ion pumps, and biosensors. To understand ion transport properties in depth, it is desirable to design and construct high-performance heterogeneous membranes with tailored selectivities, such as rectified ion transport. Janus membranes, having differing properties on opposing faces, have emerged as a new strategy for achieving ion rectification. To date, the methods used to combine two different membranes to realize such heterogeneous structure suffer from significant drawbacks. These relatively uncontrollable processes and weak interfacial interactions have limited the understanding of ion transport process as well as the practical use of these membranes. Herein, we explore a highly customizable process to control the properties of Janus membranes. ALD can deposit materials uniformly and with high precision and controllability on arbitrarily complex and large substrates. Thus, ALD is a promising way to fabricate Janus membranes and to develop systematic models to help us understand ion transport. Deposition of different metal oxides selectively on one face of a membrane enables one to tune the electrostatics of the interface. Experiments will be guided by simulations performed by collaborators in the de Pablo group. These simulations will suggest pore geometries and surface charge spatial distributions that are likely to produce high rectification ratios. Experiments will aim to realize these optimized designs and then serve to

provide feedback to enhance the simulations, forming a virtuous cycle with continuous improvements in understanding and performance.

5.1 Introduction

Membranes are an important component of technologies with applications in energy and water. Membrane processes involve selective/directional mass transport through pores, which is often thermodynamically unfavorable. To make the process continuous, external energy input is essential. Minimizing this energy input is a grand challenge in the field, and conventional membranes have proven unable to achieve significant progress. Thus, new strategies are needed. Janus membranes are a new class of membrane with asymmetric properties on each side, which can provide an inner driving force at the junction barrier to control the ion transport process inside pores. This inner driving force provides an additional potential, facilitating the expected mass or energy flow when it aligns with the external driving force while impeding those flows when counter-aligned. Because of the unique structure of the Janus membrane, it has been designed and used in many areas ranging from mass separation[198] to energy harvesting[199, 145, 200].

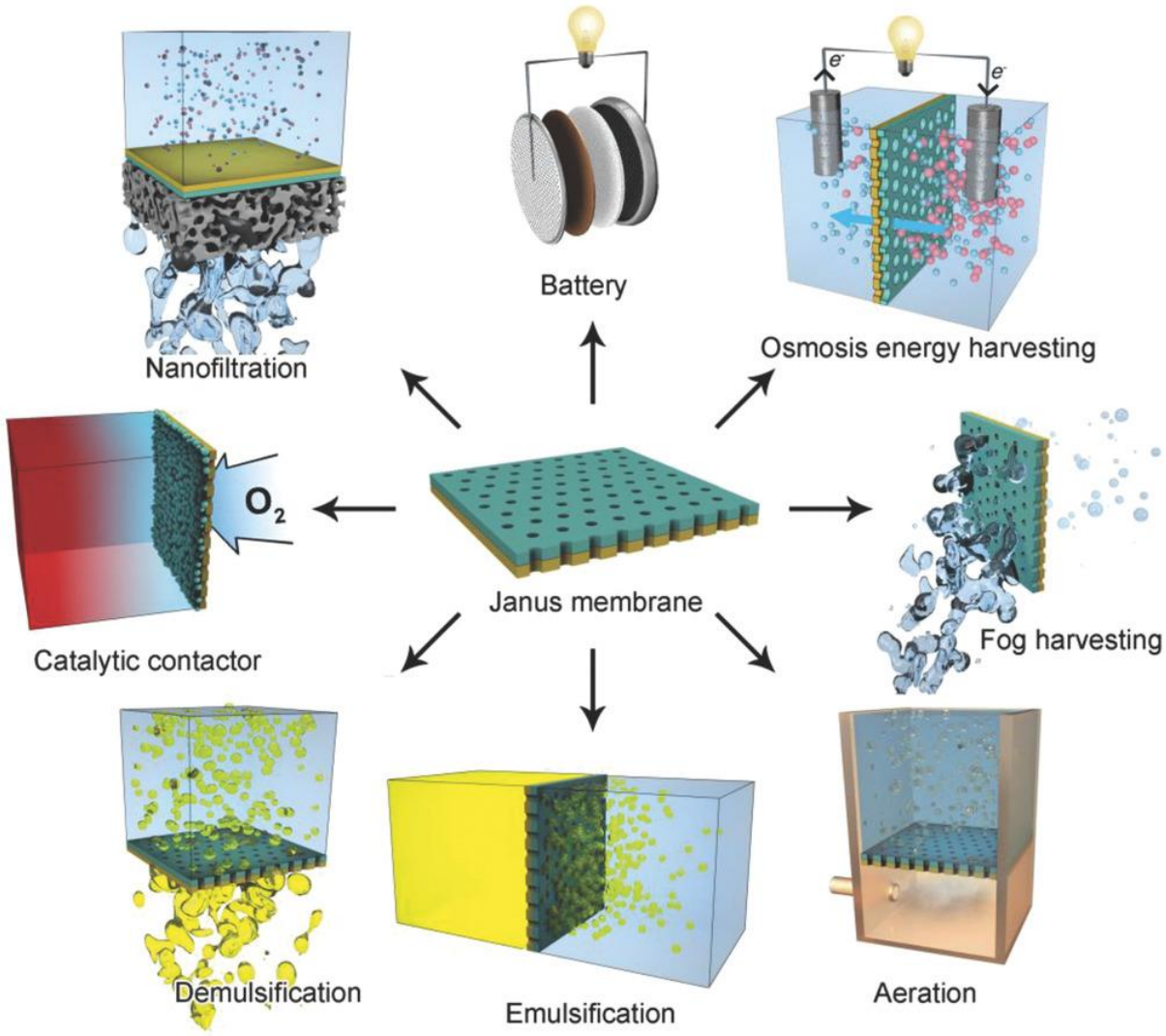

Figure 5.1: Illustrative potential applications of Janus membranes. Reproduced from ref. [52].

Nature has provided inspiration for Janus membrane architectures.[201, 202] The cytomembrane, for example, possesses a typical Janus structure, whose outside has a positive charge, and inside negative. Such asymmetric structure enables ion transport across the cytomembrane with a selective direction to maintain cell function.[203] Inspired from the natural world, the study of Janus membranes with asymmetric surface charge launched at the end of last century and gained increasing attention recently as the potential utility to address major societal

water challenges becomes clearer (Figure 4a). The earliest Janus membranes were bipolar membranes, each layer of which only allowed selective permeation of certain cations or anions to realize selective ion transport. This feature demonstrated Janus membranes with an asymmetric surface charge to be good candidates for ion-based batteries or other systems involved with ion transport processes such as osmotic energy harvesting and nanofiltration.[204, 205, 206, 207, 208, 52]

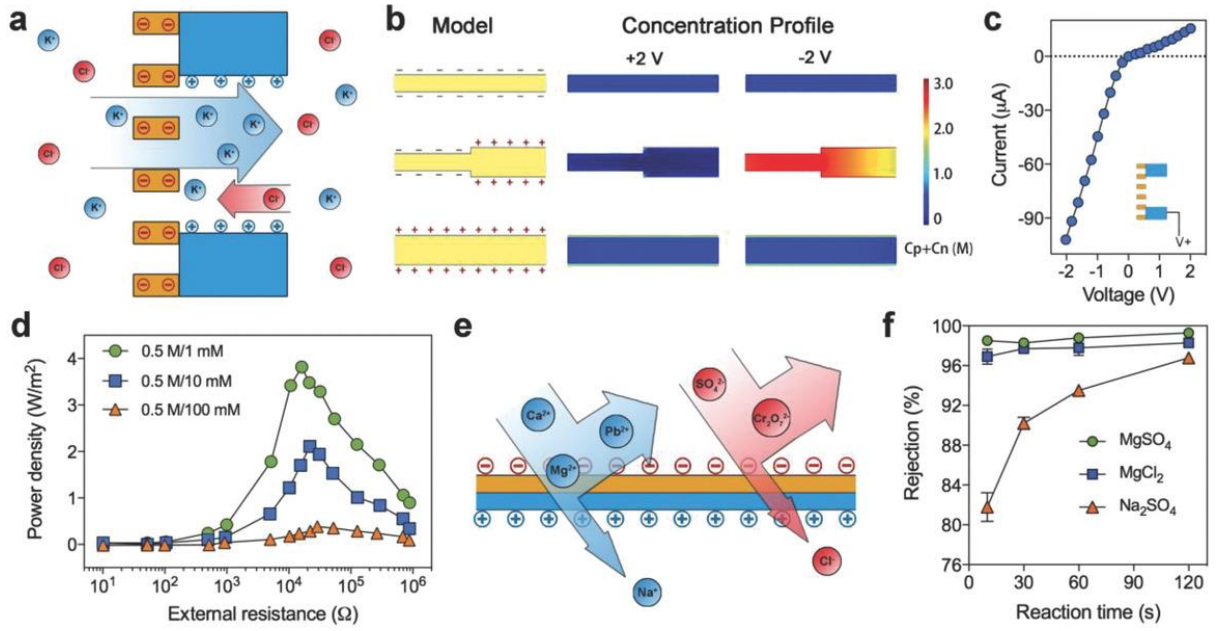

Figure 5.2: Applications of Janus membranes with asymmetric surface charges. a) Diagram of a Janus membrane applied in energy generation by salt concentration difference. K+ ions transport selectively through the membrane. b) Calculated ionic concentration distribution in positively charged, negatively charged, and Janus membranes. These results confirm the ionic rectification is caused by ion depletion and accumulation induced by asymmetric polarity under different external bias. c) I-V curve of the Janus membrane in 0.1 M KCl solution, reflecting the ionic rectification effect of the asymmetrically charged membrane. d) Power density generated using a Janus membrane under different salinity gradient and resistance. e, Diagram of a Janus membrane used in nanofiltration. The negatively charged layer rejects the multivalent anions while the positively charged one rejects multivalent cations. f, Salt rejection of a Janus nanofiltration membrane. A positively charged layer was formed initially, while the negatively charged layer formed with the increase of reaction time. Reproduced from ref. [52].

For Janus membranes, the efficient ion-selective transport mechanism is based on the presence of nanopores with heterogeneity in electrochemistry and structure. The fluidic channels inside the Janus membranes follow a similar principle to ionic diodes[209], i.e. bipolar nanopores showing different ion conductance under different bias polarities because of the asymmetric surface charge.[210, 145] Fundamentally, the change of conductance originates from the originally asymmetric cation/anion distribution on each side of the nanopores at equilibrium (Figure 5.2 b). When an external electric field is applied, the ion current is proportional to the original equilibrium ion concentration.[211] Therefore, under bias polarity, when the outward ionic flow is larger than the inward ionic flow, the nanopore is depleted, leading to lower ionic conduction. When the applied electric field is reversed, it can lead to an accumulation of ions in the pores and results in higher ionic conductivity. This nonlinear ionic conductivity response eventually leads to the ionic rectification performance for ionic diodes (Figure 5.2c). In addition, higher surface charge density can lead to better ionic selectivity and conductance. This would allow the processing of more concentrated solutions within Janus membranes; otherwise, the concentrated ion solutions can offset the surface charges within the nanopores, excluding the occurrence of electrical double layer overlap and subsequent ion-selective transport.

Osmotic energy existing in seawater is regarded as a sustainable energy source because of the large reserves and easy accessibility.[136, 212, 198] Janus membrane can also work for nanofiltration (Figure 5.2 e, f). Janus membranes can be effective for osmotic energy harnessing because the bipolar structure with opposing polarity can form an abrupt change of the cation or anion concentration at the interface. The energy conversion efficiency could be promoted by optimizing the pore geometry and the surface charge density. This simple and versatile configuration is amenable to numerical simulation and subsequent optimization.[213, 214, 215] More

advanced treatments that look at non-equilibrium effects relevant during transport are also possible.

One of the biggest challenges in advancing Janus membrane concepts is the fabrication of membranes with opposing properties on their two faces. Many strategies have been applied to membrane surface modification[203], but asymmetric membrane fabrication remains challenging. The main problem is that the porous structure of membranes often leads to wholly, not asymmetric, modification due to the capillary effect during the widely applied wet chemistry modification process. To date, to realize this asymmetric surface charge heterostructure, many membrane materials, and synthetic methods have been attempted, like asymmetric modification, packing nanoparticles modified with different functional groups, covalent modification, and ALD, among other methods.[202, 205, 208] ALD, in particular, has been demonstrated recently as a powerful tool in that, in many cases, it can offer arbitrary control over the shape or the gradient of the property from one membrane face to the other. In this work, we tried two different approaches to fabricate Janus membranes based on ALD technology. The first approach was based on commercial isotropic anodic aluminum oxide (AAO) membrane, and the second method was based on our own designed isoporous silicon nitride (Si_3N_4) membrane.

5.2 Results and Discussion

5.2.1 Fabricating Janus Membrane Based on Commercial AAO Membrane with ALD

ALD is a thin film deposition technique based on the sequential use of a gas phase chemical process, which can be used for surface modification. Compared with other Janus membrane synthesis methods, ALD is an efficient way to precisely control the morphology, thickness, pore size, and surface charge density. Typically, ALD results in a uniform, conformal

coating—even for convoluted substrates with tortuous interior pore structures. However, if one selects a membrane for which the pore size is comparable to or smaller than the mean free path of the vapor-phase precursors, a gradient evolution of the deposited material can be created in accordance with the diffusion process. To realize a bipolar ionic diode heterostructure using the ALD technique, we propose two deposition strategies: one-side functionalization and two-side functionalization. Commercial anodic aluminum oxide (AAO) membranes serve as a convenient template from which to fabricate the Janus architectures. AAO has good thermal stability, opening up a wide ALD processing window. The oxide substrate material is also amenable to a range of ALD chemistries, and a variety of pore diameters are available. Moreover, AAO membranes typically have asymmetric pore geometry as a result of the anodization-based fabrication process. This geometric asymmetry can be exploited to enhance the ion rectification property.

In order to prepare Janus membranes using ALD, it is necessary to restrict the exposure to the vapor-phase precursors to one side of the substrate. A special holder for AAO membranes has been designed to this end, which can seal off the bottom side of the membrane to ensure that diffusion and grown initiates at the top side of the AAO membrane. (Figure 5.3) Once the membrane is sandwiched by the holder, the precursor will only diffuse from the top pore into the channel. By controlling the soak time, the metal oxide will ideally grow on only one side of the nano-channel.

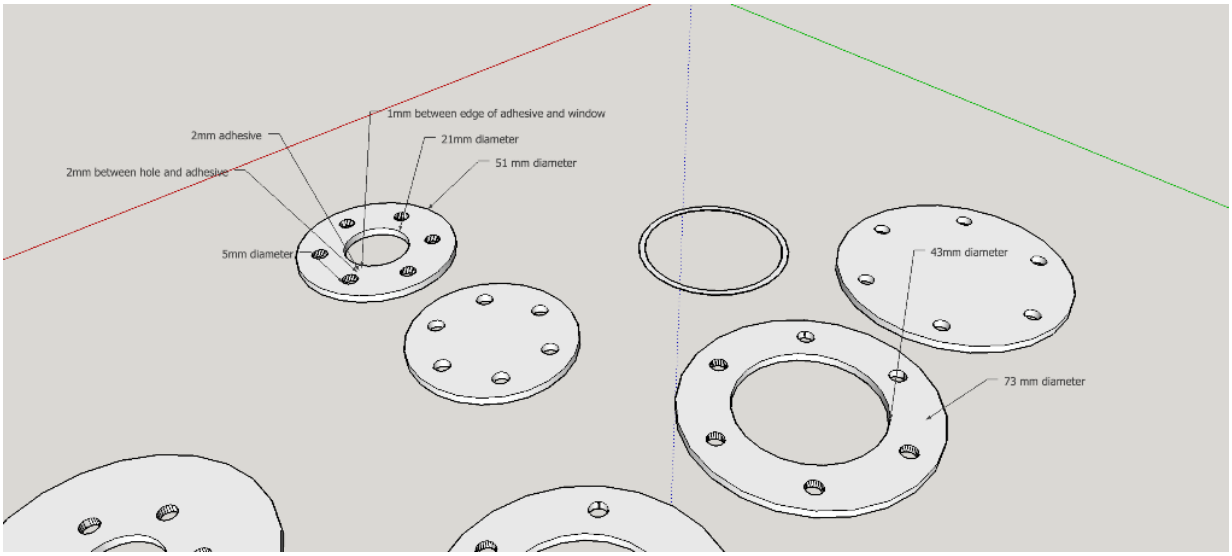

Figure 5.3: Schematic for Janus membrane holder for ALD.

The isotropic AAO membrane was purchased from InRedox Company, the mean pore size of which is 28 nm. The pore density of the AAO membrane is 5×10^{10} cm^{-2}. Figure 5.4 shows the surface and the cross-section structure of the AAO membrane. This isotropic AAO membrane has a different structure compared to typical AAO membranes. Typical AAO membranes exhibit two distinct layers, the top layer has pores with a narrow diameter (for example, 20 nm), while bottom 40 µm thickness has larger pores, around 200 nm, working as the supporting layer. To fabricate sandwich structure within the Debye length scale, the isotropic AAO membrane was chosen as the template. For ALD functionalization, one side was exposed to the vapor-phase precursors, while the other side was sealed off. Based on the results of Chaper 4, ALD-grown SnO_2 film is very stable in water, and it has strong positive surface charge, so we choose SnO_2 as the first deposition material. Process conditions were selected to deposit tin oxide only on the exposed face, stopping the precursor diffusion with a nitrogen purge before the molecules could make their way deeper into the pores.

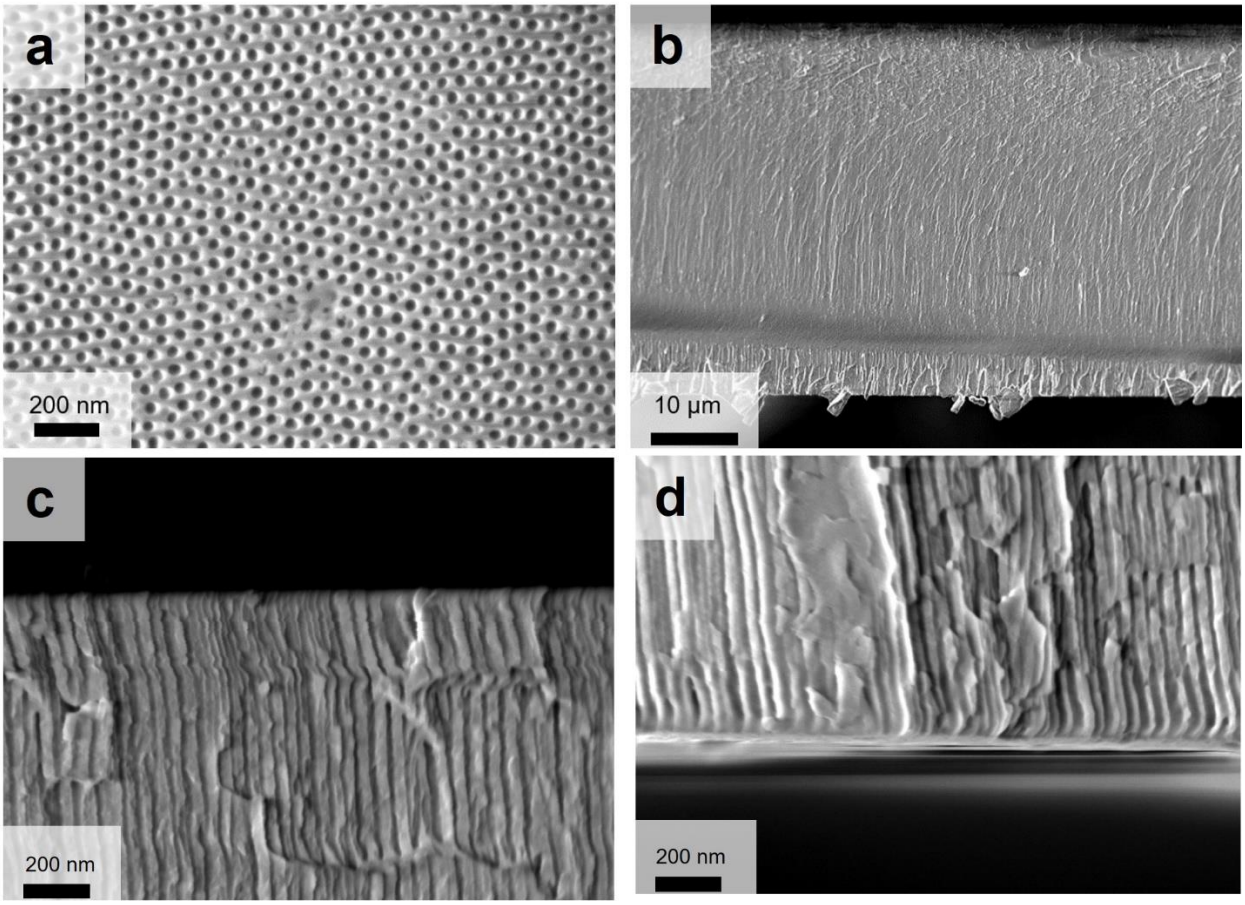

Figure 5.4: SEM images of commercial isotropic AAO membrane with uniform pore size. (a) Top view of AAO membrane with mean pore size of 28 nm. (b) Cross-section of AAO membrane with the thickness of 50 µm. (c-d) Zoom-in cross-section of AAO membrane, showing the straight uniform channels.

To map out the relationship between the final pore size and the ALD process parameters, samples were prepared with 40, 80, and 160 cycles of ALD, followed by structural and performance characterization. Details of these experiments are described below. By changing ALD processing parameters (cycle number, oxide material, pressure, time, temperature), we aim to replicate the (optimized) ionic rectification. Characterization of the resulting membranes will provide powerful data for feeding back to the simulations and refining them to project further performance enhancements.

Magnesium oxide (MgO) was chosen as the opposite charge coating materials to be grown by ALD, paired with the tin oxide. SnO_2 was firstly grown on one side of AAO, while MgO on the other side. Tetrakis(dimethylamino)tin (TDMASn) was the tin source, bis(ethylcyclopentadienyl) magnesium ($Mg(CpEt)_2$) the magnesium source, and water the oxygen source. The heater was set at 55 °C, and the chamber temperature was 100 °C. Before fabricating sandwich structures, we separately deposit SnO_2 and MgO on separate AAO membranes to characterize the growth processes.

During the deposition of SnO_2, the TDMA Sn dose time was 0.5 s and the purge time was 45 s; then, the water dose time was 0.15 s and the purge time was 60 s. Figure 5.5 shows that the pores of AAO membranes were narrowed down to 17, 12, and 6 nm after 40, 80, and 160 cycles of SnO_2 deposition, respectively. After 120 cycles, the pore size of AAO membrane shrunk down to below 10 nm.

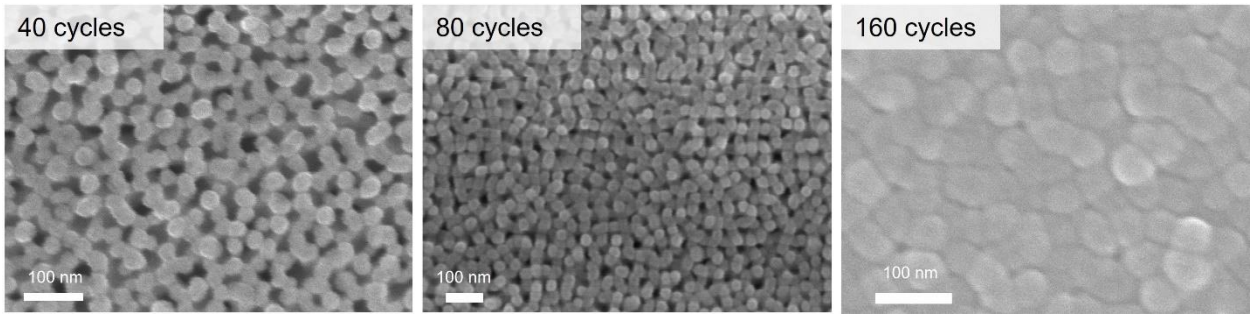

Figure 5.5: SEM images of SnO_2 coated AAO membrane with different cycle number

During the deposition of MgO, the $Mg(CpEt)_2$ dose time was 0.5 s and the purge time was 45 s; then, the water dose time was 0.15 s and the purge time was 60 s. Figure 5.6 shows that

the pores of AAO membranes were narrowed down to 20 and 12 nm after 40 and 160 cycles of SnO_2 deposition, respectively.

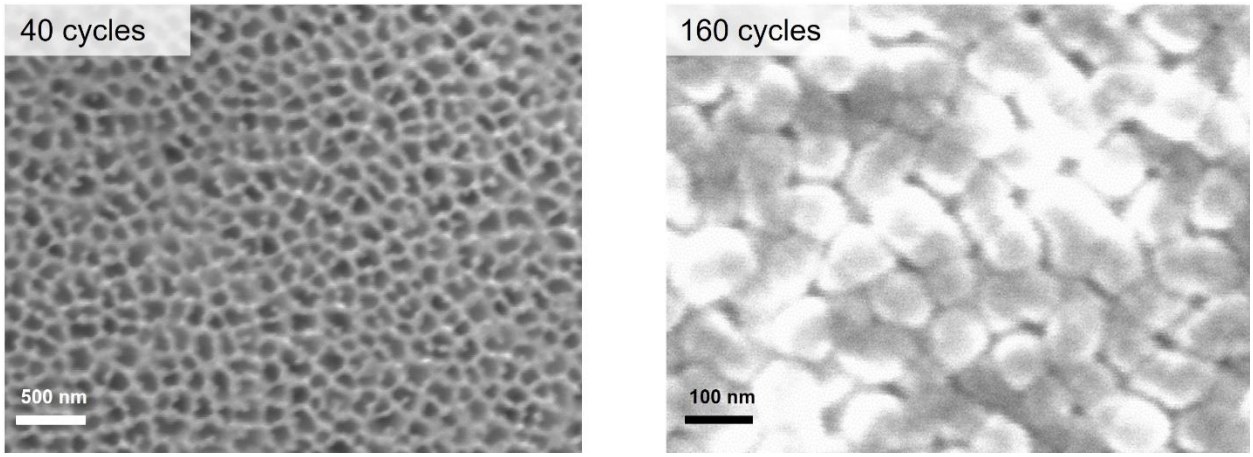

Figure 5.6: SEM images of MgO coated AAO membrane with different cycle numbers

After determining the growth rate of SnO_2 and MgO, we fabricated a MgO-AAO-SnO_2 sandwich structured membrane. The ALD recipes were [give which specific conditions were selected].

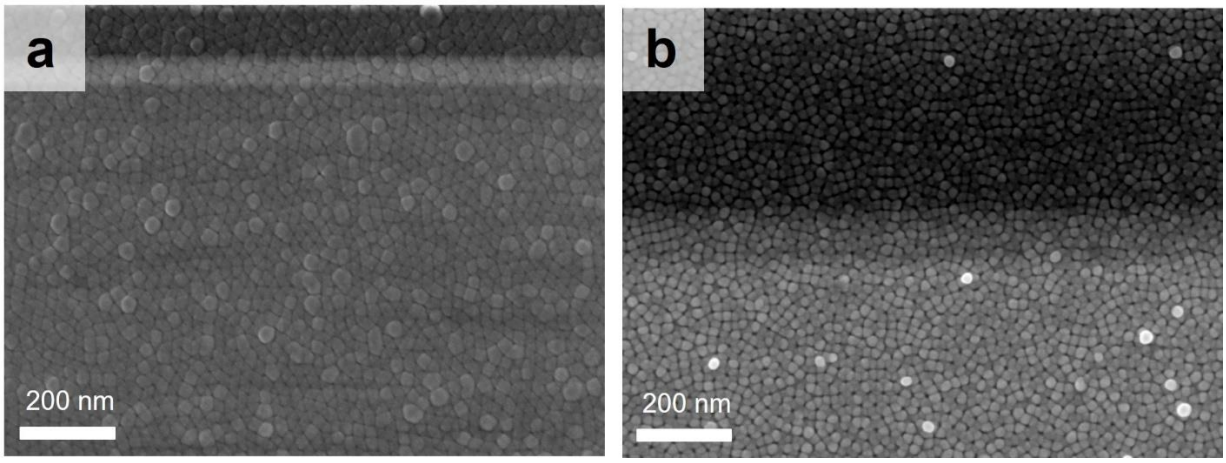

Figure 5.7: SEM images of MgO-AAO-SnO2 sandwich structured membrane. (a) Top side SEM, with 160 cycles of SnO_2, (b) Bottom side SEM, with 160 cycles of MgO.

As shown in Figure 5.7, the MgO-AAO-SnO_2 sandwich structured membrane has mean pore size of 6 nm on the SnO_2 deposited side and a mean pore size of 12 nm on the MgO deposited side. Figure 5.8 shows the EDS elemental mapping of the cross-section of MgO-AAO-SnO_2 sandwich structured membrane. Al and O elements are dispersed evenly along the channel because of the substrate composition (Al_2O_3), while tin is only present on one side of the membrane, indicating the successful coating of SnO_2 on one side. Mg signal surprisingly appears on both sides, which may be a result of contamination in the reactor. Further studies are underway to identify and eliminate this issue.

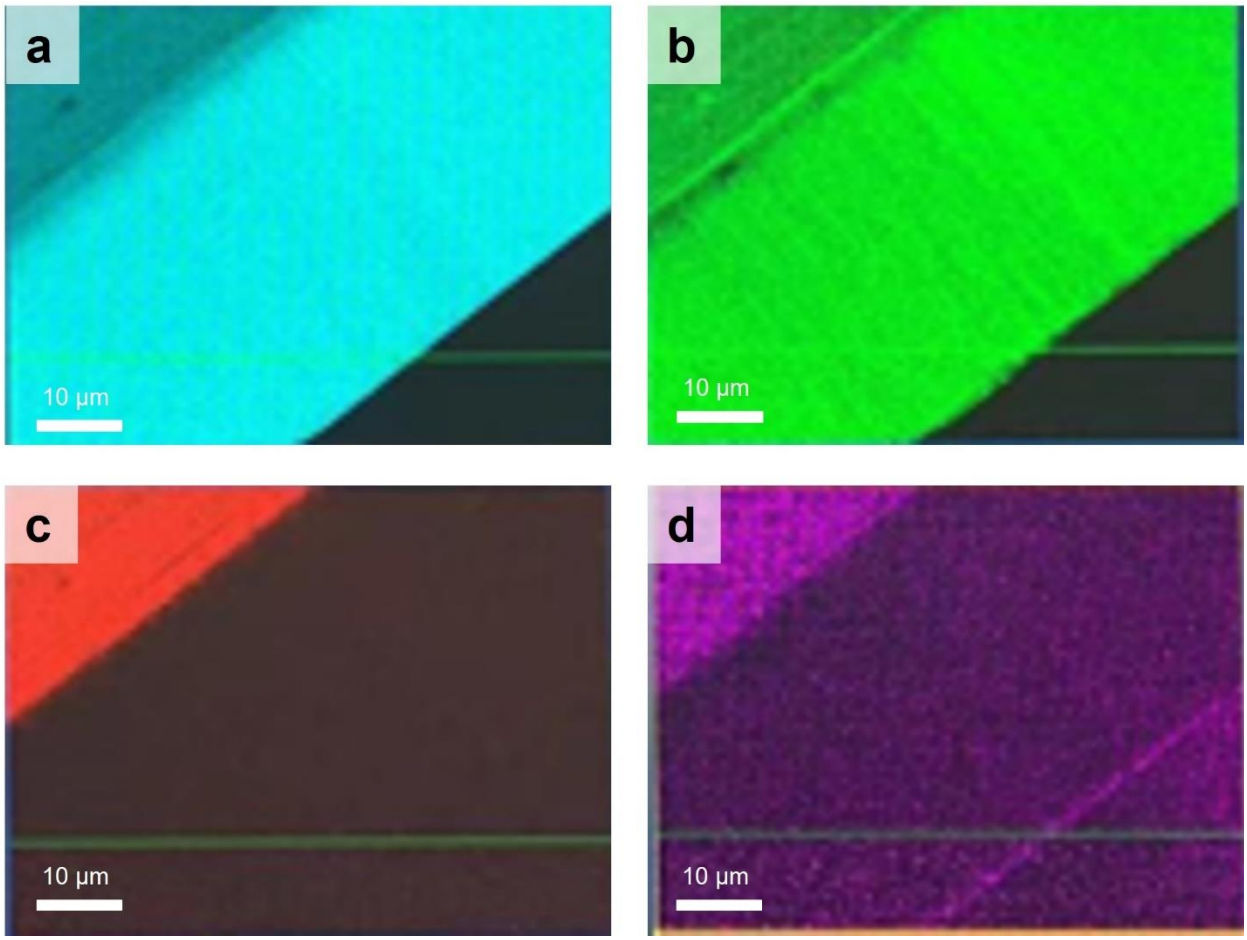

Figure 5.8: EDS mapping of the cross-section of MgO-AAO-SnO_2 sandwich structured membrane. (a) Al, (b) O, (c)Sn, and (d) Mg.

5.2.2 Fabricating Janus Membranes on Silicon Nitride Membranes with ALD

Due to the large thickness of commercial AAO membranes, the system cannot be fully analyzed through molecular dynamics simulations, which limits the guidance simulations can provide toward membrane design. In addition, commercial membranes generally exhibit wide pore-size distribution and inconsistent pore size between different individual membranes. To pursue an experimental platform that would be more amenable to simulations and that would

exhibit uniform and reproducible transport behavior, we designed and fabricated isoporous silicon nitride (Si_3N_4) membranes through a sequence of nanofabrication processes, as follows:

Step one: To produce 2.5 mm by 0.7 mm silicon nitride (SiN) membranes, we use a double-sided 100 nm SiN coating on a 500 μm silicon wafer. SiN can provide a high etching resistance to KOH solution, which is used to release the membranes at the final step. Firstly, we deposit gold on the front side as a global marker to align the front-side pattern with the back side pattern in the following step.

Step two: Si can be etched in KOH solution forming a characteristic V-etch with sidewalls that produces a 54.7-degree angle with the surface. In order to obtain a 2.5 mm by 0.7 mm membrane area on the front side after KOH etching, we used photolithography to create a 3.2 mm by 1.4 mm Si window on the back side.

Step three: After fabricating the back pattern, we deposit ~9 nm-thick random copolymer, called a "mat", on the front side. This layer can form a neutral condition of the block copolymer (BCP) we will use, which helps us obtain a perpendicular cylinder structure. Then we use e-beam lithography to write a hexagonal geometry with 4× density multifaction on this mat layer. After O_2 plasma removes the patterned area, Si is exposed to air, which allows us to graft hydroxylated polystyrene (PS-OH) onto the surface. After grafting PS-OH, we spin coat ~90 nm PS-*b*-PMMA on top and anneal it under 270 °C for 2 h to grow a cylindrical geometry of this BCP.

Step four: In order to enhance the properties of porous structures so that the percolated structure can transfer to the underlying Si_3N_4 layer, the sequential infiltration synthesis (SIS)[62]

process is applied to interact TMA precursors with polar groups on the polymer, forming nanoporous AlO_x from an organically defined structure.

Step five: We deposit a 20 nm gold protection layer on top of the SIS layer because we cannot directly do photolithography on the SIS layer. Next, we use photolithography to create a 2.5 mm by 0.7 mm area aligning with the back side 3.2 mm by 1.4 mm window. We use gold etchant to remove the gold layer, O_2 plasma etching to remove all PS block to create our porous scaffold, and a fluoride gas-based etching to transfer the geometry in the SIS layer to the Si_3N_4 layer. Finally, we remove all layers on top of the Si_3N_4 to make sure the surface is clean and ready for KOH back etching.

Step six: Due to the brittle nature of ultrathin Si_3N_4 membranes, we coat the front side of the Si_3N_4 membrane with a 150 nm thick PMMA layer to prevent the KOH solution from penetrating through the membrane. We only expose the back side of the Si_3N_4 to an 80 °C KOH solution and wait until there are no further H_2 bubbles generated. After the membrane is dried, we use O_2 plasma to remove the PMMA layer.

Finally, a Si_3N_4 membrane with a thickness of 100 nm will be released.

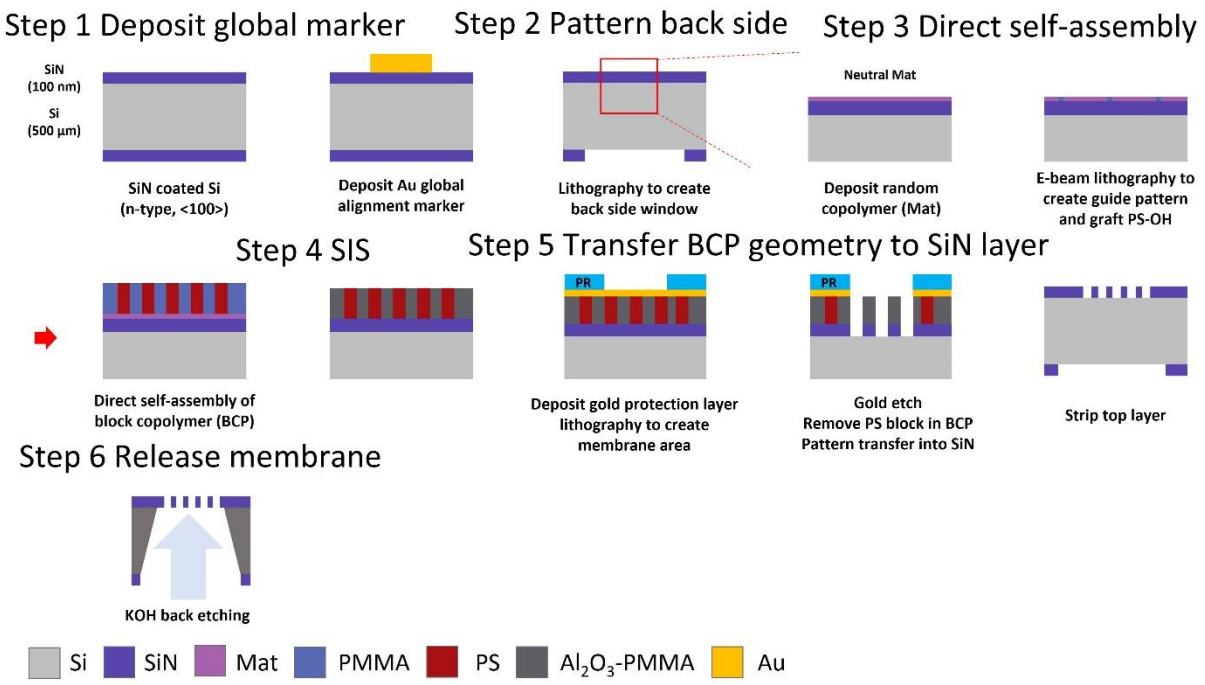

Figure 5.9: Scheme of the nanofabrication process of the Si_3N_4 membrane.

The lateral size of the Si_3N_4 membrane is controlled to be 2.5 mm × 0.7 mm (Figure 5.10a). The membrane has funnel-shaped channels with a length of 100 nm (Figure 5.10b). The front side and back side SEM images show that the Si_3N_4 membrane has a mean front side pore size of 23.5 nm and mean back side pore size of 17.0 nm with high uniformity. These isoporous Si_3N_4 membranes could serve as an improved platform for ion transport studies through confined charged nanochannels.

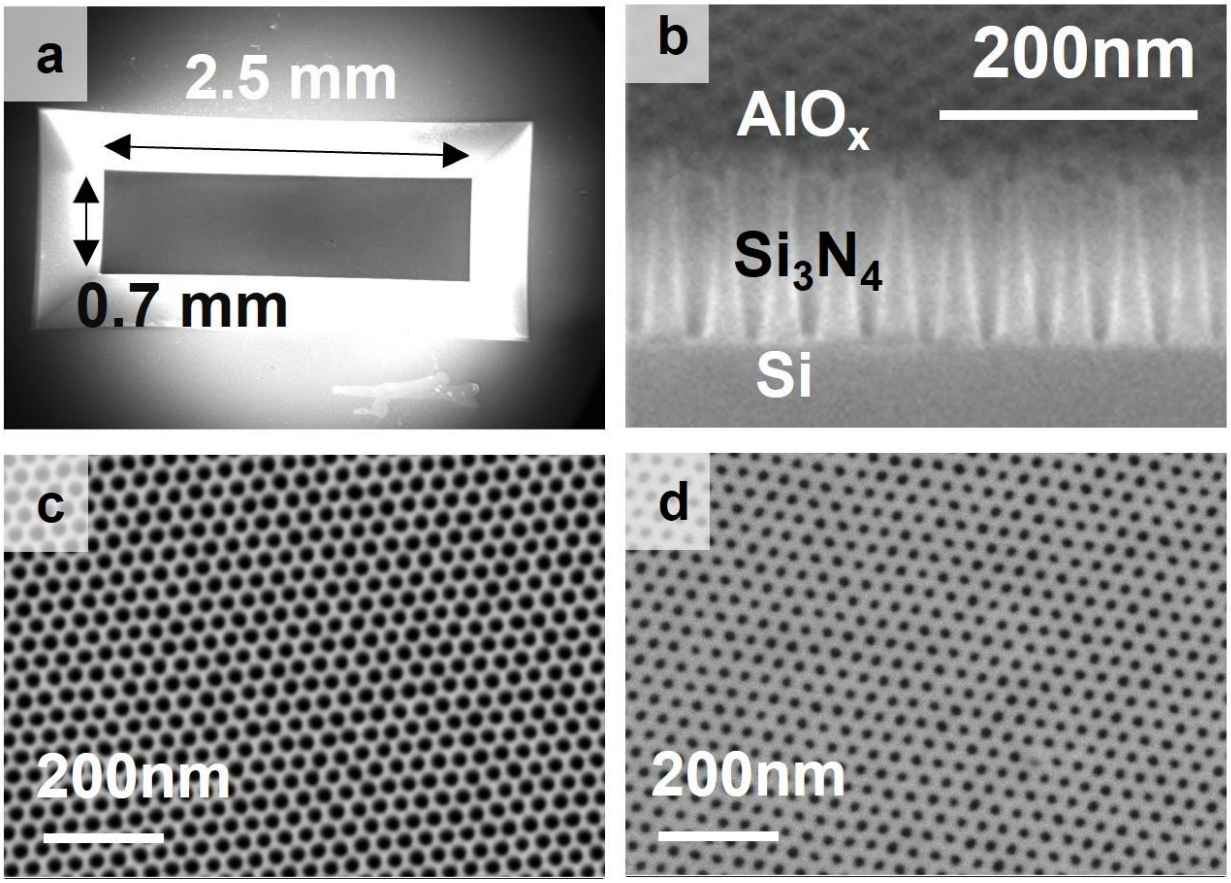

Figure 5.10: SEM images of the Si_3N_4 membrane. (a) Total view, (b) Cross-section view, (c) Front side view, and (d) Back side view.

We precisely shrink the pore size of the Si_3N_4 membranes with ALD and control the surface charge of the nanochannels by choosing different coating materials. Based on the zeta potential profile (Figure 4.22), SiO_2 has the highest negative surface charge compared to other metal oxides grown by ALD. Thus, as with the AAO experiment described previously, we choose SiO_2 as the coating material. The deposition is carried out at 200 °C using (3-aminopropyl)triethoxysilane (APTES), H_2O, and ozone as the precursors. The recipe time sequence (s) (metal precursor dose/purge/co-reactant dose/purge/co-reactant dose/purge) is as follows: 2/15/2/10/10/15. To check the growth rate of SiO_2, we measured thickness on a Si/SiO_2

wafer after deposition, revealing a rate of 0.34 Å/cycle. (The position of wafers and Si_3N_4 membranes is presented in Figure 5.11.)

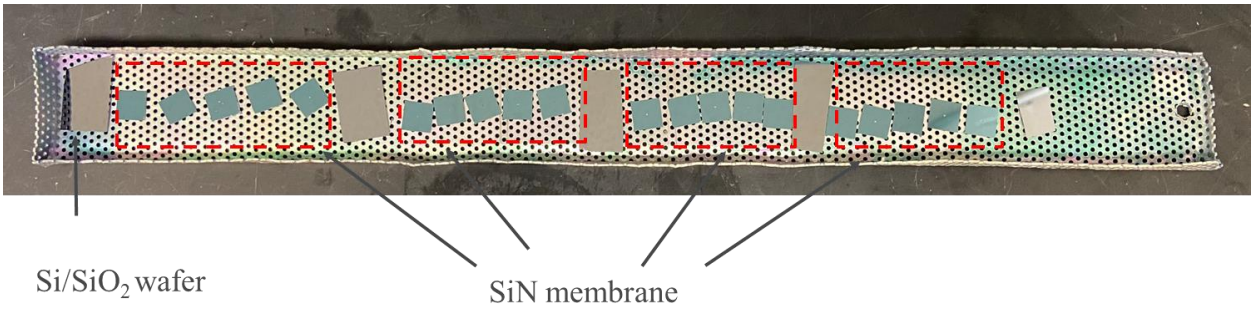

Figure 5.11: Layout of Si_3N_4 membranes and Si wafers.

After SiO_2 coating, the Si_3N_4 pores uniformly shrink down. The back-side pores are shrunk to 16.1 nm and 12.5 nm after 100 cycles and 160 cycles of ALD coating, respectively, from the pristine size of 17.0 nm. The back side pores are shrunk to 21.7 nm and 17.8 nm after 100 cycles and 160 cycles coating, respectively, from the pristine size of 23.5 nm.

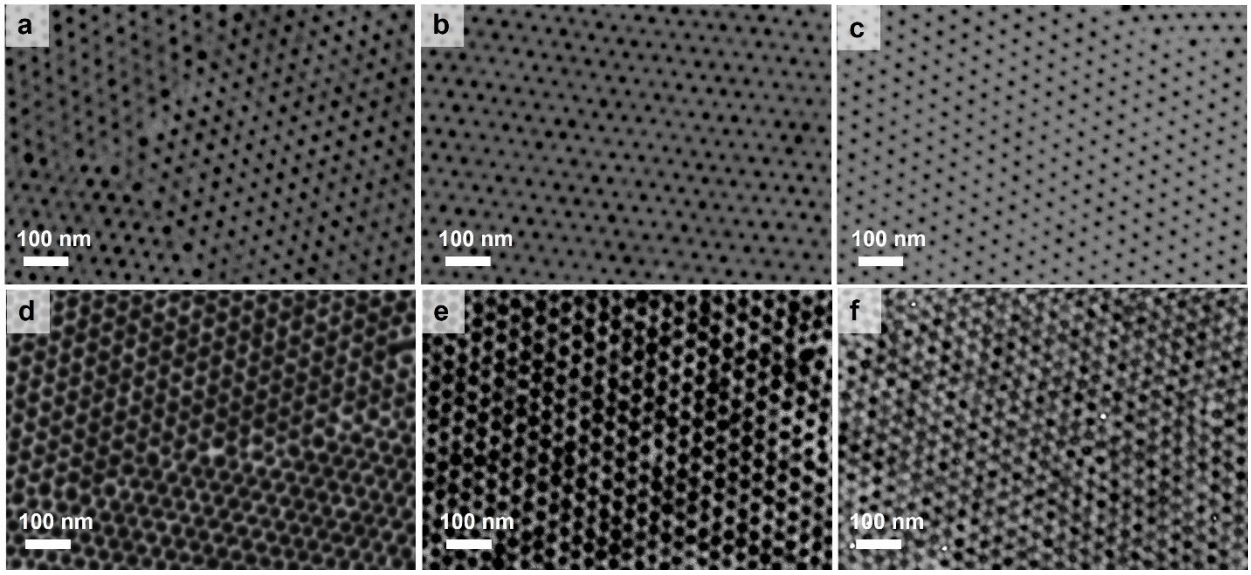

Figure 5.12: SEM images of Si_3N_4 membranes grown with SiO_2 by ALD. (a) Back side of pristine Si_3N_4 membrane, (b) Back side of Si_3N_4 membrane with 100 cycles of SiO_2, (c) Back side of Si_3N_4 membrane with 160 cycles of SiO_2, (d) Front side of pristine Si_3N_4 membrane, (e) Front side of Si_3N_4 membrane with 100 cycles of SiO_2, and (f) Front side of Si_3N_4 membrane with 160 cycles of SiO_2.

5.2.3 Transmembrane Ionic Current through MgO-AAO-SnO_2 Sandwich Structured Membranes

Ion transport is the targeted property to explore in these membranes. Conductivity, ion concentrations in separation processes, rectification ratio, and power density are all of interest. To characterize these properties, an electrochemical workstation is utilized to perform linear sweep voltammetry (LSV). In some cases, inductively coupled plasma mass spectrometry (ICP-MS) is used to detect elements at low concentration in solution.

The ionic transport properties of the ALD-modified AAO membrane were examined with a simple electrochemical device by measuring the transmembrane ionic current. A pair of Ag/AgCl electrodes was used to apply a transmembrane potential. The electrolytes are 0.01 M

KCl, K_2SO_4, and KH_2PO_4. For pristine isotropic AAO membranes, no ionic rectification is observed because of its symmetric nanochannel structure.

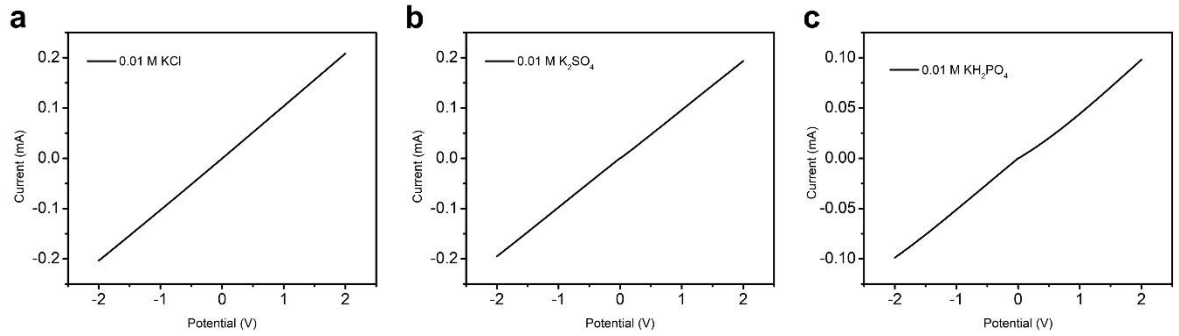

Figure 5.13: Transmembrane ionic current through pristine isotropic AAO membranes.

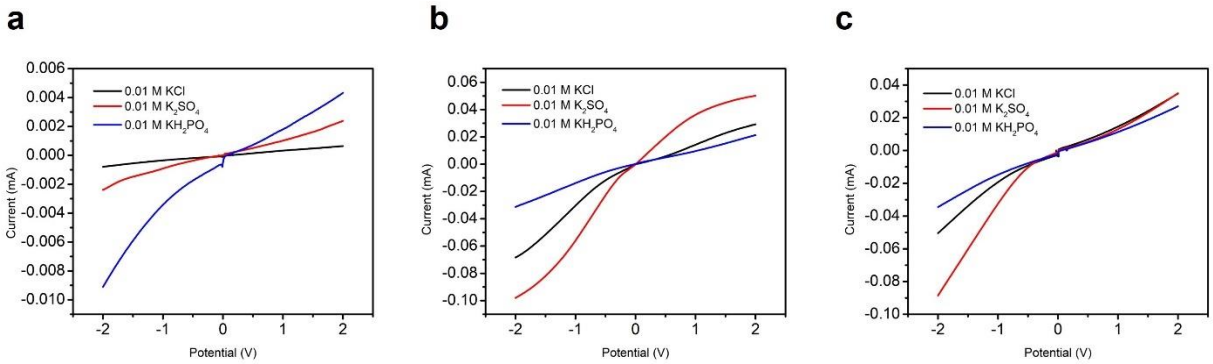

Figure 5.14: Ionic rectification for (a) MgO-AAO-SnO_2 sandwich structured membrane, (b) AAO membrane coated with MgO on one side, and (c) AAO membrane coated with SnO_2 on one side.

As for ALD-modified AAO membranes, they each exhibit ionic rectification because of the asymmetric channel surface charge distribution along the membrane with sandwich structure. We also observe ionic rectification for one-side-coated materials because of the asymmetric channel geometry. The highest rectification ratio was three for SnO_2-coated AAO membranes. Figure 5.14 shows the I-V curve of the heterogeneous membrane sweeping from the potential of –2 V to 2 V. The rectification phenomenon occurring here shows that ALD can be utilized to

fabricate Janus membranes for nanofluidic system. However, the relatively low rectification ratio of the sandwich structured membranes can be attributed primarily to two reasons: (1) MgO has poor stability in aqueous systems, as shown in Figure 4.20. SnO_2 could serve as a positive charged coating material, but SiO_2 would serve as a better counter material that possesses high negative surface charge. (2) The high aspect ratio of the commercial membrane (~2500) makes it difficult to modify the whole channel cross section. Rather, the coating materials are mainly deposited on the outside surface of the membrane and only to a shallow fraction of the overall depth.

5.2.4 Transmembrane Ionic Current through ALD-modified Si_3N_4 Membrane

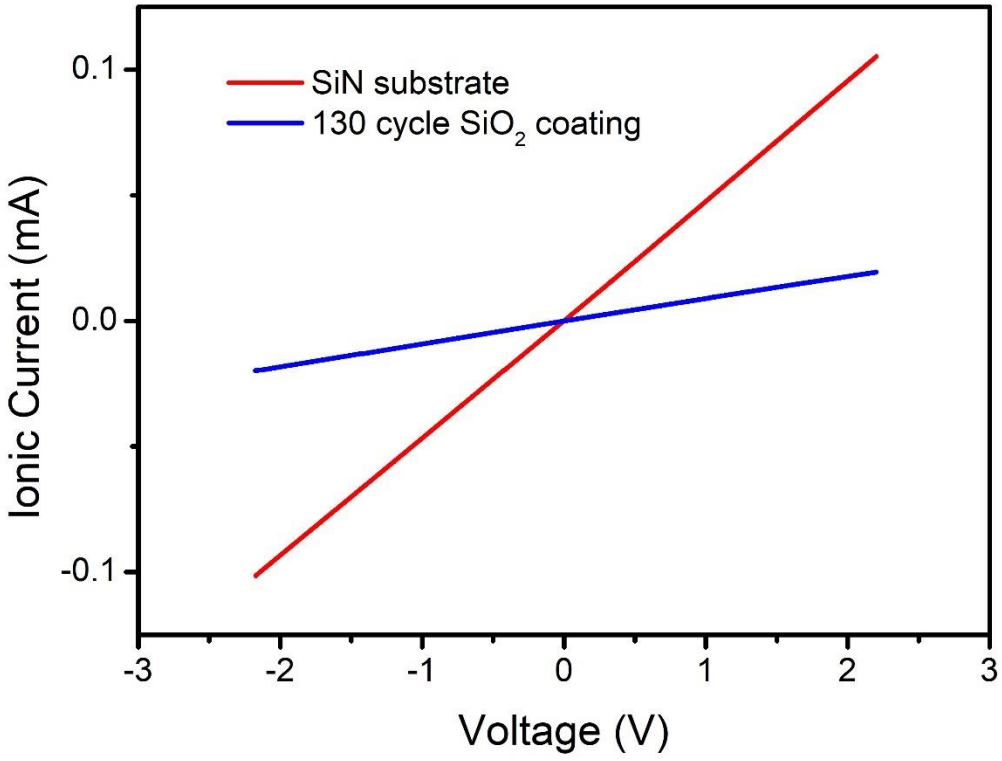

Figure 5.15: Transmembrane ionic current through Si_3N_4 membrane and SiO_2 coated Si_3N_4 membrane.

The ion transport properties of the Si_3N_4 membranes were examined with a simple electrochemical device by measuring the transmembrane ionic current. The electrolyte is 0. 1 M KCl. For Si_3N_4 membrane and SiO_2 coated Si_3N_4, no ionic rectification is observed. Unlike the AAO-based Janus membranes, these membranes have rather low aspect ratio pores (~5:1), so the ALD precursors rapidly diffuse through the entire pore length, even for very short vapor pulses. Because ALD is a conformal coating method, the total channel of the Si_3N_4 membrane is deposited with uniform SiO_2 giving the membrane a symmetric surface charge property. Future studies will pursue combinations of ALD and other deposition methods to selectively coat only part of the pore length with a material bearing opposite charge to the substrate.

5.3 Conclusion

In summary, ALD has been demonstrated as an effective technology for membrane surface modification, especially for pore size and surface charge control. We successfully designed and fabricated MgO-AAO-SnO_2 sandwich structured membranes with Janus structure, which possess ionic rectification property. In ongoing studies within this project, rectification ratio will be enhanced through judicious design of the membrane architecture, guided by simulations. By choosing more suitable metal oxide coatings and tuning the ALD process parameters, AAO membranes are expected to achieve a higher rectification ratio. For the precise isoporous Si_3N_4 system, we have successfully controlled the pore size and introduced strong surface charge. In future studies, we will explore approaches such as in situ molecular grafting onto these substrates or membrane transfer processes to generate a heterostructure, which we

believe could achieve higher rectification ratio. Once these goals are realized, osmotic energy conversion performance can be characterized.

We propose to take advantage of the unique capabilities of ALD technology to this end. Preliminary experiments have led to membranes exhibiting rectification ratios of ~3, demonstrating the promise of this research direction. Detailed characterization of the structure, properties, and function of these membranes will ultimately provide a thorough understanding of ion transport properties, with ramifications extending beyond the applications explored herein.

5.4 Experimental Methods

Zeta Potential Measurements. The same as in the previous chapter.

Electrical Measurements. The ionic transport property of the Janus membranes was studied by measuring the ionic current through the heterogeneous membrane. The ionic current was measured by a SP-150 potentiostat (Biologic). The Janus membrane was mounted in between a two-compartment electrochemical cell. The Ag/AgCl electrodes were used to apply a transmembrane potential.

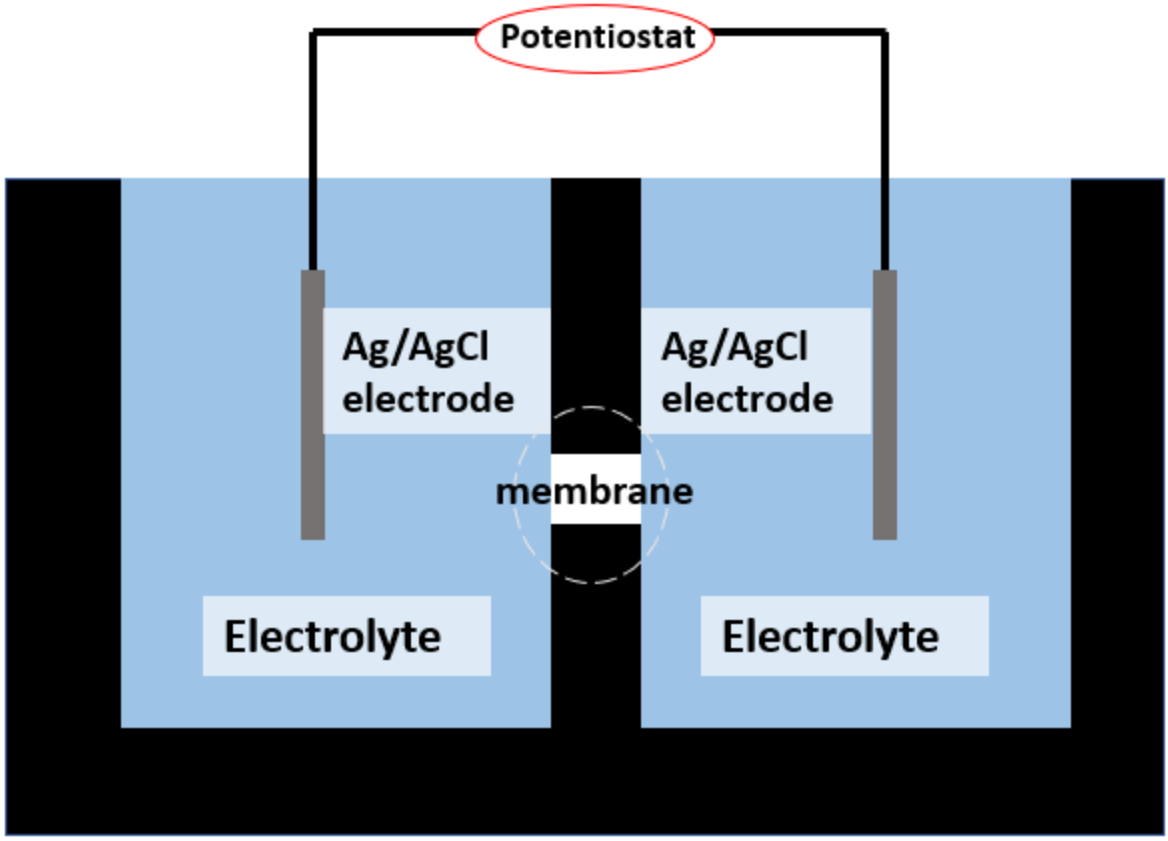

Figure 5.16: Schematic of the electrochemical testing setup

Modeling. Based on the Poisson-Nernst-Planck equations and Kirchhoff's current law, the equilibrium ion transport properties can be explored by numerical simulation. To optimize the Janus membranes' surface charge density distribution and pore sizes, the de Pablo group built models to investigate the parameter space of the transport channel. The most relevant parameters of the channel in Janus membrane that can affect the ion transport properties are channel length L, diameter d, surface charge density σ, applied voltage V, ion charge Q, ionic concentration C, and channel shape. An initial simplified model system was defined as shown in Figure 5.17a.

Here, the charge density is treated as a constant on both sides. Under positive bias (V1 = 2 V, V2 = 0 V) and negative bias (V1 = 0 V, V2 = 2 V), the simulated potential profiles are shown in Figure 5.17b.

The fluidic channels within Janus membranes follow a similar principle to ionic diodes, which is that bipolar nanopores exhibit different ion conductance under different applied bias. The systems break symmetry in its geometry, ionic concentration, and surface charge. Fundamentally, the difference of conductance under different voltages originates from the asymmetric cation/anion distribution on each side of the channel at equilibrium. When an external electric field is applied, the ion current is proportional to the original equilibrium ion concentration. Therefore, under bias polarity, when the outward ionic flow is larger than the inward ionic flow, the nanopore is depleted, leading to lower ionic conduction. When the applied electric field is reversed, it can lead to an accumulation of ions in the pores and results in higher ionic conductivity. This nonlinear ionic conductivity response eventually leads to ionic rectification. The modeling result in Figure 17b compares with recent literature reports[214, 205].

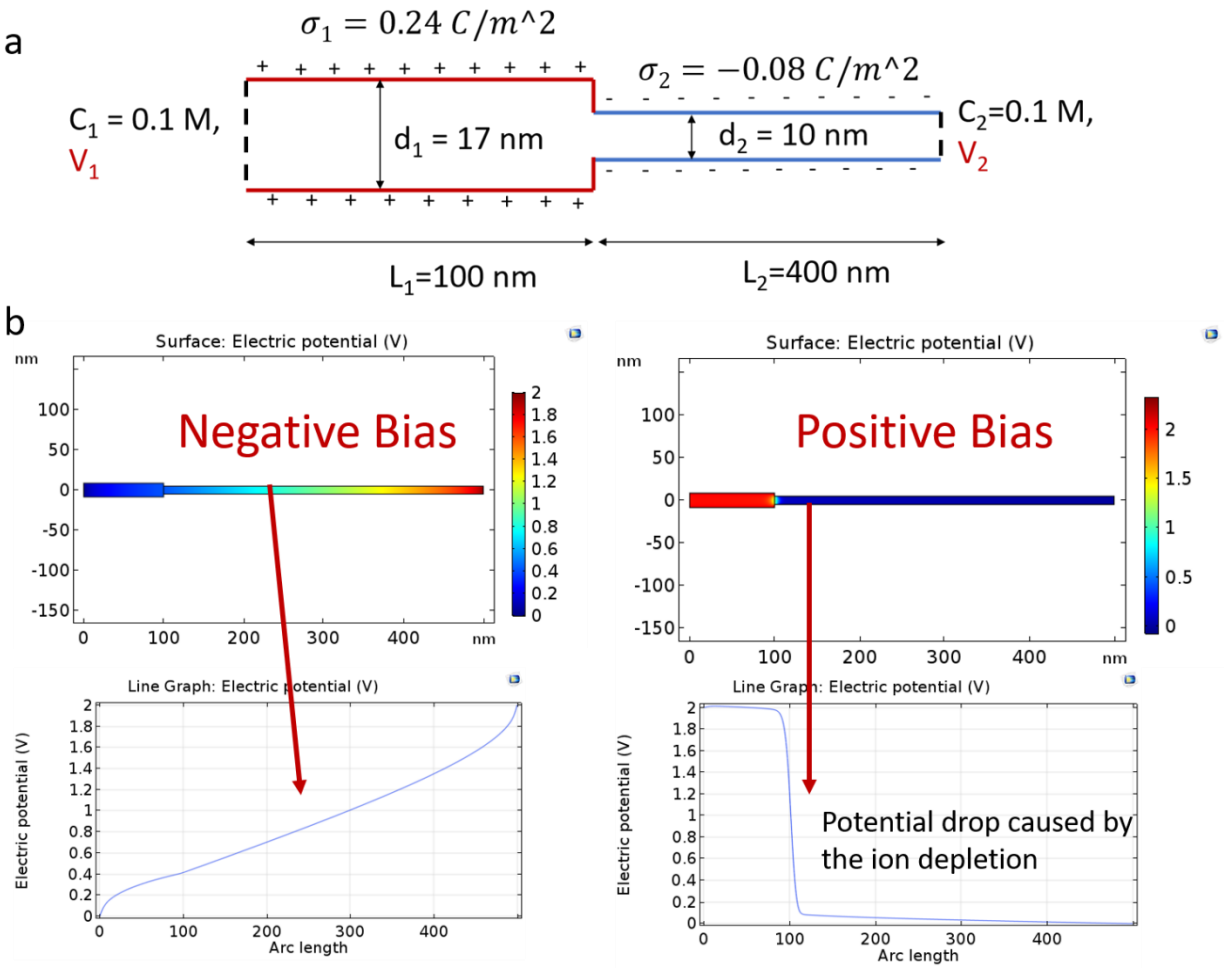

Figure 5.17: (a) Simplified model system of a Janus membrane, (b) Simulated potential field under negative/positive bias

Appendix C

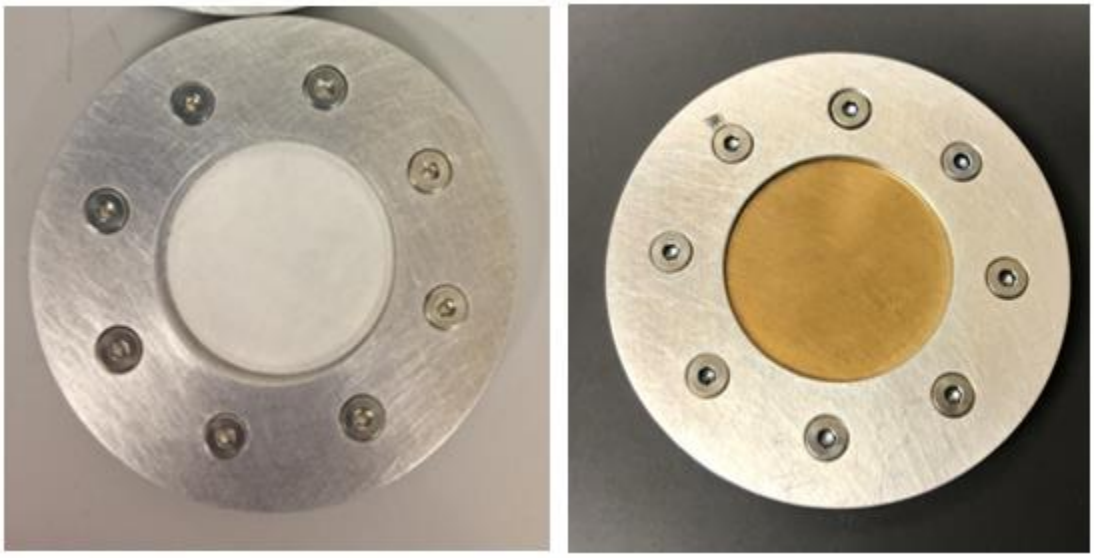

Figure 5.18: Images of assembled ALD holder for one-side deposition: pristine AAO membrane (left) and AAO coated with SnO_2 (right).

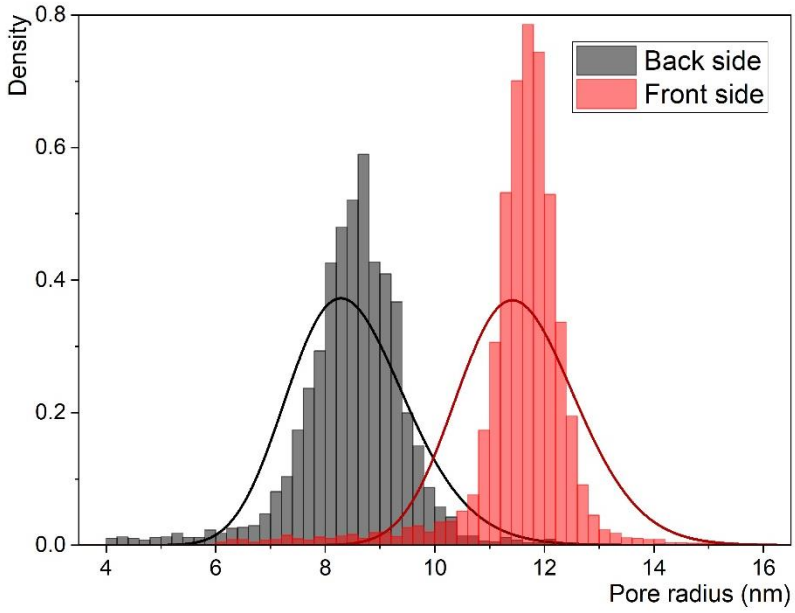

Figure 5.19: Pore size distribution of the front side and back side of the Si_3N_4 membrane.

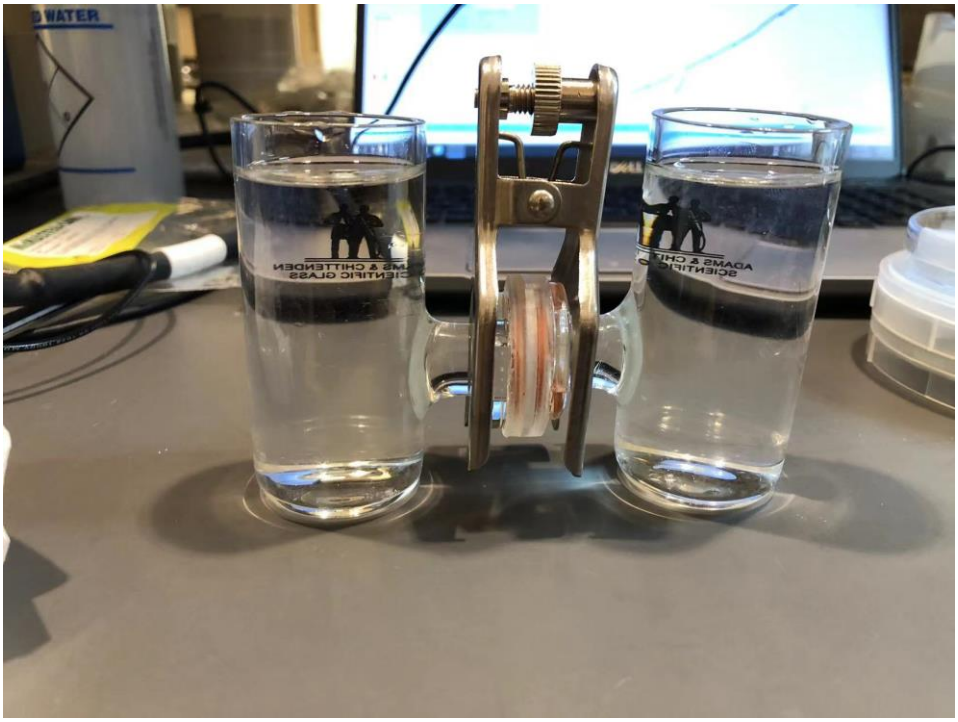

Figure 5.20: H-cell system used for transmembrane ionic current measurement.

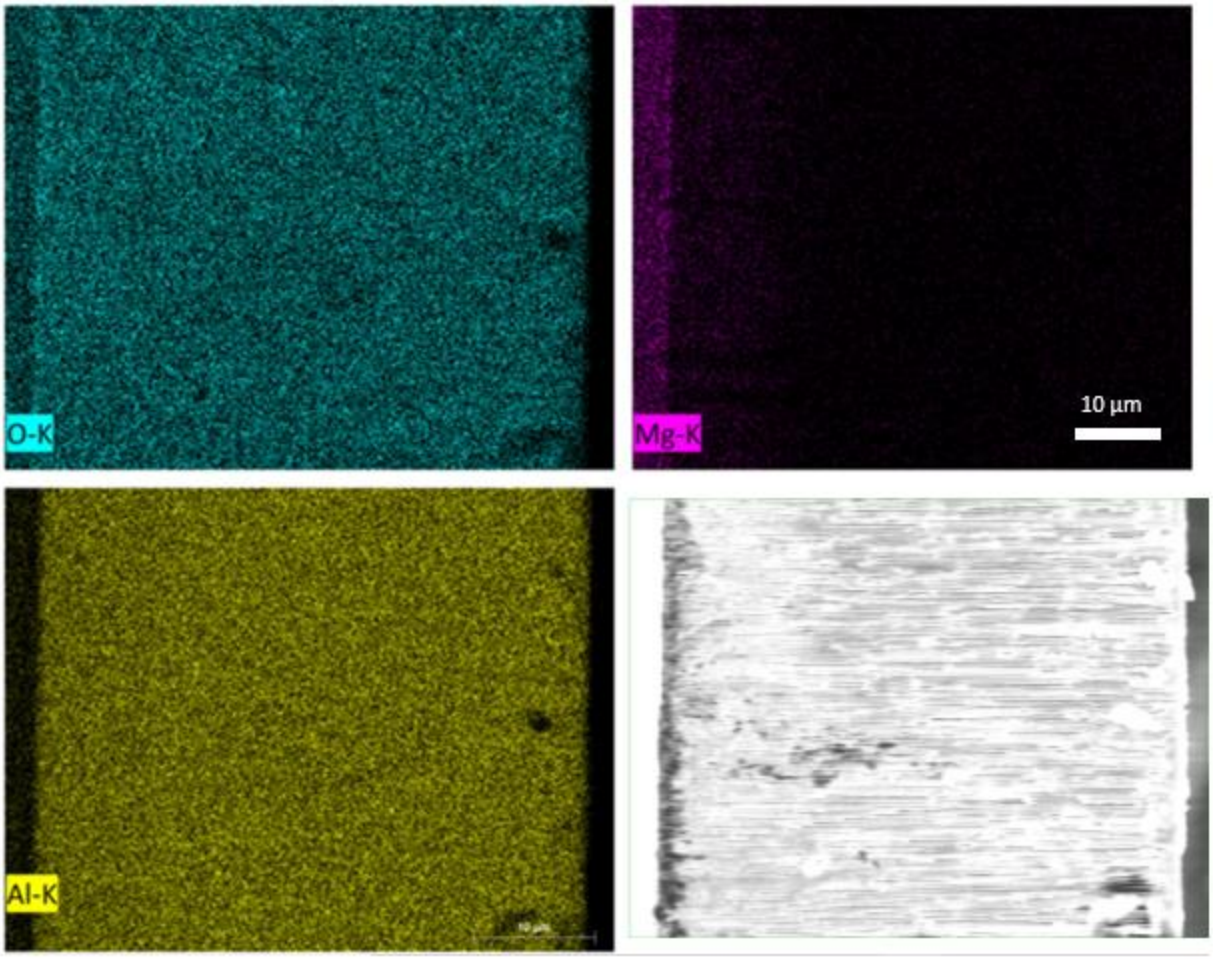

Figure 5.21: EDS elemental mapping and SEM image of the cross-section of MgO-AAO (one side deposition).

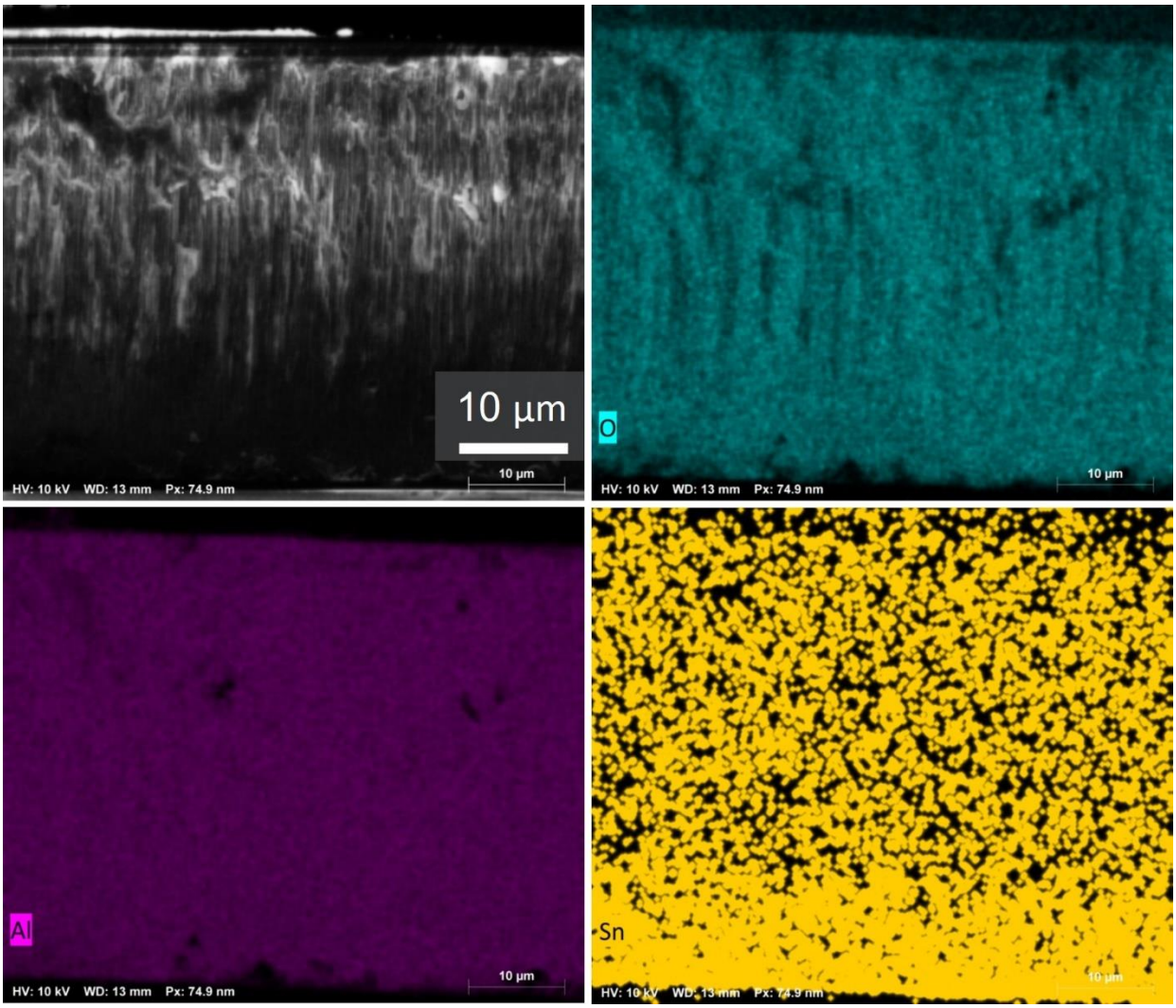

Figure 5.22: EDS elemental mapping and SEM image of the cross-section of SnO_2-AAO (one side deposition).

Chapter 6: CONCLUSION

The research in this dissertation was designed and conducted in the aim of providing new functional materials to solve water-energy nexus challenges by solar steam generation, membrane separation, and osmotic energy conversion.

In Chapter 2, we present a facile process in designing and fabricating the first COF based solar steam generator. Solar steam generation is a promising technology for treatment of saline or wastewater, drawing on plentiful sunlight as a clean and renewable energy source for distillation. In this application, one needs an efficient photothermal material that can harvest a broad range of wavelengths, convert the energy into heat, and transfer that heat to water at an air/water interface for enhanced evaporation. We demonstrated a universal, simple, and scalable interface engineering strategy for the fabrication of a solar steam generator based on this POF material. Wood@POF, using wood as the template, exhibited about 80% overall process efficiency for solar steam generation under 1.6 Suns illumination. This high performance is attributed to both the superior qualities of wood materials as a scaffold material and the exceptional solar absorptivity of POF particles. This method was also demonstrated with other templates, including sponge@POF, fabric@POF, and membrane@POF. They are all promising candidates as solar steam generators, with the selection of material for a specific application guided by availability, cost, and other factors. POF-based interface engineering design provides a pathway for the scalable fabrication of solar steam generators, with potential ramifications for desalination, wastewater treatment, and beyond.

In Chapter 3, we have demonstrated a method for tuning the 2D interlayer galleries of phyllosilicate mineral membranes via judicious selection of different molecular crosslinkers. The water stability (including electrolyte solutions) is enhanced while preserving the general layer

morphology and structure. Control of the nanochannel height enables tuning of both water and ion permeabilities via delicate manipulation of the balance between steric hindrance and electrostatic interaction. In principle, since the ion permeability ratios vary with different interlayer spacings, one could rationally design a particular spacing to promote transport of certain ions while inhibiting others, providing a broad array of applications for such membranes for ion separation, battery separators, wastewater treatment, resource recovery, and beyond. What's more, we are extending the 2D interlayer galleries to muscovite, we have successfully exfoliated this "new" mineral material, and probably be the first group to generate 2D muscovite membranes.

In Chapter 4, we present characterization of a diverse range of ALD-grown metal oxide films. As a world-leading research group focusing on water treatment, our group utilizes ALD as a common technology to do surface modification. However, a comprehensive understanding of the surface charge properties of ALD-grown metal oxides films in aqueous system is missing. We fabricated 16 different ALD-grown films. As a prelude to zeta potential measurement, those films that were sufficiently stable in water were characterized for their wetting properties, which were almost uniformly hydrophilic, with the notable exception of indium oxide. Zeta potential measurements were conducted to investigate the surface charge property for these films. NiO and SiO_2 are promising candidates as ALD coatings with negative surface charge in aqueous solution, whereas ZrO_2, Al_2O_3, and Ga_2O_3 are promising for positive surface charge coatings at near-neutral pH. Collectively, these results represent a comprehensive study of the water stability, wetting properties, and surface charge properties for many common ALD-grown metal oxide films. We believe this work provides a guideline resource for researchers and technologists in selecting ALD materials for a range of water treatment applications.

Chapter 5 follows the work from the previous chapter, we use ALD to generate Janus structure. We successfully designed and fabricated MgO-AAO-SnO_2 sandwich structured membranes with Janus structure, which present certain ionic rectification property. This is still an ongoing project, by choosing more suitable coating metal oxides, and tuning the ALD parameters, like cycle number, diffusion time, et al, AAO membranes could achieve a higher rectification ratio. As for the much more precise substrate, Si_3N_4, we have successfully controlled the pore size and introduced strong surface charge. Moving forward, the comprehensive investigation in ALD parameters and ionic rectification ratios will benefit further experiments design for osmosis energy generator.

During my PhD, I have designed and synthesized several different functional materials for different practical water treatment applications, like the first porphyrin COFs for solar steam generation, the 2D stable vermiculite membranes for selective ion transport, first 2D muscovite membrane and so on. These new findings and achievements could help to broaden the materials candidate for gradually severe water-energy problem.

REFERENCES

(1) Ercin, A. E.; Hoekstra, A. Y. Water Footprint Scenarios for 2050: A Global Analysis. *Environ. Int.* **2014**, *64*, 71–82. https://doi.org/10.1016/j.envint.2013.11.019.

(2) Lee, A.; Elam, J. W.; Darling, S. B. Membrane Materials for Water Purification: Design, Development, and Application. *Environ. Sci. Water Res. Technol.* **2016**, *2* (1), 17–42. https://doi.org/10.1039/c5ew00159e.

(3) Ockwig, N. W.; Co, A. P.; Keeffe, M. O.; Matzger, A. J.; Yaghi, O. M. Porous , Crystalline , Covalent Organic Frameworks. **2005**, *310* (November), 1166–1171.

(4) Huang, N.; Chen, X.; Krishna, R.; Jiang, D. Two-Dimensional Covalent Organic Frameworks for Carbon Dioxide Capture through Channel-Wall Functionalization. *Angew. Chemie* **2015**, *127* (10), 3029–3033. https://doi.org/10.1002/ange.201411262.

(5) Furukawa, H.; Yaghi, O. M. Storage of Hydrogen, Methane, and Carbon Dioxide in Highly Porous Covalent Organic Frameworks for Clean Energy Applications. *J. Am. Chem. Soc.* **2009**, *131* (25), 8875–8883. https://doi.org/10.1021/ja9015765.

(6) Goddard, W. A.; Mendoza-Cortés, J. L.; Han, S. S.; Furukawa, H.; Yaghi, O. M. Adsorption Mechanism and Uptake of Methane in Covalent Organic Frameworks: Theory and Experiment. *J. Phys. Chem. A* **2010**, *114* (40), 10824–10833. https://doi.org/10.1021/jp1044139.

(7) Ding, S. Y.; Gao, J.; Wang, Q.; Zhang, Y.; Song, W. G.; Su, C. Y.; Wang, W. Construction of Covalent Organic Framework for Catalysis: Pd/COF-LZU1 in Suzuki-Miyaura Coupling Reaction. *J. Am. Chem. Soc.* **2011**, *133* (49), 19816–19822. https://doi.org/10.1021/ja206846p.

(8) Fang, Q.; Gu, S.; Zheng, J.; Zhuang, Z.; Qiu, S.; Yan, Y. 3D Microporous Base-Functionalized Covalent Organic Frameworks for Size-Selective Catalysis. *Angew. Chemie* **2014**, *126* (11), 2922–2926. https://doi.org/10.1002/ange.201310500.

(9) Wang, X.; Han, X.; Zhang, J.; Wu, X.; Liu, Y.; Cui, Y. Homochiral 2D Porous Covalent Organic Frameworks for Heterogeneous Asymmetric Catalysis. *J. Am. Chem. Soc.* **2016**, *138* (38), 12332–12335. https://doi.org/10.1021/jacs.6b07714.

(10) Das, G.; Biswal, B. P.; Kandambeth, S.; Venkatesh, V.; Kaur, G.; Addicoat, M.; Heine, T.; Verma, S.; Banerjee, R. Chemical Sensing in Two Dimensional Porous Covalent Organic Nanosheets. *Chem. Sci.* **2015**, *6* (7), 3931–3939. https://doi.org/10.1039/c5sc00512d.

(11) Xu, F.; Xu, H.; Chen, X.; Wu, D.; Wu, Y.; Liu, H.; Gu, C.; Fu, R.; Jiang, D. Radical Covalent Organic Frameworks: A General Strategy to Immobilize Open-Accessible Polyradicals for High-Performance Capacitive Energy Storage. *Angew. Chemie* **2015**, *127* (23), 6918–6922. https://doi.org/10.1002/ange.201501706.

(12) Li, B. Q.; Zhang, S. Y.; Wang, B.; Xia, Z. J.; Tang, C.; Zhang, Q. A Porphyrin Covalent Organic Framework Cathode for Flexible Zn-Air Batteries. *Energy Environ. Sci.* **2018**. https://doi.org/10.1039/c8ee00977e.

(13) Xia, Z.; Zhao, Y.; Darling, S. B. Covalent Organic Frameworks for Water Treatment. *Adv. Mater. Interfaces* **2021**, *8* (1), 1–17. https://doi.org/10.1002/admi.202001507.

(14) Karan, S.; Jiang, Z.; Livingston, A. G. Sub-10 Nm Polyamide Nanofilms with Ultrafast Solvent Transport for Molecular Separation. *Science (80-.).* **2015**, *348* (6241), 1347–1351. https://doi.org/10.1126/science.aaa5058.

(15) Medina, D. D.; Rotter, J. M.; Hu, Y.; Dogru, M.; Werner, V.; Auras, F.; Markiewicz, J. T.; Knochel, P.; Bein, T. Room Temperature Synthesis of Covalent-Organic Framework Films through Vapor-Assisted Conversion. *J. Am. Chem. Soc.* **2015**, *137* (3), 1016–1019. https://doi.org/10.1021/ja510895m.

(16) Bisbey, R. P.; DeBlase, C. R.; Smith, B. J.; Dichtel, W. R. Two-Dimensional Covalent Organic Framework Thin Films Grown in Flow. *J. Am. Chem. Soc.* **2016**, *138* (36), 11433–11436. https://doi.org/10.1021/jacs.6b04669.

(17) Bunck, D. N.; Dichtel, W. R. Bulk Synthesis of Exfoliated Two-Dimensional Polymers Using Hydrazone-Linked Covalent Organic Frameworks. *J. Am. Chem. Soc.* **2013**, *135* (40), 14952–14955. https://doi.org/10.1021/ja408243n.

(18) Chandra, S.; Kandambeth, S.; Biswal, B. P.; Lukose, B.; Kunjir, S. M.; Chaudhary, M.; Babarao, R.; Heine, T.; Banerjee, R. Chemically Stable Multilayered Covalent Organic Nanosheets from Covalent Organic Frameworks via Mechanical Delamination. *J. Am. Chem. Soc.* **2013**, *135* (47), 17853–17861. https://doi.org/10.1021/ja408121p.

(19) Khayum, M. A.; Kandambeth, S.; Mitra, S.; Nair, S. B.; Das, A.; Nagane, S. S.; Mukherjee, R.; Banerjee, R. Chemically Delaminated Free-Standing Ultrathin Covalent Organic Nanosheets. *Angew. Chemie* **2016**, *128* (50), 15833–15837. https://doi.org/10.1002/ange.201607812.

(20) Mitra, S.; Kandambeth, S.; Biswal, B. P.; Abdul Khayum, M.; Choudhury, C. K.; Mehta, M.; Kaur, G.; Banerjee, S.; Prabhune, A.; Verma, S.; Roy, S.; Kharul, U. K.; Banerjee, R. Self-Exfoliated Guanidinium-Based Ionic Covalent Organic Nanosheets (ICONs). *J. Am. Chem. Soc.* **2016**, *138* (8), 2823–2828. https://doi.org/10.1021/jacs.5b13533.

(21) Ding, S. Y.; Wang, W. Covalent Organic Frameworks (COFs): From Design to Applications. *Chem. Soc. Rev.* **2013**, *42* (2), 548–568. https://doi.org/10.1039/c2cs35072f.

(22) Wang, H.; Zeng, Z.; Xu, P.; Li, L.; Zeng, G.; Xiao, R.; Tang, Z.; Huang, D.; Tang, L.; Lai, C.; Jiang, D.; Liu, Y.; Yi, H.; Qin, L.; Ye, S.; Ren, X.; Tang, W. Recent Progress in Covalent Organic Framework Thin Films: Fabrications, Applications and Perspectives. *Chem. Soc. Rev.* **2019**, *48* (2), 488–516. https://doi.org/10.1039/c8cs00376a.

(23) Wang, Z.; Zhang, S.; Chen, Y.; Zhang, Z.; Ma, S. Covalent Organic Frameworks for Separation Applications. *Chem. Soc. Rev.* **2020**, *49* (3), 708–735.

https://doi.org/10.1039/c9cs00827f.

(24) Doonan, C. J.; Tranchemontagne, D. J.; Glover, T. G.; Hunt, J. R.; Yaghi, O. M. Exceptional Ammonia Uptake by a Covalent Organic Framework. *Nat. Chem.* **2010**, *2* (3), 235–238. https://doi.org/10.1038/nchem.548.

(25) Wan, S.; Guo, J.; Kim, J.; Ihee, H.; Jiang, D. A Belt-Shaped, Blue Luminescent, and Semiconducting Covalent Organic Framework. *Angew. Chemie - Int. Ed.* **2008**, *47* (46), 8826–8830. https://doi.org/10.1002/anie.200803826.

(26) Wen, R.; Li, Y.; Zhang, M.; Guo, X.; Li, X.; Li, X.; Han, J.; Hu, S.; Tan, W.; Ma, L.; Li, S. Graphene-Synergized 2D Covalent Organic Framework for Adsorption: A Mutual Promotion Strategy to Achieve Stabilization and Functionalization Simultaneously. *J. Hazard. Mater.* **2018**, *358* (29), 273–285. https://doi.org/10.1016/j.jhazmat.2018.06.059.

(27) Gao, M.; Zhu, L.; Peh, C. K.; Ho, G. W. Solar Absorber Material and System Designs for Photothermal Water Vaporization towards Clean Water and Energy Production. *Energy Environ. Sci.* **2019**, *12* (3), 841–864. https://doi.org/10.1039/c8ee01146j.

(28) Zhou, J.; Gu, Y.; Liu, P.; Wang, P.; Miao, L.; Liu, J.; Wei, A.; Mu, X.; Li, J.; Zhu, J. Development and Evolution of the System Structure for Highly Efficient Solar Steam Generation from Zero to Three Dimensions. *Adv. Funct. Mater.* **2019**, *29* (50), 1903255. https://doi.org/10.1002/adfm.201903255.

(29) Zhao, F.; Guo, Y.; Zhou, X.; Shi, W.; Yu, G. Materials for Solar-Powered Water Evaporation. *Nat. Rev. Mater.* **2020**, *5* (May), 388–401. https://doi.org/10.1038/s41578-020-0182-4.

(30) Wu, S. L.; Chen, H.; Wang, H. L.; Chen, X.; Yang, H. C.; Darling, S. B. Solar-Driven Evaporators for Water Treatment: Challenges and Opportunities. *Environ. Sci. Water Res. Technol.* **2021**, *7* (1), 24–39. https://doi.org/10.1039/d0ew00725k.

(31) Darling, S. B. Perspective: Interfacial Materials at the Interface of Energy and Water. *J. Appl. Phys.* **2018**, *124* (3), 030901. https://doi.org/10.1063/1.5040110.

(32) Liu, G.; Jin, W.; Xu, N. Two-Dimensional-Material Membranes: A New Family of High-Performance Separation Membranes. *Angew. Chemie - Int. Ed.* **2016**, *55* (43), 13384–13397. https://doi.org/10.1002/anie.201600438.

(33) Rodenas, T.; Luz, I.; Prieto, G.; Seoane, B.; Miro, H.; Corma, A.; Kapteijn, F.; Llabrés I Xamena, F. X.; Gascon, J. Metal-Organic Framework Nanosheets in Polymer Composite Materials for Gas Separation. *Nat. Mater.* **2015**, *14* (1), 48–55. https://doi.org/10.1038/nmat4113.

(34) Cheetham, A. K.; Rao, C. N. R.; Feller, R. K. Structural Diversity and Chemical Trends in Hybrid Inorganic-Organic Framework Materials. *Chem. Commun.* **2006**, No. 46, 4780–4795. https://doi.org/10.1039/b610264f.

(35) Pham, T. C. T.; Nguyen, T. H.; Yoon, K. B. Gel-Free Secondary Growth of Uniformly Oriented Silica MFI Zeolite Films and Application for Xylene Separation. *Angew. Chemie*

- *Int. Ed.* **2013**, *52* (33), 8693–8698. https://doi.org/10.1002/anie.201301766.

(36) Jeong, H. K.; Nair, S.; Vogt, T.; Charles Dickinson, L.; Tsapatsis, M. A Highly Crystalline Layered Silicate with Three-Dimensionally Microporous Layers. *Nat. Mater.* **2003**, *2* (1), 53–58. https://doi.org/10.1038/nmat795.

(37) Mi, B. Graphene Oxide Membranes for Ionic and Molecular Sieving. *Science (80-.).* **2014**, *343* (6172), 740–742. https://doi.org/10.1126/science.1250247.

(38) O'Hern, S. C.; Jang, D.; Bose, S.; Idrobo, J. C.; Song, Y.; Laoui, T.; Kong, J.; Karnik, R. Nanofiltration across Defect-Sealed Nanoporous Monolayer Graphene. *Nano Lett.* **2015**, *15* (5), 3254–3260. https://doi.org/10.1021/acs.nanolett.5b00456.

(39) Surwade, S. P.; Smirnov, S. N.; Vlassiouk, I. V.; Unocic, R. R.; Veith, G. M.; Dai, S.; Mahurin, S. M. Water Desalination Using Nanoporous Single-Layer Graphene. *Nat. Nanotechnol.* **2015**, *10* (5), 459–464. https://doi.org/10.1038/nnano.2015.37.

(40) Tsapatsis, M. 2-dimensional Zeolites. *AIChE J.* **2012**, *59* (4), 215–228. https://doi.org/10.1002/aic.

(41) Sun, P.; Zhu, M.; Wang, K.; Zhong, M.; Wei, J.; Wu, D.; Xu, Z.; Zhu, H. Selective Ion Penetration of Graphene Oxide Membranes. *ACS Nano* **2013**, *7* (1), 428–437. https://doi.org/10.1021/nn304471w.

(42) Sun, L.; Huang, H.; Peng, X. Laminar MoS2 Membranes for Molecule Separation. *Chem. Commun.* **2013**, *49* (91), 10718–10720. https://doi.org/10.1039/c3cc46136j.

(43) Sun, L.; Ying, Y.; Huang, H.; Song, Z.; Mao, Y.; Xu, Z.; Peng, X. Ultrafast Molecule Separation through Layered WS2 Nanosheet Membranes. *ACS Nano* **2014**, *8* (6), 6304–6311. https://doi.org/10.1021/nn501786m.

(44) Liu, Y.; Wang, N.; Cao, Z.; Caro, J. Molecular Sieving through Interlayer Galleries. *J. Mater. Chem. A* **2014**, *2* (5), 1235–1238. https://doi.org/10.1039/c3ta13792a.

(45) Liu, Y.; Wang, N.; Caro, J. In Situ Formation of LDH Membranes of Different Microstructures with Molecular Sieve Gas Selectivity. *J. Mater. Chem. A* **2014**, *2* (16), 5716–5723. https://doi.org/10.1039/c4ta00108g.

(46) Ren, C. E.; Hatzell, K. B.; Alhabeb, M.; Ling, Z.; Mahmoud, K. A.; Gogotsi, Y. Charge- and Size-Selective Ion Sieving Through Ti3C2Tx MXene Membranes. *J. Phys. Chem. Lett.* **2015**, *6* (20), 4026–4031. https://doi.org/10.1021/acs.jpclett.5b01895.

(47) Sethurajaperumal, A.; Ravichandran, V.; Banerjee, A.; Manohar, A.; Varrla, E. *Two-Dimensional Layered Nanosheets*; Elsevier Inc., 2021. https://doi.org/10.1016/B978-0-12-822352-9.00022-5.

(48) Cho, I.; Lee, K. -W. Morphology of Latex Particles Formed by Poly(Methyl Methacrylate)-seeded Emulsion Polymerization of Styrene. *J. Appl. Polym. Sci.* **1985**, *30* (5), 1903–1926. https://doi.org/10.1002/app.1985.070300510.

(49) de Gennes, P. -G. Soft Matter (Nobel Lecture). *Angew. Chemie Int. Ed. English* **1992**, *31* (7), 842–845. https://doi.org/10.1002/anie.199208421.

(50) Yang, H. C.; Hou, J.; Chen, V.; Xu, Z. K. Janus Membranes: Exploring Duality for Advanced Separation. *Angew. Chemie - Int. Ed.* **2016**, *55* (43), 13398–13407. https://doi.org/10.1002/anie.201601589.

(51) Zhao, Y.; Wang, H.; Zhou, H.; Lin, T. Directional Fluid Transport in Thin Porous Materials and Its Functional Applications. *Small* **2017**, *13* (4). https://doi.org/10.1002/smll.201601070.

(52) Yang, H. C.; Xie, Y.; Hou, J.; Cheetham, A. K.; Chen, V.; Darling, S. B. Janus Membranes: Creating Asymmetry for Energy Efficiency. *Adv. Mater.* **2018**, *30* (43), 1–11. https://doi.org/10.1002/adma.201801495.

(53) Yan, L.; Yang, X.; Zhang, Y.; Wu, Y.; Cheng, Z.; Darling, S. B.; Shao, L. Porous Janus Materials with Unique Asymmetries and Functionality. *Mater. Today* **2021**, *51* (December), 626–647. https://doi.org/10.1016/j.mattod.2021.07.001.

(54) Wu, J.; Wang, N.; Wang, L.; Dong, H.; Zhao, Y.; Jiang, L. Unidirectional Water-Penetration Composite Fibrous Film via Electrospinning. *Soft Matter* **2012**, *8* (22), 5996–5999. https://doi.org/10.1039/c2sm25514f.

(55) Hu, L.; Gao, S.; Zhu, Y.; Zhang, F.; Jiang, L.; Jin, J. An Ultrathin Bilayer Membrane with Asymmetric Wettability for Pressure Responsive Oil/Water Emulsion Separation. *J. Mater. Chem. A* **2015**, *3* (46), 23477–23482. https://doi.org/10.1039/c5ta03975d.

(56) Chen, J.; Liu, Y.; Guo, D.; Cao, M.; Jiang, L. Under-Water Unidirectional Air Penetration via a Janus Mesh. *Chem. Commun.* **2015**, *51* (59), 11872–11875. https://doi.org/10.1039/c5cc03804a.

(57) Wang, Z.; Wang, Y.; Liu, G. Rapid and Efficient Separation of Oil from Oil-in-Water Emulsions Using a Janus Cotton Fabric. *Angew. Chemie - Int. Ed.* **2016**, *55* (4), 1291–1294. https://doi.org/10.1002/anie.201507451.

(58) Tian, X.; Jin, H.; Sainio, J.; Ras, R. H. A.; Ikkala, O. Droplet and Fluid Gating by Biomimetic Janus Membranes. *Adv. Funct. Mater.* **2014**, *24* (38), 6023–6028. https://doi.org/10.1002/adfm.201400714.

(59) Liu, Y.; Xin, J. H.; Choi, C. H. Cotton Fabrics with Single-Faced Superhydrophobicity. *Langmuir* **2012**, *28* (50), 17426–17434. https://doi.org/10.1021/la303714h.

(60) Yang, H. C.; Hou, J.; Wan, L. S.; Chen, V.; Xu, Z. K. Janus Membranes with Asymmetric Wettability for Fine Bubble Aeration. *Adv. Mater. Interfaces* **2016**, *3* (9), 1–5. https://doi.org/10.1002/admi.201500774.

(61) Gu, J.; Xiao, P.; Chen, J.; Zhang, J.; Huang, Y.; Chen, T. Janus Polymer/Carbon Nanotube Hybrid Membranes for Oil/Water Separation. *ACS Appl. Mater. Interfaces* **2014**, *6* (18), 16204–16209. https://doi.org/10.1021/am504326m.

(62) Yang, X.; Martinson, A. B. F.; Elam, J. W.; Shao, L.; Darling, S. B. Water Treatment Based on Atomically Engineered Materials: Atomic Layer Deposition and Beyond. *Matter* **2021**, *4* (11), 3515–3548. https://doi.org/10.1016/j.matt.2021.09.005.

(63) Yang, H. C.; Waldman, R. Z.; Chen, Z.; Darling, S. B. Atomic Layer Deposition for Membrane Interface Engineering. *Nanoscale* **2018**, *10* (44), 20505–20513. https://doi.org/10.1039/c8nr08114j.

(64) Peng, Q.; Tseng, Y. C.; Darling, S. B.; Elam, J. W. Nanoscopic Patterned Materials with Tunable Dimensions via Atomic Layer Deposition on Block Copolymers. *Adv. Mater.* **2010**, *22* (45), 5129–5133. https://doi.org/10.1002/adma.201002465.

(65) George, S. M. Atomic Layer Deposition: An Overview. *Chem. Rev.* **2010**, *110* (1), 111–131. https://doi.org/10.1021/cr900056b.

(66) Mekonnen, M. M.; Hoekstra, A. Y. Sustainability: Four Billion People Facing Severe Water Scarcity. *Sci. Adv.* **2016**, *2* (2), 1–7. https://doi.org/10.1126/sciadv.1500323.

(67) Ercin, A. E.; Hoekstra, A. Y. European Water Footprint Scenarios for 2050. *Water (Switzerland)* **2016**, *8* (6), 1–14. https://doi.org/10.3390/w8060226.

(68) Postel, S. L.; Daily, G. C.; Ehrlich, P. R. Human Appropriation of Renewable Fresh Water. *Science (80-.).* **1996**, *271* (5250), 785–788. https://doi.org/10.1126/science.271.5250.785.

(69) Van der Bruggen, B.; Vandecasteele, C. Distillation vs. Membrane Filtration: Overview of Process Evolutions in Seawater Desalination. *Desalination* **2002**, *143* (3), 207–218. https://doi.org/10.1016/S0011-9164(02)00259-X.

(70) Ziolkowska, J. R. Desalination Leaders in the Global Market – Current Trends and Future Perspectives. *Water Supply* **2016**, *16* (3), 563–578. https://doi.org/10.2166/ws.2015.184.

(71) Chiavazzo, E.; Morciano, M.; Viglino, F.; Fasano, M.; Asinari, P. Passive Solar High-Yield Seawater Desalination by Modular and Low-Cost Distillation. *Nat. Sustain.* **2018**, *1* (12), 763–772. https://doi.org/10.1038/s41893-018-0186-x.

(72) Chen, C.; Li, Y.; Song, J.; Yang, Z.; Kuang, Y.; Hitz, E.; Jia, C.; Gong, A.; Jiang, F.; Zhu, J. Y.; Yang, B.; Xie, J.; Hu, L. Highly Flexible and Efficient Solar Steam Generation Device. *Adv. Mater.* **2017**, *29* (30), 1–8. https://doi.org/10.1002/adma.201701756.

(73) Xu, N.; Hu, X.; Xu, W.; Li, X.; Zhou, L.; Zhu, S.; Zhu, J. Mushrooms as Efficient Solar Steam-Generation Devices. *Adv. Mater.* **2017**, *29* (28), 1606762. https://doi.org/10.1002/adma.201606762.

(74) Li, Y.; Gao, T.; Yang, Z.; Chen, C.; Luo, W.; Song, J.; Hitz, E.; Jia, C.; Zhou, Y.; Liu, B.; Yang, B.; Hu, L. 3D-Printed, All-in-One Evaporator for High-Efficiency Solar Steam Generation under 1 Sun Illumination. *Adv. Mater.* **2017**, *29* (26), 1–8. https://doi.org/10.1002/adma.201700981.

(75) Liu, Y.; Chen, J.; Guo, D.; Cao, M.; Jiang, L. Floatable, Self-Cleaning, and Carbon-Black-

Based Superhydrophobic Gauze for the Solar Evaporation Enhancement at the Air-Water Interface. *ACS Appl. Mater. Interfaces* **2015**, *7* (24), 13645–13652. https://doi.org/10.1021/acsami.5b03435.

(76) Wang, Y.; Zhang, L.; Wang, P. Self-Floating Carbon Nanotube Membrane on Macroporous Silica Substrate for Highly Efficient Solar-Driven Interfacial Water Evaporation. *ACS Sustain. Chem. Eng.* **2016**, *4* (3), 1223–1230. https://doi.org/10.1021/acssuschemeng.5b01274.

(77) Ren, H.; Tang, M.; Guan, B.; Wang, K.; Yang, J.; Wang, F.; Wang, M.; Shan, J.; Chen, Z.; Wei, D.; Peng, H.; Liu, Z. Hierarchical Graphene Foam for Efficient Omnidirectional Solar–Thermal Energy Conversion. *Adv. Mater.* **2017**, *29* (38), 1–7. https://doi.org/10.1002/adma.201702590.

(78) Gao, X.; Ren, H.; Zhou, J.; Du, R.; Yin, C.; Liu, R.; Peng, H.; Tong, L.; Liu, Z.; Zhang, J. Synthesis of Hierarchical Graphdiyne-Based Architecture for Efficient Solar Steam Generation. *Chem. Mater.* **2017**, *29* (14), 5777–5781. https://doi.org/10.1021/acs.chemmater.7b01838.

(79) Xu, W.; Hu, X.; Zhuang, S.; Wang, Y.; Li, X.; Zhou, L.; Zhu, S.; Zhu, J. Flexible and Salt Resistant Janus Absorbers by Electrospinning for Stable and Efficient Solar Desalination. *Adv. Energy Mater.* **2018**, *8* (14). https://doi.org/10.1002/aenm.201702884.

(80) Bae, K.; Kang, G.; Cho, S. K.; Park, W.; Kim, K.; Padilla, W. J. Flexible Thin-Film Black Gold Membranes with Ultrabroadband Plasmonic Nanofocusing for Efficient Solar Vapour Generation. *Nat. Commun.* **2015**, *6*. https://doi.org/10.1038/ncomms10103.

(81) Zhu, M.; Li, Y.; Chen, F.; Zhu, X.; Dai, J.; Li, Y.; Yang, Z.; Yan, X.; Song, J.; Wang, Y.; Hitz, E.; Luo, W.; Lu, M.; Yang, B.; Hu, L. Plasmonic Wood for High-Efficiency Solar Steam Generation. *Adv. Energy Mater.* **2018**, *8* (4). https://doi.org/10.1002/aenm.201701028.

(82) Li, R.; Zhang, L.; Shi, L.; Wang, P. MXene Ti3C2: An Effective 2D Light-to-Heat Conversion Material. *ACS Nano* **2017**, *11* (4), 3752–3759. https://doi.org/10.1021/acsnano.6b08415.

(83) Zhu, G.; Xu, J.; Zhao, W.; Huang, F. Constructing Black Titania with Unique Nanocage Structure for Solar Desalination. *ACS Appl. Mater. Interfaces* **2016**, *8* (46), 31716–31721. https://doi.org/10.1021/acsami.6b11466.

(84) Zeng, Y.; Yao, J.; Horri, B. A.; Wang, K.; Wu, Y.; Li, D.; Wang, H. Solar Evaporation Enhancement Using Floating Light-Absorbing Magnetic Particles. *Energy Environ. Sci.* **2011**, *4* (10), 4074–4078. https://doi.org/10.1039/c1ee01532j.

(85) Ni, G.; Miljkovic, N.; Ghasemi, H.; Huang, X.; Boriskina, S. V.; Lin, C. Te; Wang, J.; Xu, Y.; Rahman, M. M.; Zhang, T. J.; Chen, G. Volumetric Solar Heating of Nanofluids for Direct Vapor Generation. *Nano Energy* **2015**, *17*, 290–301. https://doi.org/10.1016/j.nanoen.2015.08.021.

(86) Jiang, F.; Li, T.; Li, Y.; Zhang, Y.; Gong, A.; Dai, J.; Hitz, E.; Luo, W.; Hu, L. Wood-Based Nanotechnologies toward Sustainability. *Adv. Mater.* **2018**, *30* (1), 1–39. https://doi.org/10.1002/adma.201703453.

(87) Jia, C.; Li, Y.; Yang, Z.; Chen, G.; Yao, Y.; Jiang, F.; Kuang, Y.; Pastel, G.; Xie, H.; Yang, B.; Das, S.; Hu, L. Rich Mesostructures Derived from Natural Woods for Solar Steam Generation. *Joule* **2017**, *1* (3), 588–599. https://doi.org/10.1016/j.joule.2017.09.011.

(88) Yang, H. C.; Chen, Z.; Xie, Y.; Wang, J.; Elam, J. W.; Li, W.; Darling, S. B. Chinese Ink: A Powerful Photothermal Material for Solar Steam Generation. *Adv. Mater. Interfaces* **2019**, *6* (1), 1–7. https://doi.org/10.1002/admi.201801252.

(89) Yang, X.; Yang, Y.; Fu, L.; Zou, M.; Li, Z.; Cao, A.; Yuan, Q. An Ultrathin Flexible 2D Membrane Based on Single-Walled Nanotube–MoS2 Hybrid Film for High-Performance Solar Steam Generation. *Adv. Funct. Mater.* **2018**, *28* (3), 1–9. https://doi.org/10.1002/adfm.201704505.

(90) Yang, Y.; Yang, X.; Fu, L.; Zou, M.; Cao, A.; Du, Y.; Yuan, Q.; Yan, C. H. Two-Dimensional Flexible Bilayer Janus Membrane for Advanced Photothermal Water Desalination. *ACS Energy Lett.* **2018**, *3* (5), 1165–1171. https://doi.org/10.1021/acsenergylett.8b00433.

(91) Dawson, R.; Stöckel, E.; Holst, J. R.; Adams, D. J.; Cooper, A. I. Microporous Organic Polymers for Carbon Dioxide Capture. *Energy Environ. Sci.* **2011**, *4* (10), 4239–4245. https://doi.org/10.1039/c1ee01971f.

(92) Li, Z.; Feng, X.; Zou, Y.; Zhang, Y.; Xia, H.; Liu, X.; Mu, Y. A 2D Azine-Linked Covalent Organic Framework for Gas Storage Applications. *Chem. Commun.* **2014**, *50* (89), 13825–13828. https://doi.org/10.1039/c4cc05665e.

(93) Nandi, S.; Singh, S. K.; Mullangi, D.; Illathvalappil, R.; George, L.; Vinod, C. P.; Kurungot, S.; Vaidhyanathan, R. Low Band Gap Benzimidazole COF Supported Ni3N as Highly Active OER Catalyst. *Adv. Energy Mater.* **2016**, *6* (24). https://doi.org/10.1002/aenm.201601189.

(94) Diercks, C. S.; Liu, Y.; Cordova, K. E.; Yaghi, O. M. The Role of Reticular Chemistry in the Design of CO2 Reduction Catalysts. *Nat. Mater.* **2018**, *17* (4), 301–307. https://doi.org/10.1038/s41563-018-0033-5.

(95) Li, B. Q.; Zhang, S. Y.; Wang, B.; Xia, Z. J.; Tang, C.; Zhang, Q. A Porphyrin Covalent Organic Framework Cathode for Flexible Zn-Air Batteries. *Energy Environ. Sci.* **2018**, *11* (7), 1723–1729. https://doi.org/10.1039/c8ee00977e.

(96) Kong, L.; Li, B. Q.; Peng, H. J.; Zhang, R.; Xie, J.; Huang, J. Q.; Zhang, Q. Porphyrin-Derived Graphene-Based Nanosheets Enabling Strong Polysulfide Chemisorption and Rapid Kinetics in Lithium–Sulfur Batteries. *Adv. Energy Mater.* **2018**, *8* (20). https://doi.org/10.1002/aenm.201800849.

(97) Li, B. Q.; Zhang, S. Y.; Kong, L.; Peng, H. J.; Zhang, Q. Porphyrin Organic Framework Hollow Spheres and Their Applications in Lithium–Sulfur Batteries. *Adv. Mater.* **2018**, *30* (23), 1–6. https://doi.org/10.1002/adma.201707483.

(98) Li, B.-Q.; Chen, X.-R.; Chen, X.; Zhao, C.-X.; Zhang, R.; Cheng, X.-B.; Zhang, Q. Favorable Lithium Nucleation on Lithiophilic Framework Porphyrin for Dendrite-Free Lithium Metal Anodes. *Research* **2019**, *2019*, 1–11. https://doi.org/10.34133/2019/4608940.

(99) Ghasemi, H.; Ni, G.; Marconnet, A. M.; Loomis, J.; Yerci, S.; Miljkovic, N.; Chen, G. Solar Steam Generation by Heat Localization. *Nat. Commun.* **2014**, *5*, 1–7. https://doi.org/10.1038/ncomms5449.

(100) Giannozzi, P.; Baroni, S.; Bonini, N.; Calandra, M.; Car, R.; Cavazzoni, C.; Ceresoli, D.; Chiarotti, G. L.; Cococcioni, M.; Dabo, I.; Dal Corso, A.; De Gironcoli, S.; Fabris, S.; Fratesi, G.; Gebauer, R.; Gerstmann, U.; Gougoussis, C.; Kokalj, A.; Lazzeri, M.; Martin-Samos, L.; Marzari, N.; Mauri, F.; Mazzarello, R.; Paolini, S.; Pasquarello, A.; Paulatto, L.; Sbraccia, C.; Scandolo, S.; Sclauzero, G.; Seitsonen, A. P.; Smogunov, A.; Umari, P.; Wentzcovitch, R. M. QUANTUM ESPRESSO: A Modular and Open-Source Software Project for Quantum Simulations of Materials. *J. Phys. Condens. Matter* **2009**, *21* (39). https://doi.org/10.1088/0953-8984/21/39/395502.

(101) Hamann, D. R. Erratum: Optimized Norm-Conserving Vanderbilt Pseudopotentials (Physical Review B (2013) 88 (085117) DOI: 10.1103/PhysRevB.88.085117). *Phys. Rev. B* **2017**, *95* (23), 239906. https://doi.org/10.1103/PhysRevB.95.239906.

(102) Blöchl, P. E. Projector Augmented-Wave Method. *Phys. Rev. B* **1994**, *50* (24), 17953–17979. https://doi.org/10.1103/PhysRevB.50.17953.

(103) Perdew, J. P.; Burke, K.; Ernzerhof, M. Generalized Gradient Approximation Made Simple. *Phys. Rev. Lett.* **1996**, *77* (18), 3865–3868. https://doi.org/10.1103/PhysRevLett.77.3865.

(104) Baker, R. W. *Membrane Technology and Applications*; John Wiley & Sons, Ltd: Chichester, UK, 2004. https://doi.org/10.1002/0470020393.

(105) Lalia, B. S.; Kochkodan, V.; Hashaikeh, R.; Hilal, N. A Review on Membrane Fabrication: Structure, Properties and Performance Relationship. *Desalination* **2013**, *326*, 77–95. https://doi.org/10.1016/j.desal.2013.06.016.

(106) Zhao, Y. H.; Qian, Y. L.; Zhu, B. K.; Xu, Y. Y. Modification of Porous Poly(Vinylidene Fluoride) Membrane Using Amphiphilic Polymers with Different Structures in Phase Inversion Process. *J. Memb. Sci.* **2008**, *310* (1–2), 567–576. https://doi.org/10.1016/j.memsci.2007.11.040.

(107) Arabi, S.; Pellegrin, M. L.; Aguinaldo, J.; Sadler, M. E.; McCandless, R.; Sadreddini, S.; Wong, J.; Burbano, M. S.; Koduri, S.; Abella, K.; Moskal, J.; Alimoradi, S.; Azimi, Y.; Dow, A.; Tootchi, L.; Kinser, K.; Kaushik, V.; Saldanha, V. *Membrane Processes*; 2020; Vol. 92. https://doi.org/10.1002/wer.1385.

(108) Park, H. B.; Kamcev, J.; Robeson, L. M.; Elimelech, M.; Freeman, B. D. Maximizing the Right Stuff: The Trade-off between Membrane Permeability and Selectivity. *Science (80-.).* **2017**, *356* (6343), 1138–1148. https://doi.org/10.1126/science.aab0530.

(109) Kandambeth, S.; Biswal, B. P.; Chaudhari, H. D.; Rout, K. C.; Kunjattu H., S.; Mitra, S.; Karak, S.; Das, A.; Mukherjee, R.; Kharul, U. K.; Banerjee, R. Selective Molecular Sieving in Self-Standing Porous Covalent-Organic-Framework Membranes. *Adv. Mater.* **2017**, *29* (2), 1603945. https://doi.org/10.1002/adma.201603945.

(110) Li, B.; Japip, S.; Chung, T. S. Molecularly Tunable Thin-Film Nanocomposite Membranes with Enhanced Molecular Sieving for Organic Solvent Forward Osmosis. *Nat. Commun.* **2020**, *11* (1), 1–10. https://doi.org/10.1038/s41467-020-15070-w.

(111) Gai, J. G.; Gong, X. L.; Wang, W. W.; Zhang, X.; Kang, W. L. An Ultrafast Water Transport Forward Osmosis Membrane: Porous Graphene. *J. Mater. Chem. A* **2014**, *2* (11), 4023–4028. https://doi.org/10.1039/c3ta14256f.

(112) Zhang, W. H.; Yin, M. J.; Zhao, Q.; Jin, C. G.; Wang, N.; Ji, S.; Ritt, C. L.; Elimelech, M.; An, Q. F. Graphene Oxide Membranes with Stable Porous Structure for Ultrafast Water Transport. *Nat. Nanotechnol.* **2021**, *16* (3), 337–343. https://doi.org/10.1038/s41565-020-00833-9.

(113) Kang, Y.; Xia, Y.; Wang, H.; Zhang, X. 2D Laminar Membranes for Selective Water and Ion Transport. *Advanced Functional Materials*. Wiley-VCH Verlag July 18, 2019. https://doi.org/10.1002/adfm.201902014.

(114) Andreeva, D. V.; Trushin, M.; Nikitina, A.; Costa, M. C. F.; Cherepanov, P. V.; Holwill, M.; Chen, S.; Yang, K.; Chee, S. W.; Mirsaidov, U.; Castro Neto, A. H.; Novoselov, K. S. Two-Dimensional Adaptive Membranes with Programmable Water and Ionic Channels. *Nat. Nanotechnol.* **2021**, *16* (2), 174–180. https://doi.org/10.1038/s41565-020-00795-y.

(115) Fathizadeh, M.; Xu, W. L.; Zhou, F.; Yoon, Y.; Yu, M. Graphene Oxide: A Novel 2-Dimensional Material in Membrane Separation for Water Purification. *Adv. Mater. Interfaces* **2017**, *4* (5). https://doi.org/10.1002/admi.201600918.

(116) Zhao, G.; Zhu, H. Cation–π Interactions in Graphene-Containing Systems for Water Treatment and Beyond. *Adv. Mater.* **2020**, *32* (22). https://doi.org/10.1002/adma.201905756.

(117) Chen, C.; Wang, J.; Liu, D.; Yang, C.; Liu, Y.; Ruoff, R. S.; Lei, W. Functionalized Boron Nitride Membranes with Ultrafast Solvent Transport Performance for Molecular Separation. *Nat. Commun.* **2018**, *9* (1). https://doi.org/10.1038/s41467-018-04294-6.

(118) Ding, L.; Wei, Y.; Wang, Y.; Chen, H.; Caro, J.; Wang, H. A Two-Dimensional Lamellar Membrane: MXene Nanosheet Stacks. *Angew. Chemie - Int. Ed.* **2017**, *56* (7), 1825–1829. https://doi.org/10.1002/anie.201609306.

(119) Hoenig, E.; Strong, S. E.; Wang, M.; Radhakrishnan, J. M.; Zaluzec, N. J.; Skinner, J. L.; Liu, C. Controlling the Structure of MoS2Membranes via Covalent Functionalization with

Molecular Spacers. *Nano Lett.* **2020**. https://doi.org/10.1021/acs.nanolett.0c02114.

(120) Cheng, P.; Chen, Y.; Gu, Y. H.; Yan, X.; Lang, W. Z. Hybrid 2D WS2/GO Nanofiltration Membranes for Finely Molecular Sieving. *J. Memb. Sci.* **2019**, *591* (May). https://doi.org/10.1016/j.memsci.2019.117308.

(121) Lu, P.; Wang, Y.; Wang, L.; Wei, Y.; Li, W.; Li, Y.; Tang, C. Y. Immobilization of Sulfonated Polysulfone via 2D LDH Nanosheets during Phase-Inversion: A Novel Strategy towards Greener Membrane Synthesis and Enhanced Desalination Performance. *J. Memb. Sci.* **2020**, *614* (July), 118508. https://doi.org/10.1016/j.memsci.2020.118508.

(122) Shao, J. J.; Raidongia, K.; Koltonow, A. R.; Huang, J. Self-Assembled Two-Dimensional Nanofluidic Proton Channels with High Thermal Stability. *Nat. Commun.* **2015**, *6*. https://doi.org/10.1038/ncomms8602.

(123) Momma, K.; Izumi, F. VESTA 3 for Three-Dimensional Visualization of Crystal, Volumetric and Morphology Data. *J. Appl. Crystallogr.* **2011**, *44* (6), 1272–1276. https://doi.org/10.1107/S0021889811038970.

(124) Survey, U. S. G. *Mineral Commodity Summaries 2020*; 2020.

(125) Huang, K.; Rowe, P.; Chi, C.; Sreepal, V.; Bohn, T.; Zhou, K. G.; Su, Y.; Prestat, E.; Pillai, P. B.; Cherian, C. T.; Michaelides, A.; Nair, R. R. Cation-Controlled Wetting Properties of Vermiculite Membranes and Its Promise for Fouling Resistant Oil–Water Separation. *Nat. Commun.* **2020**, *11* (1). https://doi.org/10.1038/s41467-020-14854-4.

(126) Walker, G. F.; Garrett, W. G. Chemical Exfoliation of Vermiculite and the Production of Colloidal Dispersions. *Science (80-.).* **1967**, *156* (3773), 385–387. https://doi.org/10.1126/science.156.3773.385.

(127) Tian, M.; Wang, L.; Wang, J.; Zheng, S.; Wang, F.; Shao, N.; Wang, L. A Two-Dimensional Lamellar Vermiculite Membrane for Precise Molecular Separation and Ion Sieving. *ACS Sustain. Chem. Eng.* **2022**, *10* (3), 1137–1148. https://doi.org/10.1021/acssuschemeng.1c05951.

(128) Xu, R.; Sun, Y.; Wang, Y.; Huang, J.; Zhang, Q. Two-Dimensional Vermiculite Separator for Lithium Sulfur Batteries. *Chinese Chem. Lett.* **2017**, *28* (12), 2235–2238. https://doi.org/10.1016/j.cclet.2017.09.065.

(129) Liu, T.; Zhang, C.; Yuan, J.; Zhen, Y.; Li, Y. Two-Dimensional Vermiculite Nanosheets-Modified Porous Membrane for Non-Aqueous Redox Flow Batteries. *J. Power Sources* **2021**, *500* (May), 229987. https://doi.org/10.1016/j.jpowsour.2021.229987.

(130) Razmjou, A.; Eshaghi, G.; Orooji, Y.; Hosseini, E.; Korayem, A. H.; Mohagheghian, F.; Boroumand, Y.; Noorbakhsh, A.; Asadnia, M.; Chen, V. Lithium Ion-Selective Membrane with 2D Subnanometer Channels. *Water Res.* **2019**, *159*, 313–323. https://doi.org/10.1016/j.watres.2019.05.018.

(131) Yu, B.; Wang, X.; Qian, X.; Xing, W.; Yang, H.; Ma, L.; Lin, Y.; Jiang, S.; Song, L.; Hu, Y.; Lo, S. Functionalized Graphene Oxide/Phosphoramide Oligomer Hybrids Flame

Retardant Prepared via in Situ Polymerization for Improving the Fire Safety of Polypropylene. *RSC Adv.* **2014**, *4* (60), 31782–31794. https://doi.org/10.1039/c3ra45945d.

(132) Zou, Y. C.; Mogg, L.; Clark, N.; Bacaksiz, C.; Milovanovic, S.; Sreepal, V.; Hao, G. P.; Wang, Y. C.; Hopkinson, D. G.; Gorbachev, R.; Shaw, S.; Novoselov, K. S.; Raveendran-Nair, R.; Peeters, F. M.; Lozada-Hidalgo, M.; Haigh, S. J. Ion Exchange in Atomically Thin Clays and Micas. *Nat. Mater.* **2021**, *20* (12), 1677–1682. https://doi.org/10.1038/s41563-021-01072-6.

(133) Zhang, H.; He, Q.; Luo, J.; Wan, Y.; Darling, S. B. Sharpening Nanofiltration: Strategies for Enhanced Membrane Selectivity. *ACS Appl. Mater. Interfaces* **2020**, *12* (36), 39948–39966. https://doi.org/10.1021/acsami.0c11136.

(134) Tran, T. T. Van; Kumar, S. R.; Lue, S. J. Separation Mechanisms of Binary Dye Mixtures Using a PVDF Ultrafiltration Membrane: Donnan Effect and Intermolecular Interaction. *J. Memb. Sci.* **2019**, *575* (June 2018), 38–49. https://doi.org/10.1016/j.memsci.2018.12.070.

(135) Bason, S.; Freger, V. Phenomenological Analysis of Transport of Mono- and Divalent Ions in Nanofiltration. *J. Memb. Sci.* **2010**, *360* (1–2), 389–396. https://doi.org/10.1016/j.memsci.2010.05.037.

(136) Kaganovich, M.; Zhang, W.; Freger, V.; Bernstein, R. Effect of the Membrane Exclusion Mechanism on Phosphate Scaling during Synthetic Effluent Desalination. *Water Res.* **2019**, *161*, 381–391. https://doi.org/10.1016/j.watres.2019.06.013.

(137) Vold, M. J. Zeta Potential in Colloid Science. Principles and Applications. *J. Colloid Interface Sci.* **1982**, *88* (2), 608. https://doi.org/10.1016/0021-9797(82)90296-X.

(138) Xie, H.; Saito, T.; Hickner, M. A. Zeta Potential of Ion-Conductive Membranes by Streaming Current Measurements. *Langmuir* **2011**, *27* (8), 4721–4727. https://doi.org/10.1021/la105120f.

(139) Tan, R.; Wang, A.; Malpass-Evans, R.; Williams, R.; Zhao, E. W.; Liu, T.; Ye, C.; Zhou, X.; Darwich, B. P.; Fan, Z.; Turcani, L.; Jackson, E.; Chen, L.; Chong, S. Y.; Li, T.; Jelfs, K. E.; Cooper, A. I.; Brandon, N. P.; Grey, C. P.; McKeown, N. B.; Song, Q. Hydrophilic Microporous Membranes for Selective Ion Separation and Flow-Battery Energy Storage. *Nat. Mater.* **2020**, *19* (2), 195–202. https://doi.org/10.1038/s41563-019-0536-8.

(140) Kummu, M.; Guillaume, J. H. A.; De Moel, H.; Eisner, S.; Flörke, M.; Porkka, M.; Siebert, S.; Veldkamp, T. I. E.; Ward, P. J. The World's Road to Water Scarcity: Shortage and Stress in the 20th Century and Pathways towards Sustainability. *Sci. Rep.* **2016**, *6* (December), 1–16. https://doi.org/10.1038/srep38495.

(141) Gehrke, I.; Geiser, A.; Somborn-Schulz, A. Innovations in Nanotechnology for Water Treatment. *Nanotechnol. Sci. Appl.* **2015**, *8*, 1–17. https://doi.org/10.2147/NSA.S43773.

(142) Ahmed, M. J. K.; Ahmaruzzaman, M. A Review on Potential Usage of Industrial Waste Materials for Binding Heavy Metal Ions from Aqueous Solutions. *J. Water Process Eng.* **2016**, *10*, 39–47. https://doi.org/10.1016/j.jwpe.2016.01.014.

(143) Yang, M.; Hadi, P.; Yin, X.; Yu, J.; Huang, X.; Ma, H.; Walker, H.; Hsiao, B. S. Antifouling Nanocellulose Membranes: How Subtle Adjustment of Surface Charge Lead to Self-Cleaning Property. *J. Memb. Sci.* **2021**, *618* (September 2020), 118739. https://doi.org/10.1016/j.memsci.2020.118739.

(144) Zhang, M.; Guan, K.; Ji, Y.; Liu, G.; Jin, W.; Xu, N. Controllable Ion Transport by Surface-Charged Graphene Oxide Membrane. *Nat. Commun.* **2019**, *10* (1), 1–8. https://doi.org/10.1038/s41467-019-09286-8.

(145) Gao, J.; Guo, W.; Feng, D.; Wang, H.; Zhao, D.; Jiang, L. High-Performance Ionic Diode Membrane for Salinity Gradient Power Generation. *J. Am. Chem. Soc.* **2014**, *136* (35), 12265–12272. https://doi.org/10.1021/ja503692z.

(146) Efome, J. E.; Rana, D.; Matsuura, T.; Lan, C. Q. Insight Studies on Metal-Organic Framework Nanofibrous Membrane Adsorption and Activation for Heavy Metal Ions Removal from Aqueous Solution. *ACS Appl. Mater. Interfaces* **2018**, *10* (22), 18619–18629. https://doi.org/10.1021/acsami.8b01454.

(147) Ernst, M.; Bismarck, A.; Springer, J.; Jekel, M. Zeta-Potential and Rejection Rates of a Polyethersulfone Nanofiltration Membrane in Single Salt Solutions. *J. Memb. Sci.* **2000**, *165* (2), 251–259. https://doi.org/10.1016/S0376-7388(99)00238-0.

(148) McNeil, S. E. *Challenges for Nanoparticle Characterization.*; 2011; Vol. 697. https://doi.org/10.1007/978-1-60327-198-1_2.

(149) Mavukkandy, M. O.; McBride, S. A.; Warsinger, D. M.; Dizge, N.; Hasan, S. W.; Arafat, H. A. Thin Film Deposition Techniques for Polymeric Membranes– A Review. *J. Memb. Sci.* **2020**, *610* (May), 118258. https://doi.org/10.1016/j.memsci.2020.118258.

(150) Dendooven, J.; Devloo-Casier, K.; Levrau, E.; Van Hove, R.; Pulinthanathu Sree, S.; Baklanov, M. R.; Martens, J. A.; Detavernier, C. In Situ Monitoring of Atomic Layer Deposition in Nanoporous Thin Films Using Ellipsometric Porosimetry. *Langmuir* **2012**, *28* (8), 3852–3859. https://doi.org/10.1021/la300045z.

(151) Cameron, M. A.; Gartland, I. P.; Smith, J. A.; Diaz, S. F.; George, S. M. Atomic Layer Deposition of SiO2 and TiO2 in Alumina Tubular Membranes: Pore Reduction and Effect of Surface Species on Gas Transport. *Langmuir* **2000**, *16* (19), 7435–7444. https://doi.org/10.1021/la9916981.

(152) Knez, M.; Nielsch, K.; Niinistö, L. Synthesis and Surface Engineering of Complex Nanostructures by Atomic Layer Deposition. *Adv. Mater.* **2007**, *19* (21), 3425–3438. https://doi.org/10.1002/adma.200700079.

(153) Weber, M.; Julbe, A.; Kim, S. S.; Bechelany, M. Atomic Layer Deposition (ALD) on Inorganic or Polymeric Membranes. *J. Appl. Phys.* **2019**, *126* (4), 1–11. https://doi.org/10.1063/1.5103212.

(154) Yang, X.; Sun, P.; Zhang, H.; Xia, Z.; Waldman, R. Z.; Mane, A. U.; Elam, J. W.; Shao, L.; Darling, S. B. Polyphenol-Sensitized Atomic Layer Deposition for Membrane

Interface Hydrophilization. *Adv. Funct. Mater.* **2020**. https://doi.org/10.1002/adfm.201910062.

(155) Marsalek, R. Particle Size and Zeta Potential of ZnO. *APCBEE Procedia* **2014**, *9*, 13–17. https://doi.org/10.1016/j.apcbee.2014.01.003.

(156) Siti, S. A.; Amirnordin, S. H.; Rahman, H. A.; Abdullah, H. Z.; Taib, H. Effect of Zeta Potential of Stanum Oxide (SnO2) on Electrophoretic Deposition (EPD) on Porous Alumina. *Adv. Mater. Res.* **2013**, *795*, 334–337. https://doi.org/10.4028/www.scientific.net/AMR.795.334.

(157) Liao, D. L.; Wu, G. S.; Liao, B. Q. Zeta Potential of Shape-Controlled TiO2 Nanoparticles with Surfactants. *Colloids Surfaces A Physicochem. Eng. Asp.* **2009**, *348* (1–3), 270–275. https://doi.org/10.1016/j.colsurfa.2009.07.036.

(158) Shao, Y.; Ren, B.; Jiang, H.; Zhou, B.; LV, L.; Ren, J.; Dong, L.; Li, J.; Liu, Z. Dual-Porosity Mn2O3 Cubes for Highly Efficient Dye Adsorption. *J. Hazard. Mater.* **2017**, *333*, 222–231. https://doi.org/10.1016/j.jhazmat.2017.03.014.

(159) Gu, D.; Yalcin, S.; Baumgart, H.; Qian, S.; Baysal, O.; Beskok, A. Electrophoretic Light Scattering for Surface Zeta Potential Measurement of ALD Metal Oxide Films. *ECS Trans.* **2019**, *33* (2), 37–41. https://doi.org/10.1149/1.3485239.

(160) Linn, J. H.; Swartz, W. E. An XPS Study of the Water Adsorption/Desorption Characteristics of Transition Metal Oxide Surfaces: Microelectronic Implications. *Appl. Surf. Sci.* **1984**, *20* (1), 154–166. https://doi.org/https://doi.org/10.1016/0378-5963(84)90335-0.

(161) Rana, D.; Matsuura, T. Surface Modifications for Antifouling Membranes. *Chem. Rev.* **2010**, *110* (4), 2448–2471. https://doi.org/10.1021/cr800208y.

(162) Oh, I.-K.; Zeng, L.; Kim, J.-E.; Park, J.-S.; Kim, K.; Lee, H.; Seo, S.; Khan, M. R.; Kim, S.; Park, C. W.; Lee, J.; Shong, B.; Lee, Z.; Bent, S. F.; Kim, H.; Park, J. Y.; Lee, H.-B.-R. Surface Energy Change of Atomic-Scale Metal Oxide Thin Films by Phase Transformation. *ACS Nano* **2020**, *14* (1), 676–687. https://doi.org/10.1021/acsnano.9b07430.

(163) Kosmulski, M. Isoelectric Points and Points of Zero Charge of Metal (Hydr) Oxides : 50 Years after Parks ' Review. *Adv. Colloid Interface Sci.* **2016**, *238*, 1–61. https://doi.org/10.1016/j.cis.2016.10.005.

(164) Zhang, Q.; Jing, W.; Fan, Y.; Xu, N. An Improved Parks Equation for Prediction of Surface Charge Properties of Composite Ceramic Membranes. *J. Memb. Sci.* **2008**, *318* (1–2), 100–106. https://doi.org/10.1016/j.memsci.2008.02.004.

(165) Cornell, R. .; Posner, A. .; Quirk, J. . A Titrimetric and Electrophoretic Investigation of the Pzc and the Iep of Pigment Rutile. *J. Colloid Interface Sci.* **1975**, *53* (1), 6–13. https://doi.org/10.1016/0021-9797(75)90028-4.

(166) Kosmulski, M. The PH Dependent Surface Charging and Points of Zero Charge. VIII.

Update. *Adv. Colloid Interface Sci.* **2020**, *275*, 102064. https://doi.org/10.1016/j.cis.2019.102064.

(167) Putman, B.; Van der Meeren, P.; Thierens, D. Reduced Bovine Serum Albumin Adsorption by Prephosphatation of Powdered Zirconium Oxide. *Colloids Surfaces A Physicochem. Eng. Asp.* **1997**, *121* (1), 81–88. https://doi.org/10.1016/S0927-7757(96)03978-7.

(168) Morimoto, T.; Kittaka, S. Isoelectric Point of Manganese Oxide. *Bull. Chem. Soc. Jpn.* **1974**, *47* (7), 1586–1588. https://doi.org/10.1246/bcsj.47.1586.

(169) Ardizzone, S.; Spinolo, G.; Trasatti, S. The Point of Zero Charge of Co3O4 Prepared by Thermal Decomposition of Basic Cobalt Carbonate. *Electrochim. Acta* **1995**, *40* (16), 2683–2686. https://doi.org/10.1016/0013-4686(95)00238-A.

(170) Bogdanova, N. F.; Klebanov, A. V.; Ermakova, L. E.; Sidorova, M. P.; Aleksandrov, D. A. Adsorption of Ions on the Surface of Tin Dioxide and Its Electrokinetic Characteristics in 1 : 1 Electrolyte Solutions. *Colloid J.* **2004**, *66* (4), 409–417. https://doi.org/10.1023/B:COLL.0000037445.08721.85.

(171) Díaz de León, J. N. Binary γ-Al2O3–α-Ga2O3 as Supports of NiW Catalysts for Hydrocarbon Sulfur Removal. *Appl. Catal. B Environ.* **2016**, *181*, 524–533. https://doi.org/10.1016/j.apcatb.2015.08.028.

(172) Szekeres, M.; Dékány, I.; de Keizer, A. Adsorption of Dodecyl Pyridinium Chloride on Monodisperse Porous Silica. *Colloids Surfaces A Physicochem. Eng. Asp.* **1998**, *141* (3), 327–336. https://doi.org/10.1016/S0927-7757(97)00116-7.

(173) Deliormanlı, A. M.; Çelik, E.; Polat, M. The Isoelectric Point of Lead Magnesium Niobate. *J. Am. Ceram. Soc.* **2007**, *90* (10), 3314–3317. https://doi.org/10.1111/j.1551-2916.2007.01871.x.

(174) Kosmulski, M. Pristine Points of Zero Charge of Gallium and Indium Oxides. *J. Colloid Interface Sci.* **2001**, *238* (1), 225–227. https://doi.org/10.1006/jcis.2001.7484.

(175) Gonza, F. Electrical Surface Charge and Potential of Hematite / Yttrium Oxide Core ± Shell Colloidal Particles. *Colloid Polym. Sci.* **2001**, *1211*, 1206–1211.

(176) Naklicki, M. L.; Rao, S. R.; Gomez, M.; Finch, J. A. Flotation and Surface Analysis of the Nickel (II) Oxide / Amyl Xanthate System. *Int. J. Miner. Process.* **2002**, *65*, 73–82.

(177) Zhang, Y.; Chen, Y.; Westerhoff, P.; Hristovski, K.; Ã, J. C. C. Stability of Commercial Metal Oxide Nanoparticles in Water. *Water Res.* **2008**, *42*, 2204–2212. https://doi.org/10.1016/j.watres.2007.11.036.

(178) Subramaniam, K.; Yiacoumi, S.; Tsouris, C. Copper Uptake by Inorganic Particles — Equilibrium , Kinetics , and Particle Interactions : Experimental. *Colloids Surfaces A Physicochem. Eng. Asp.* **2001**, *177*, 133–146.

(179) Kosmulski, M.; Maczka, E. Synthesis and Characterization of Goethite and Goethite –

Hematite Composite : Experimental Study and Literature Survey. *Adv. Colloid Interface Sci.* **2003**, *103* (02), 57–76. https://doi.org/10.1016/S0001-8686(02)00083-0.

(180) Elam, J. W.; Groner, M. D.; George, S. M. Viscous Flow Reactor with Quartz Crystal Microbalance for Thin Film Growth by Atomic Layer Deposition. *Rev. Sci. Instrum.* **2002**, *73* (8), 2981. https://doi.org/10.1063/1.1490410.

(181) Rozyyev, V.; Murphy, J. G.; Barry, E.; Mane, A. U.; Sibener, S. J.; Elam, J. W. Vapor-Phase Grafting of a Model Aminosilane Compound to Al2O3, ZnO, and TiO2 Surfaces Prepared by Atomic Layer Deposition. *Appl. Surf. Sci.* **2021**, *562*, 149996. https://doi.org/https://doi.org/10.1016/j.apsusc.2021.149996.

(182) Prodanovic´, V.; Chan, H. W.; Mane, A. U.; Elam, J. W.; Minjauw, M. M.; Detavernier, C.; van der Graaf, H.; Sarro, P. M. Effect of Thermal Annealing and Chemical Treatments on Secondary Electron Emission Properties of Atomic Layer Deposited MgO. *J. Vac. Sci. Technol. A* **2018**, *36* (6), 06A102. https://doi.org/10.1116/1.5040813.

(183) Hausmann, D. M.; Kim, E.; Becker, J.; Gordon, R. G. Atomic Layer Deposition of Hafnium and Zirconium Oxides Using Metal Amide Precursors. *Chem. Mater.* **2002**, *14* (10), 4350–4358. https://doi.org/10.1021/cm020357x.

(184) Burton, B. B.; Fabreguette, F. H.; George, S. M. Atomic Layer Deposition of MnO Using Bis(Ethylcyclopentadienyl)Manganese and H2O. *Thin Solid Films* **2009**, *517* (19), 5658–5665. https://doi.org/https://doi.org/10.1016/j.tsf.2009.02.050.

(185) Zhang, Z.; Nallan, H. C.; Coffey, B. M.; Ngo, T. Q.; Pramanik, T.; Banerjee, S. K.; Ekerdt, J. G. Atomic Layer Deposition of Cobalt Oxide on Oxide Substrates and Low Temperature Reduction to Form Ultrathin Cobalt Metal Films. *J. Vac. Sci. Technol. A* **2018**, *37* (1), 10903. https://doi.org/10.1116/1.5063669.

(186) Elam, J. W.; Baker, D. A.; Hryn, A. J.; Martinson, A. B. F.; Pellin, M. J.; Hupp, J. T. Atomic Layer Deposition of Tin Oxide Films Using Tetrakis(Dimethylamino) Tin. *J. Vac. Sci. Technol. A* **2008**, *26* (2), 244–252. https://doi.org/10.1116/1.2835087.

(187) Yang, R. Bin; Bachmann, J.; Reiche, M.; Gerlach, J. W.; Gösele, U.; Nielsch, K. Atomic Layer Deposition of Antimony Oxide and Antimony Sulfide. *Chem. Mater.* **2009**, *21* (13), 2586–2588. https://doi.org/10.1021/cm900623v.

(188) Dezelah; Niinistö, J.; Arstila, K.; Niinistö, L.; Winter, C. H. Atomic Layer Deposition of Ga2O3 Films from a Dialkylamido-Based Precursor. *Chem. Mater.* **2006**, *18* (2), 471–475. https://doi.org/10.1021/cm0521424.

(189) Badot, J. C.; Mantoux, A.; Baffier, N.; Dubrunfaut, O.; Lincot, D. Electrical Properties of V2O5 Thin Films Obtained by Atomic Layer Deposition (ALD). *J. Mater. Chem.* **2004**, *14* (23), 3411–3415. https://doi.org/10.1039/B410324F.

(190) Bachmann, J.; Zierold, R.; Chong, Y. T.; Hauert, R.; Sturm, C.; Schmidt-Grund, R.; Rheinländer, B.; Grundmann, M.; Gösele, U.; Nielsch, K. A Practical, Self-Catalytic, Atomic Layer Deposition of Silicon Dioxide. *Angew. Chemie Int. Ed.* **2008**, *47* (33),

6177–6179. https://doi.org/https://doi.org/10.1002/anie.200800245.

(191) Knapas, K.; Rahtu, A.; Ritala, M. Reaction Mechanism Studies on Atomic Layer Deposition of Nb2O5 from Nb(OEt)5 and Water. *Langmuir* **2010**, *26* (2), 848–853. https://doi.org/10.1021/la902289h.

(192) Libera, J. A.; Hryn, J. N.; Elam, J. W. Indium Oxide Atomic Layer Deposition Facilitated by the Synergy between Oxygen and Water. *Chem. Mater.* **2011**, *23* (8), 2150–2158. https://doi.org/10.1021/cm103637t.

(193) Niinistö, J.; Putkonen, M.; Niinistö, L. Processing of Y2O3 Thin Films by Atomic Layer Deposition from Cyclopentadienyl-Type Compounds and Water as Precursors. *Chem. Mater.* **2004**, *16* (15), 2953–2958. https://doi.org/10.1021/cm040145v.

(194) Nardi, K. L.; Yang, N.; Dickens, C. F.; Strickler, A. L.; Bent, S. F. Creating Highly Active Atomic Layer Deposited NiO Electrocatalysts for the Oxygen Evolution Reaction. *Adv. Energy Mater.* **2015**, *5* (17), 1500412. https://doi.org/https://doi.org/10.1002/aenm.201500412.

(195) Martinson, A. B. F.; DeVries, M. J.; Libera, J. A.; Christensen, S. T.; Hupp, J. T.; Pellin, M. J.; Elam, J. W. Atomic Layer Deposition of Fe2O3 Using Ferrocene and Ozone. *J. Phys. Chem. C* **2011**, *115* (10), 4333–4339. https://doi.org/10.1021/jp110203x.

(196) Martín, A.; Martínez, F.; Malfeito, J.; Palacio, L.; Prádanos, P.; Hernández, A. Zeta Potential of Membranes as a Function of PH: Optimization of Isoelectric Point Evaluation. *J. Memb. Sci.* **2003**, *213* (1–2), 225–230. https://doi.org/10.1016/S0376-7388(02)00530-6.

(197) Martínez, F.; Martín, A.; Malfeito, J.; Palacio, L.; Prádanos, P.; Tejerina, F.; Hernández, A. Streaming Potential through and on Ultrafiltration Membranes. *J. Memb. Sci.* **2002**, *206* (1–2), 431–441. https://doi.org/10.1016/s0376-7388(01)00788-8.

(198) Cheng, L. J.; Guo, L. J. Nanofluidic Diodes. *Chem. Soc. Rev.* **2010**, *39* (3), 923–938. https://doi.org/10.1039/b822554k.

(199) Strathmann, H.; Krol, J. J.; Rapp, H. J.; Eigenberger, G. Limiting Current Density and Water Dissociation in Bipolar Membranes. *J. Memb. Sci.* **1997**, *125* (1), 123–142. https://doi.org/10.1016/S0376-7388(96)00185-8.

(200) Zhang, Z.; Kong, X.-Y.; Xiao, K.; Liu, Q.; Xie, G.; Li, P.; Ma, J.; Tian, Y.; Wen, L.; Jiang, L. Engineered Asymmetric Heterogeneous Membrane: A Concentration-Gradient-Driven Energy Harvesting Device. *J. Am. Chem. Soc.* **2015**, *137* (46), 14765–14772. https://doi.org/10.1021/jacs.5b09918.

(201) Zhang, Z.; Li, P.; Kong, X. Y.; Xie, G.; Qian, Y.; Wang, Z.; Tian, Y.; Wen, L.; Jiang, L. Bioinspired Heterogeneous Ion Pump Membranes: Unidirectional Selective Pumping and Controllable Gating Properties Stemming from Asymmetric Ionic Group Distribution. *J. Am. Chem. Soc.* **2018**. https://doi.org/10.1021/jacs.7b11472.

(202) Li, C.; Zhao, Y.; He, L.; Mo, R.; Gao, H.; Zhou, C.; Hong, P.; Sun, S.; Zhang, G. Mussel-Inspired Fabrication of Porous Anodic Alumina Nanochannels and a Graphene Oxide

Interfacial Ionic Rectification Device. *Chem. Commun.* **2018**. https://doi.org/10.1039/c8cc00209f.

(203) Yeung, T.; Gilbert, G. E.; Shi, J.; Silvius, J.; Kapus, A.; Grinstein, S. Membrane Phosphatidylserine Regulates Surface Charge and Protein Localization. *Science (80-.).* **2008**, *319* (5860), 210–213. https://doi.org/10.1126/science.1152066.

(204) Huang, X.; Kong, X. Y.; Wen, L.; Jiang, L. Bioinspired Ionic Diodes: From Unipolar to Bipolar. *Advanced Functional Materials*. 2018. https://doi.org/10.1002/adfm.201801079.

(205) Zhang, Q.; Liu, Q.; Kang, J.; Huang, Q.; Liu, Z.; Diao, X.; Zhai, J. Robust Sandwich-Structured Nanofluidic Diodes Modulating Ionic Transport for an Enhanced Electrochromic Performance. *Adv. Sci.* **2018**, *5* (9). https://doi.org/10.1002/advs.201800163.

(206) Feng, Y.; Zhu, W.; Guo, W.; Jiang, L. Bioinspired Energy Conversion in Nanofluidics: A Paradigm of Material Evolution. *Adv. Mater.* **2017**. https://doi.org/10.1002/adma.201702773.

(207) Cao, L.; Wen, Q.; Feng, Y.; Ji, D.; Li, H.; Li, N.; Jiang, L.; Guo, W. On the Origin of Ion Selectivity in Ultrathin Nanopores: Insights for Membrane-Scale Osmotic Energy Conversion. *Adv. Funct. Mater.* **2018**. https://doi.org/10.1002/adfm.201804189.

(208) Zhu, X.; Zhou, Y.; Hao, J.; Bao, B.; Bian, X.; Jiang, X.; Pang, J.; Zhang, H.; Jiang, Z.; Jiang, L. A Charge-Density-Tunable Three/Two-Dimensional Polymer/Graphene Oxide Heterogeneous Nanoporous Membrane for Ion Transport. *ACS Nano* **2017**. https://doi.org/10.1021/acsnano.7b03576.

(209) Pérez-Mitta, G.; Tuninetti, J. S.; Knoll, W.; Trautmann, C.; Toimil-Molares, M. E.; Azzaroni, O. Polydopamine Meets Solid-State Nanopores: A Bioinspired Integrative Surface Chemistry Approach to Tailor the Functional Properties of Nanofluidic Diodes. *J. Am. Chem. Soc.* **2015**. https://doi.org/10.1021/jacs.5b01638.

(210) Zhang, Z.; Kong, X. Y.; Xiao, K.; Liu, Q.; Xie, G.; Li, P.; Ma, J.; Tian, Y.; Wen, L.; Jiang, L. Engineered Asymmetric Heterogeneous Membrane: A Concentration-Gradient-Driven Energy Harvesting Device. *J. Am. Chem. Soc.* **2015**, *137* (46), 14765–14772. https://doi.org/10.1021/jacs.5b09918.

(211) Bazinet, L.; Lamarche, F.; Ippersiel, D. Bipolar-Membrane Electrodialysis: Applications of Electrodialysis in the Food Industry. *Trends Food Sci. Technol.* **1998**, *9* (3), 107–113. https://doi.org/10.1016/S0924-2244(98)00026-0.

(212) Bao, B.; Hao, J.; Bian, X.; Zhu, X.; Xiao, K.; Liao, J.; Zhou, J.; Zhou, Y.; Jiang, L. 3D Porous Hydrogel/Conducting Polymer Heterogeneous Membranes with Electro-/PH-Modulated Ionic Rectification. *Adv. Mater.* **2017**, *29* (44), 1–7. https://doi.org/10.1002/adma.201702926.

(213) White, H. S.; Bund, A. Ion Current Rectification at Nanopores in Glass Membranes. *Langmuir* **2008**, *24* (5), 2212–2218. https://doi.org/10.1021/la702955k.

(214) Zhang, Z.; Xie, G.; Xiao, K.; Kong, X. Y.; Li, P.; Tian, Y.; Wen, L.; Jiang, L. Asymmetric Multifunctional Heterogeneous Membranes for PH- and Temperature-Cooperative Smart Ion Transport Modulation. *Adv. Mater.* **2016**. https://doi.org/10.1002/adma.201602758.

(215) Yan, R.; Liang, W.; Fan, R.; Yang, P. Nanofluidic Diodes Based on Nanotube Heterojunctions. *Nano Lett.* **2009**. https://doi.org/10.1021/nl9020123.